Monitoring bioinspired fibrillar grippers by contact observation and machine learning

Dissertation

zur Erlangung des Grades
des Doktors der Ingenieurwissenschaften
der Naturwissenschaftlich-Technischen Fakultät
der Universität des Saarlandes

von

Manar Samri

Saarbrücken 2022

Tag des Kolloquiums:	07 July 2023
Berichterstatter:	Prof. Dr. Eduard Arzt
	Prof. Dr. Stefan Seelecke
	Prof. Dr. Herbert Shea
Vorsitz:	Prof. Dr. Tobias Kraus
Akad. Mitarbeiter:	Dr.-Ing. Frank Aubertin

Abstract

The remarkable properties of bio-inspired microstructures make them extensively accessible for various applications, including industrial, medical, and space applications. However, their implementation especially as grippers for pick-and-place robotics can be compromised by multiple factors. The most common ones are alignment imperfections with the target object, unbalanced stress distribution, contamination, defects, and roughness at the gripping interface.

In the present work, three different approaches to assess the contact phenomena between patterned structures and the target object are presented. First, *in-situ* observation and machine learning are combined to realize accurate real-time predictions of adhesion performance. The trained supervised learning models successfully predict the adhesion performance from the contact signature. Second, two newly developed optical systems are compared to observe the correct grasping of various target objects (rough or transparent) by looking through the microstructures. And last, model experiments are provided for a direct comparison with simulation efforts aiming at a prediction of the contact signature and an analysis of the rate and preload-dependency of the adhesion strength of a soft polymer film in contact with roughness-like surface topography. The results of this thesis open new perspectives for improving the reliability of handling systems using bioinspired microstructures.

Kurzzusammenfasung

Durch die besonderen Eigenschaften bioinspirierter Mikrostrukturen können diese für verschiedene Anwendungen genutzt werden, einschließlich industrieller, medizinischer und Weltraumanwendungen. Ihre Implementierung, insbesondere als Greifer für Pick-and-Place-Robotiker, kann jedoch durch mehrere Faktoren beeinträchtigt werden. Am häufigsten sind Ausrichtungsmängel an das Zielobjekt, unausgeglichene Spannungsverteilungen, Defekte und Rauheit an der Greifschnittstelle.

Die vorliegende Arbeit zeigt drei verschiedene Ansätze, um den Kontakt zwischen strukturierten Adhäsiven und Zielobjekten zu untersuchen. Zunächst werden *in-situ* Beobachtungen und maschinelles Lernen kombiniert, um Echtzeitvorhersagen der Adhäsionsleistung zu ermöglichen. Die trainierten Modelle werden verwendet, um die Haftungsleistung anhand der Kontaktsignatur des Pads erfolgreich zu prognostizieren. Anschließend werden zwei neu entwickelte, optische Systeme verglichen, mit denen das korrekte „Greifen“ von verschiedenen Objekten (mit rauen oder undurchsichtigen Oberflächen) durch die Mikrostrukturen live verfolgt werden kann. Zuletzt werden Modellexperimente durchgeführt, die mit Simulationen der Signatur des Kontakts einer weichen Polymerschicht mit einer idealisierten rauen Gegenfläche direkt verglichen werden können. Die Ergebnisse dieser Arbeit eröffnen neue Perspektiven zur zuverlässigeren Verwendung von Handhabungssystemen mit bioinspirierten Mikrostrukturen.

‘And say, my Lord increase me in knowledge’
The Quran 20:114

Acknowledgements

The research for this thesis was conducted at the INM - Leibniz Institute for New Materials in the Functional Microstructures Group between 2019 and 2022 under the scientific guidance of Prof. Eduard Arzt.

Six months into my Ph.D. project the world was faced with a global pandemic. A highly challenging, life-threatening, and heart-breaking situation. By the end of my Ph.D. journey, life is going back to normal, and for that I am grateful. Grateful for science and scientists, who worked hard and fought this pandemic as fast as possible, grateful to all the hard-working people who stood in the front line throughout the pandemic, and grateful for all the lessons I have learned. Lessons that will stay with me for the rest of my life. In the face of the pandemic, I have learned new ways of working, new ways of living, and new ways of taking appreciation. I have learned patience, and I have learned how adversity can forge us and make us stronger. But most importantly, I have learned that success only comes from the support, guidance, and love of the people in our life. Therefore, I would like to take this opportunity to thank everyone who contributed directly or indirectly to the accomplishment of this important step of my life:

Foremost, my sincere gratitude goes to Prof. Dr. Eduard Arzt for giving me the opportunity to pursue my Ph.D. within his research group. Thank you for the constructive discussions and for your guidance through the different challenges. Thank you for your trust and for the freedom you have given me to do my research and find my own way. I am honored to be your student.

I cordially thank Prof. Stefan Seelecke for accepting to be my academic supervisor. For the motivating discussion and for his helpful observations.

I would like to thank Dr. René Hensel for being my supervisor and mentor since my first day at INM. Thank you for the invaluable support, advices, and useful suggestions in the different projects we have worked on together. In each step of my journey, you have always been generous with your time and patiently guided me.

Next, I would like to express my gratitude to Dr. Peter Rogin for his valuable

contribution to the development of the new optical devices, and to Fabian Faller for the development of the second optical device and for his technical support.

Likewise, I would like to thank Christian Müller, and Prof. Martin Müser, for the fruitful collaboration on the "combined numerical and experimental study of adhesion to rough surfaces" which materialized as a joint manuscript in preparation.

Additionally, I would like to acknowledge Dr. Tim Dahmena and Dr. Taoufik En-nejjari for the insightful discussions and guidance on the machine learning project.

Special thanks to Jonathan Thiemke and Eva Prinz for their support and help in carrying out different experiments and collecting data.

Thank you to all INM colleagues who have been helpful and supportive, fostering a pleasant and productive environment, particularly, the current and former members of the Functional Microstructures group: Dr. Xuan Zahng, Dr.Yue Wang, Lisa sold, Joachim Blau, Dr. Haocheng Quan, Dr. Katharina Sorg, Gabriela Moreira Lana, Angela Rutz, Andreas Weyand, Dr. Gisela Heppe, Pamela Kalmes, Dr. Lena Barnefske and Susanne Selzer. Furthermore, I would like to thank the team of the Mechanical Workshop of our institute, especially Martin Schmidt, for his technical support whenever I needed it.

My sincere gratitude goes to my parents whose love and guidance are with me in whatever I pursue; my siblings Samir, Samar, Anas, and my cousin Siham for being my role models since I was a kid; my husband Murad Abu-aisheh for his love and patient throughout the last three years. Thank you all for always being there for me, for the encouraging words, and for the continued motivation.

Last but not the least, I would like to thank all the friends I have made during this journey, I am so glad I had the chance to meet such wonderful people. A special thanks to Loubna and Dilawar for making the last stressful days of my Ph.D. also filled with fun and laughter, and to Viktor for never missing our flammkuchen meeting and for the wonderful conversations we had.

Abbreviations and symbols

Abbreviations and symbols used in the chapters similarly:

Materials and material properties:

E Elastic modulus

u Elongation

k Stiffness

ν Poisson's ratio

PDMS Polydimethylsiloxane

Methods

SEM Scanning Electron Microscopy

JKR Johnson-Kendall-Roberts

GFMD Greens Function Molecular Dynamics

FEM Finite-Element Method

AFM Atomic force microscopy

FTIR Frustrated Total Internal Reflection

IRM Interference Reflection Microscop

ANOVA Analysis of variance

SSIM Structural similarity index measure

Adhesion parameters:

E_{keesom} Keesom energy

E_{Debye} Debye energy

E_{London} London energy

σ Pull-off stress

F_p Pull-off force

F Preload Force

f_{max} Pull-off force of an individual fibril

G_c Energy release rate

A Real contact area

A_a Apparent contact area

N_a Number of attached fibrils

N_d Number of detached fibrils

Abbreviations and symbols used in the chapters differently:

Machine learning:

ML Machine Learning

AI Artificial Intelligence

PCA Principal Component Analysis

LnR Linear Regression

LR Logistic Regression

SVM Support Vector Machine

SVR Support Vector Regression

BT Boosted Tree

KNN K-Nearest Neighbor

AUC-ROC Area under the receiver operating characteristic curve

D Training data

G Information gain

Tp True Positive

Tn True Negative

Fp False Positive

Fn False Negative

P Precision

R Recall

F_1 Score

R^2 R Square

$RMSE$ Root Mean Square Error

MAE Mean Absolute Error

y_i The value of the i-th observation in the validation data

$\hat{y}_i$ The predicted value

$\bar{y}_i$ the mean of the observed data

n the number of observations

N_m Number of samples

H The chosen split criteria function

Q The data at node

m the nod

$\theta = (x_m, t_m)$ The feature and threshold being evaluated

Fibrillar structure parameters:

N Total number of fibrils

h Fibril length

W Half the width of the array

a Mushroom tip radius

r Stalk radius

d Distance between adjacent fibrils

Weibull statistical parameters:

m Weibull modulus

u_0 Reference elongation at detachment

f_0 Reference force

Chapter 2:

C Contact compliance

d Contact diameter

Chapter 3:

θ Misalignment angle

M Peeling moment

$\vec{v}$ Misalignment vector

$W - |\vec{v}|$ Length of the misalignment vector

A' Normalized real contact area

N'_a Normalized number of attached fibrils

$(W - |\vec{v}|)'$ Normalized length of the misalignment vector

Chapter 4:

α Robot misalignment angle (rotation around x axe)

β Robot misalignment angle (rotation around y axe)

w Off-center object displacement

C Center of mass

$|\vec{v}|$ Misalignment vector magnitude

θ Misalignment vector angle with respect to the x axis

Chapter5:

f Lens focal point

l Setup height

D_a Setup aperture diameter

R_{pad} Pad radius

R_{sph} Curvature radius of the holder

t Backing layer thickness

μ_x The average of the image x

μ_y The average of the image y

σ_x^2 The variance of the image x

σ_y^2 The variance of the image y

σ_{xy}^2 The covariance of x and y

c_1 **and** c_2 Variables to stabilize the division

C_m Centre of the misaligned contact

RGB Color model: Red Green Blue

PADC Poly (allyl diglycol carbonate)

Chapter 6:

F_{pl} Preload

ρ Range of adhesion

$\mathbf{q}$ wavevectors

q Magnitude

γ Surface energy

$\tilde{\gamma}$ Dimensionless surface energy

a Punch radius

h Thickness of the PDMS film

ω Frequency

$E(\omega)$ Frequency-dependent Young's modulus

E^* The contact modulus

$v_{\mathbf{ela}}^{\mathbf{full}}$ The areal elastic energy in full static contact

λ Wave vector

$z(x, y)$ Single-wavelength corrugation

$v_{\mathbf{ext}}$ Velocity of the indenter

τ Relaxation time

t Displacement time

(K_n,η_n) Maxwell elements: stiffness and damping

(K_0,η_0) Kelvin-Voigt elements

N Number of Maxwell elements

m Inertia mass

$\tilde{u}$ The spatial Fourier transform of the displacement field

$\tilde{f}$ The spatial Fourier transform of the external force

$\tilde{G}$ Green's function

$\Gamma(g)$ The interaction potential

$g(x, y)$ The gap

CZM Cohesive zone model

CPU Central Processing Unit

CG Conjugate gradient

BAMs Bearing-area models

Contribution of co-authors

The research leading to these results has received funding from the Leibniz Competition Grant MUSIGAND (No. K279/2019) awarded to Eduard Arzt.

Details of the contributions of all co-authors to the individual chapters are acknowledged in the following.

Published chapters

Chapter 3 was published in peer-reviewed journals.

Samri, M., Thiemecke, J., Prinz, E., Dahmen, T., Hensel, R., & Arzt, E. (2022). Predicting the adhesion strength of micropatterned surfaces using supervised machine learning. Materials Today, 53, 41-50.
The article is available under: `https://doi.org/10.1016/j.mattod.2022.01.018`

Manar Samri : Conceptualization, Methodology, Investigation, Software, Writing-Original draft preparation. Jonathan Thiemecke: Software, Investigation. Eva Prinz: Investigation. Tim Dahmen: Review & Editing. René Hensel: Conceptualization, Methodology, Supervision, Writing - Original Draft. Eduard Arzt: Supervision, Writing- Review & Editing, Funding acquisition.

Planned manuscript

Chapter 4 is a planned manuscript.

Manar Samri : Conceptualization, Methodology, Investigation, Software, Writing-Original Draft. Jonathan Thiemecke: Software. René Hensel: Supervision, Conceptualization, Writing - Review & Editing. Eduard Arzt: Supervision, Conceptualization, Writing- Review & Editing, Funding acquisition.

Chapter 5 is a planned manuscript.

Manar Samri : Conceptualization, Methodology, Investigation, Software, Writing-Original Draft. René Hensel: Supervision, Conceptualization. Fabian Faller: Methodology, Investigation. Peter Rogin: Supervision, Conceptualization, Writing - Review & Editing. Eduard Arzt: Supervision, Conceptualization, Writing-Review & Editing, Funding acquisition.

Chapter 6 is a planned manuscript in collaboration with "The material simulation group" of the Department of Materials Science and Engineering at Saarland University, with the two first authors: Christian Müller and Manar Samri .

Christian Müller: Conceptualization, theoretical and numerical investigation, Simulations, Writing- Original Draft. Manar Samri: Conceptualization, Experimental methodology and investigation, Writing- Original Draft. René Hensel: Conceptualization, Supervision. Eduard Arzt: Conceptualization, Writing- Review & Editing, Funding acquisition. Martin Müser: Supervision, Conceptualization, Writing- Original Draft.

Table of Contents

Chapter 1

Introduction

In this new era, biomimicry has been a source of transformation [1]. It has greatly benefited the scientific and industrial revolutions. In contrast to humans, nature does not produce waste nor consume energy to create. Therefore, rather than only taking from nature, humans started learning from it.

"*We must draw our standards from the natural world. We must honor with the humility of the wise the bounds of that natural world and the mystery which lies beyond them, admitting that there is something in the order of being which evidently exceeds all our competence.*"
-VACLAV HAVEL, president of the Czech Republic [2].

In the materials science world, the need to move away from energy- and resource-intensive linear economy has pushed scientists to dig into the biology of animals, insects, and plants to extract new insights and ideas [1, 3, 4]. After years of research, the mystery of multiple abilities and functionalities of these biological materials is finally pierced, paving the way for multiple technological innovations and medical applications.

A remarkable characteristic of the biological materials is the resulting functionalities such as adhesive properties, optical appearance, wettability, and self-healing properties. These functions are the result of an optimization process of the biological materials during evolution. The multiple functions of biological materials are primarily expressed at the interfaces, to help maintain stable internal conditions despite a variable and hostile external environment. There are three dimensions to understanding these functionalities: the chemical composition (molecular scale), the nano- or microstructuring (nano- and micrometric), and the architecture of the surface (macroscopic). However, in many cases, this

complexity often exceeds the three levels classification by the interweaving of structures at all scales.

For adhesion properties in living materials, the most spectacular is the adhesive system found on the gecko. The first scientific observation on this dates back to Aristotle in the 4th century BC, where he noted: "*...run up and down a tree in any way, even with the head downwards*" [5]. Since then, geckos have never ceased to arouse the curiosity of many scientists. In fact, the gecko can move at speeds 20 times its length per second, climb smooth and rough surfaces, and even walk on ceilings. The answer to the riddle behind these abilities resides in the shape and architecture of its toe pads. A closer look at the gecko's toes showed a hierarchical fibrillar structure that allows the formation of intimate contact with all types of surfaces, see **Figure 1.1 a** and **b**. As a result, a low-intensity electrical dipole interaction occurs at short distances between atoms and/or molecules corresponding to the van der Waals force.

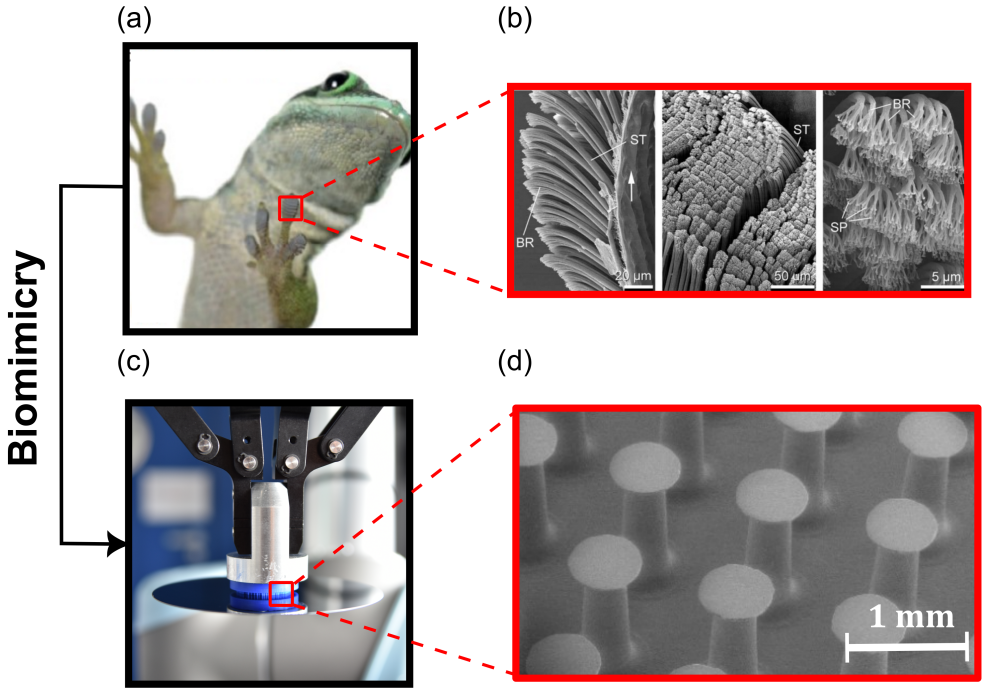

Figure 1.1: Biomimicry: from gecko adhesive system to a functional gripper for handling application. **a)** Image of a Gecko (Phlesuma nigristiata). Reproduced from [6]. **b)** The hierarchical adhesive system on the gecko's toe. Reproduced from [7]. It consists of aligned lamellae; each lamella contains microscopic hair-like fibrils (setae) which also split into smaller nanoscopic spatulae. **c)** Gecko-inspired gripping system. **d)** Scanning electron image of the synthetic fibrillar structure.

Inspired by gecko biology, a new generation of fibrillar dry adhesives has been developed, **Figure 1.1 d**. Over the past two decades, the design of high-performance fibrillar structures has come a long way. Scientists first focused

on understanding the principles behind gecko-inspired adhesives [8–13], then on optimizing the properties, geometry, and shape as well as developing new manufacturing processes [14–17]. Eventually, it became evident that the switchable and strong adhesion offered by these structures can open a wide range of applications such as robotics, handling systems (**Figure 1.1 c**), biomedical and space applications [6].

The present thesis solves challenges to the use of gecko-inspired structures as grippers for object handling. In fact, the nano and micropatterning of polymeric materials has shown great potential as new gripping technology. With residue-free, reversible adhesion, these structures can overcome various limitations of traditional gripping systems. In addition, they can be used without an external source of energy such as electricity or vacuum, showing an eco-friendly and sustainable performance.

There are, however, several issues associated with using these structures as grippers. Due to their short range, van der Waals forces can be adversely affected by the loss of intimate contact with the target surface. This can be a result of interfacial defects, roughness, or contamination in addition to alignment imperfections. Thus, these inconveniences can compromise the adhesive strength and lead to unwanted detachment, which makes it hard for the reliable handling promise to come true.

As the industry moves further into the automation age, any failure in the process can be costly. Therefore, finding a way to avoid or correct the above-cited limitations is crucial for integrating these structures into an industrial application. A first step towards improving the reliability of gecko-inspired gripping systems is to monitor and predict the adhesion performance. Taking advantage of the emerging capabilities from *in-situ* observation, machine learning, and simulation techniques, this work introduces different approaches to predict the adhesion performance from the contact signature.

This dissertation is divided into seven chapters. **Chapter 2** is a review of the theory and state of the art to provide the reader with the current knowledge related to this project. **Chapters 3 to 6** each represent a different approach to monitoring and predicting the adhesion from the contact signature: **Chapters 3** and **4** introduce a monitoring system using *in-situ* observation techniques, image processing, and machine learning models. **Chapter 5** is dedicated to the development of new optical techniques that will allow the *in-situ* observation of the contact and detachment of fibrillar adhesives with different types of surfaces. Simulation is used in **Chapter 6** to predict the contact signature of soft polymer films in contact with roughness-like surface topography. A conclusion and an outlook on further developments are offered in the final **Chapter 7**.

Chapter 2

Literature Review

2.1 Adhesion and bioinspired adhesives

2.1.1 Adhesion mechanisms in nature

Adhesion is a physico-chemical phenomenon with great importance in different engineering and research areas. It was defined by Kendall as the interaction between two surfaces which leads to a finite separation force [18]. Theoretically speaking, two surfaces in very close proximity (generally less than 1 nm) will attract and adhere to one another due to chemical and/or physical interactions [19] as shown in **Figure 2.1**. Nevertheless, not all surfaces in contact effectively adhere to each other, given that the real contact area between two surfaces is an extremely small fraction of the apparent contact area [20].

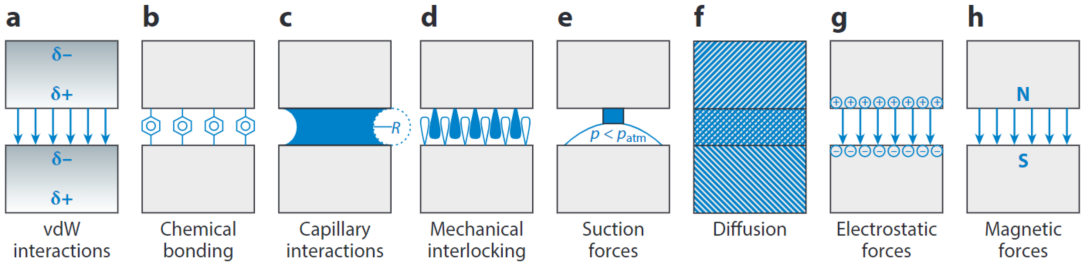

Figure 2.1: Attachment mechanisms. **a)** van der Waals interactions, **b)** chemical bonding, **c)** capillary interactions, **d)** mechanical interlocking, **e)** suction forces, **f)** diffusion of one surface material into the other, **g)** electrostatic forces, and **h)** magnetic forces. Reproduced from [21].

Evolution has permitted the development of multiple effective and versatile adhesive systems in numerous animals and insects to overcome the small contact area limitations and adapt to their environments [1, 6]. The understanding of these mechanisms and the attachment forces behind them was a crucial factor for the upgrading to new generations of adhesives.

For example, capillary forces were found to be the main mechanism that allows spiders, many beetles, and ants to freely move on walls and ceilings, **Figure 2.1 c**. These insects are able to support their own weight, even when carrying proportionally quite heavy objects. The attraction between two objects through capillary forces is mainly due to the Laplace pressure and the surface tension of the liquid. It is manifested when the liquid on the interface forms a capillary bridge between the two surfaces [21]. Inspiration from insects such as the leaf beetle, whose adhesive strength exceeds 100 times its body weight (circa 33 mN), led to the development of capillary-based switchable adhesives that can be potentially integrated in different applications [22, 23].

The suction mechanism employed by some underwater animals such as the octopus [24, 25] can be considered one of the essential mechanisms adopted by nature for reversible underwater adhesion, **Figure 2.1 e**. Octopus suckers generate a pressure difference in a few milliseconds which can produce a high adhesion force [26]. This has inspired the development of different suction cup-based adhesives for both in-air and underwater applications [27–30].

Similarly, snails and other mollusks have solved the adhesion problem by generating a sticky mucus that allows them to maintain conformal contact with the surfaces. Upon drying, an epiphragm is created where the shear modulus goes from 100 Pa to 1 GPa, allowing a strong attachment to the target surface [31].

The impressive adhesion force in reptiles such as geckos was linked to van der Waals interactions [8, 9], **Figure 2.1 a**. It is considered a short-range force that can be very strong over small distances between atoms and molecules [32]. Van der Waals force consist of three different types of interactions: dipole-dipole interaction, i.e. Keesom energy (E_{keesom}), with a typical bonding energy $< 20\ kJ\ mol^{-1}$; dipole-induced dipole interaction, i.e. Debye energy (E_{Debye}) $< 2\ kJ\ mol^{-1}$; and dispersive interaction, i.e. London energy (E_{London}) in the range $0.1-40\ kJ\ mol^{-1}$ [19, 32]. The total energy of the van der Waals forces is the sum of the energy of these three interactions.
The attractive van der Waals energy between two atoms is inversely proportional to the sixth power of their separation ($1/r^6$), i.e., the shorter the distance between the adherents' molecules the stronger the energy and the higher the attraction between them. However, if the distance between the two molecules is too small that their atoms' positive nuclei repel, a large repulsive force will be generated, which will result in an equilibrium distance [32]. In the case of van der Waals attraction between macroscopic bodies, other factors affect the total energy such as the geometry of the objects [32].

2.1.2 Bioinspired fibrillar dry adhesives

Biomimetics has become an immensely powerful approach for the development of new technologies. One of the many interesting biological systems that intrigued scientists over the last decades is the ability of some insects and animals to climb vertical walls with a fast attachment and detachment mechanism within milliseconds on various types of surfaces, i.e., wet or dry, smooth or rough, hard or soft. The understanding of the adhesion mechanisms in such animals led to the development of a new generation of adhesives with exceptional new properties [5].

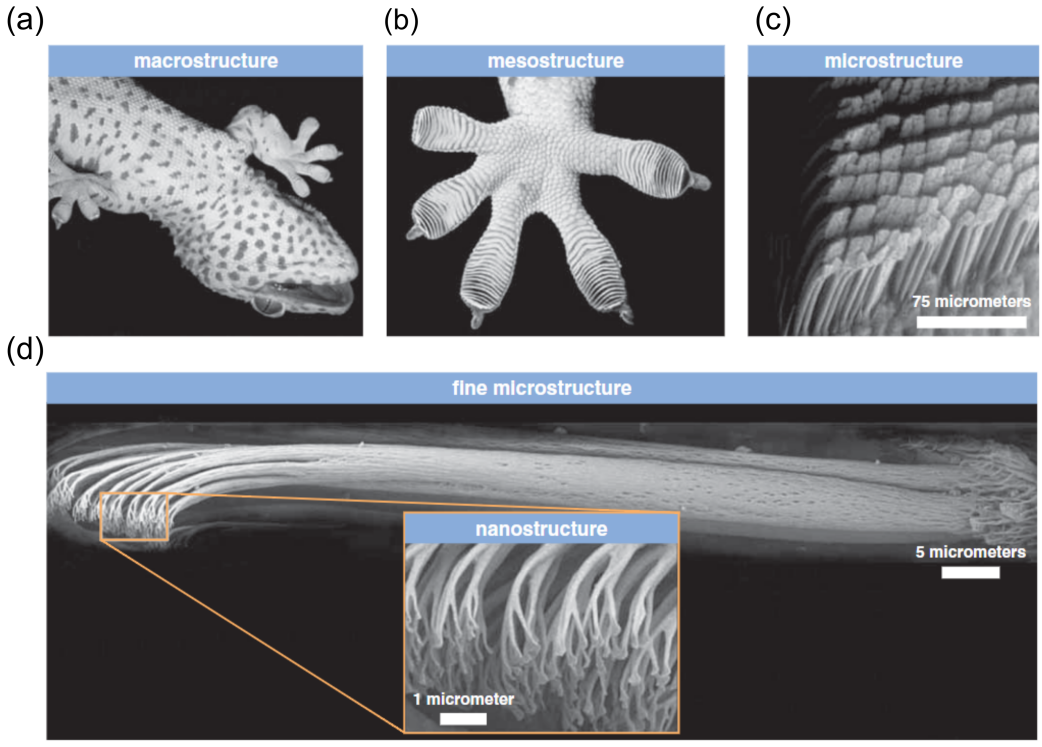

Figure 2.2: The complex hierarchical structure, of the gecko toe pads. **a)** Macroscopic image of a gecko, **b)** shows the foot of the gecko. **c)** and **d)** show Scanning Electron Microscopy (SEM) images of the hierarchical structure. It consists of aligned lamellae; each lamella contains microscopic hair-like fibrils (setae) which also split into smaller nanoscopic spatulae. Figure reproduced from [11].

The most fascinating adhesive system is found on the gecko's toe pads. Lizards such as the geckos are the heaviest living objects on this planet that are able to adhere to ceilings [20]. In fact, the gecko's adhesive system operates under the most severe conditions (rough, smooth, vertical, contaminated surfaces and ceilings) due to its hierarchical structure. Gecko's toe pads contain multiple lamellae that are lined with small structures called setae, which are approximately 100 microns long and 5 to 10 microns wide. Each seta contains at its end hundreds of even smaller structures called spatulae, with a diameter of about 200 nm

[33], see **Figure 2.2**. The first theories to explain the binding forces behind the gecko's strong adhesion suggested that the hair-like fibrils attach through capillary forces [34] and van der Waals forces [8]. However, investigations by Autumn *et al.* [8,9] rejected the theories of wet adhesion by capillary forces. They argued based on their studies on gecko hairs in contact with hydrophobic surfaces that van der Waals interactions were solely responsible for adhesion. Later Atomic force microscopy (AFM) experiments by Huber *et al.* [35] demonstrated that the spatulae pull-off forces increase in the presence of humidity. They concluded that in that case, capillarity can contribute equally to adhesion.

Adhesion tests on a single seta revealed that it can support a maximum load of about 200 µN. Knowing that a gecko has between 6 and 7 million setae, means that it could theoretically support a maximum load of 130 kg [8]. The shape and orientation of the seta play a big role in the detachment mechanism for the geckos as the adhesion ceases as soon as the seta is inclined with respect to the surface. This mechanism was later exploited also in handling processes.

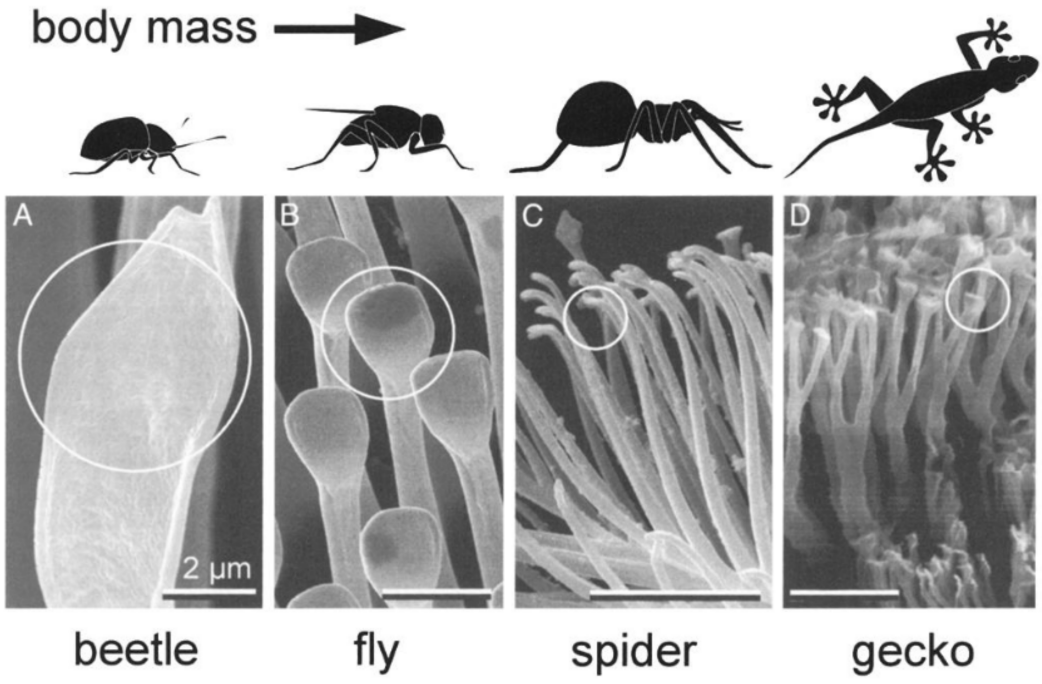

Figure 2.3: SEM images displaying the size variation of the fibrils with the body mass of different animals illustrated above. The heavier the animal, the finer the structures. Reproduced from [10].

Arzt *et al.* [10] found that the density of adhesive fibrils is correlated with body mass in various insects and animals, such as beetles, flies, spiders, and geckos. As one can see in **Figure 2.3**, the heavier the animal is the smaller its fibrils are, and the higher the areal density is. Thus, the adhesive strength of these structures increases when the size of their fibrils decreases and the number

increases. This assumption was justified by contact mechanics theory and was interpreted by the principle nowadays known as 'contact splitting' [10], which is considered a governing mechanical principle behind the bioinspired microfibrillar adhesives.

2.1.3 Factors influencing the adhesion of fibrillar structures

The adhesion strength of fibrillar structures can be influenced by various factors and the optimization of their performance can be linked to different parameters. The following sections will discuss the most important factors affecting their efficiency.

2.1.3.1 Material and design effects

Since the first attempts to mimic fibrillar adhesives, it has been shown that the shape, size, and aspect ratio have a big influence on the adhesion performance of the patterned structure [1]. Several studies have shown that mushroom-like fibrils exhibit improved performance when compared with flat punches, by more than an order of magnitude [15,21,36,37]. Detailed numerical calculations showed that, by adding a mushroom cap, the stress singularities at the edge are released and transferred to the center of the fibril [17, 38, 39], see **Figure 2.4 a** and **b**. As a result, this design can be more tolerant of interfacial defects. Besides the shape of the fibrils, it was found that adhesion strength increased by decreasing the aspect ratio of the fibril [40]. However, a reduced aspect ratio could lead to an increase in stiffness, which negatively impacts the tolerance to misalignment and surface roughness [6, 40, 41].

Furthermore, the properties of the materials used in the fabrication have a great impact on the adhesion behavior of these structures. The most commonly used materials are elastomers with an elastic modulus lying between 1 and 100 MPa. A scaling relationship between the adhesion strength and the elastic modulus is predicted by fracture mechanics models [42] as presented in **Eq.2.1**

$$\sigma \approx \sqrt{\frac{G_c}{AC}} \approx \sqrt{\frac{G_c E}{d}} \tag{2.1}$$

with σ the pull off stress, G_c the energy release rate, A the contact area, C the contact compliance, E the elastic modulus, and d the contact diameter.

Using gradient structures in ladybugs as inspiration, scientists have developed composite fibrils that combine soft and stiff materials to increase adhesion and compliance to rough surfaces. [43–45], **Figure 2.4 c**.

Overall, the choice of the different design parameters is dependent on the working conditions of the adhesives. For this purpose, multiple studies have been conducted to design a map for the prediction and optimization of these parameters [16, 46, 47].

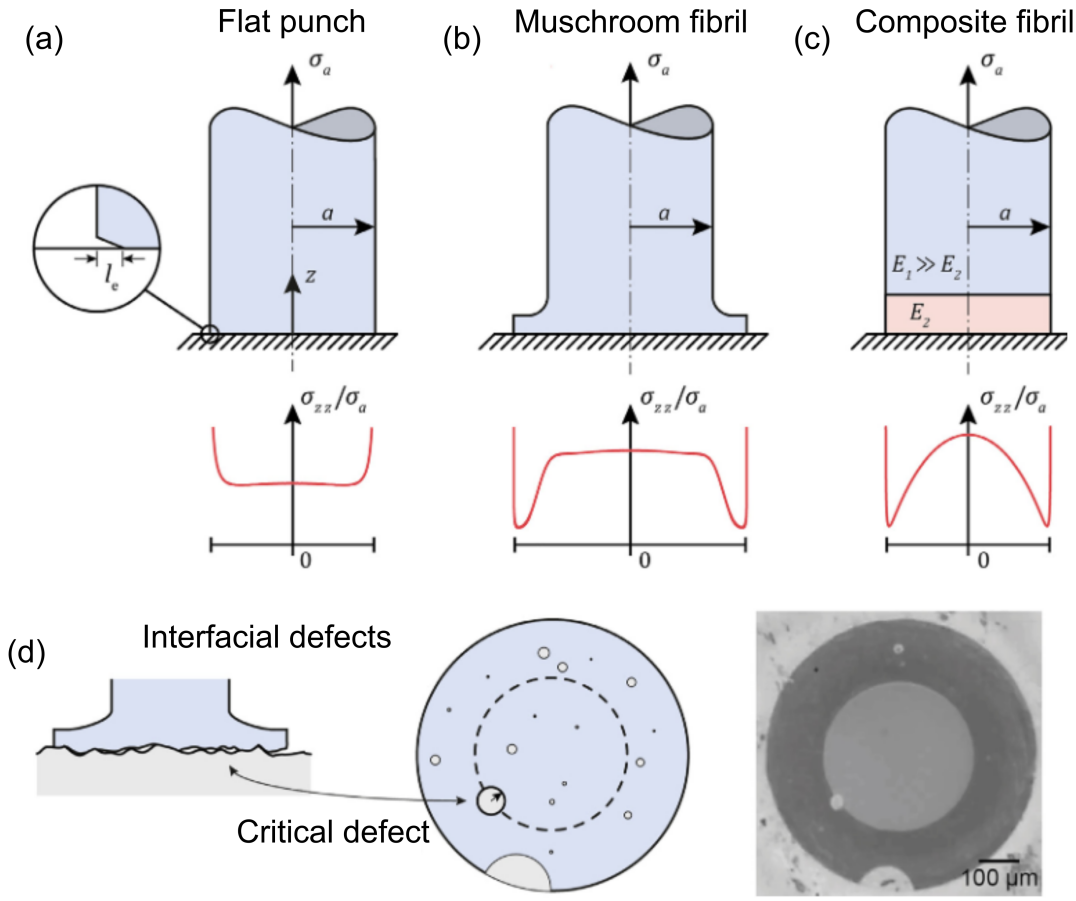

Figure 2.4: Illustration of the contact of the fibrillar micropatterned surface. Figure reproduced from [48]. a-c) Schematic drawing show the contact of single fibril with the target surface and the corresponding stress distribution for **a)** flat punch **b)** mushroom fibril **c)** composite fibril **d)** A realistic image of the contact and the analogous drawing showing multiple interfacial defects due to roughness/contamination.

2.1.3.2 Contact imperfections

Contact imperfections can adversely influence the adhesion strength of the bioinspired structures either on the array or single fibril scales.

At the fibril level: Van der Waals forces, being short-range interactions, decrease strongly with increasing distance to the target surface. Thus, the geometry of the contact surface and roughness drastically influence the strength of these forces [49, 50]. Moreover, surface defects, dust, contamination, or trapped air bubbles at the interface can lead to very weak or no adhesion at the fibril

level. In fact, the small particles would limit proper contact formation between the fibril and the target surface as can be seen in **Figure 2.4 d**, which would weaken the intermolecular interactions [51, 52]. The random variation of the defects' size and position can also result in a variation of the pull-off strength across the array [48].

At the array level: The alignment imperfections of the adhesive pad with the target surface and the fabrication-induced defects such as waviness or non-uniform height distribution of the fibrils can dramatically affect the adhesion [53–55]. Due to the uneven load distribution caused by these problems, local detachments occur at the defective area and propagate as a peeling effect. Experiments conducted by Booth *et al.* [54] have confirmed that even a small misalignment, of the order of 0.1°, will lead to peeling and to a significant drop in the adhesion strength. The peeling effect due to misalignment is also dependent on numerous adhesive design parameters such as the compliance and thickness of the backing layer, the array size, the aspect ratio of the fibril, and the fibril-to-fibril distance [53].

2.1.3.3 Environmental factors

Environmental conditions such as temperature or humidity can have an effect on the adhesion of fibrillar elastomers [1, 50, 56, 57]. Temperature can alter the mechanical properties of materials, resulting in large variations in adhesion strength [56]. The presence of humidity and water, on the other hand, weakens van der Waals interactions. In contrast, suction and capillary forces may become dominant [57].

2.1.3.4 Testing conditions

Testing the adhesion strength of bioinspired microstructures is crucial for quantifying and predicting the quality of their performance [58]. In general, the testing methods used fall under two categories, load-controlled measurements, and displacement-controlled measurements, with the latter being the most commonly used. However, it has been shown that the testing conditions using displacement-controlled measurements do not always correspond to real-world circumstances as they can impose geometric deformations that would not be seen in applications. These resulting deformations significantly affect adhesion properties in ways that are hard to predict [59].

2.1.4 Statistical properties of the fibrillar structures

In the early studies of the bioinspired fibrillar structures, it was assumed that the adhesive force of an array was the sum of the strength of individual fibrillar contacts. However, fibrillar structures tend to exhibit inevitable fabrication or contact defects as mentioned in section **2.1.3.2**, causing an uneven distribution of the adhesive strength across the array. To determine the adhesion strength statistics, Porwal *et al.* [60] implemented Monte Carlo simulations. Using probability distributions for the fibrils length and attachment strength, they concluded that increasing variations decreased the adhesive strength. McMeeking *et al.* [51] hypothesized that the detachment is governed by defects in the fibrils, following the statistical theory of fracture [61]. These ideas were later extended by Tinnemann *et al.* [62] and Booth *et al.* [48, 63], who developed a bimodal statistical theory based on the Weibull distribution. The Weibull distribution was found to be consistent with the empirical strength distribution obtained by correlating the time of detachment to the elongation of the single fibrils.

The cumulative Weibull distribution function is given by **Eq.2.2**.

$$\frac{N_d}{N} = 1 - \exp\left\{\left[-\left(\frac{u}{u_0}\right)^m\right]\right\} \tag{2.2}$$

where N is the total number of fibrils, N_d the number of detached fibrils, u the elongation, u_0 the reference elongation at detachment, and m the Weibull modulus. Thus, small Weibull moduli correspond to a large variation in adhesion strength values and vice versa.

Hensel *et al.* [64] demonstrated the use of the statistical Weibull distribution to characterize the fibrillar adhesives strength distribution, where the parameters m and u_0 can provide specific properties for each structure.

2.1.5 Fibrillar adhesives applications

In the last decades, we have gained a considerable amount of knowledge and understanding of the bioinspired adhesives, which enabled their initial transfer to different applications, see **Figure 2.5**. One of the first application that emerged was the climbing and crawling robots that mimic the behavior of geckos [65, 68–75]. These robots can be used for different applications such as inspection and maintenance of tall buildings, large ships, or even spacecrafts. Another potential space application of the bioinspired adhesives is the grasping of the rocket bodies and debris floating and orbiting the Earth [68, 74]. The wide range of materials used to fabricate the fibrillar adhesives structures has also facilitated their integration into biomedical applications. As a result, various innovative

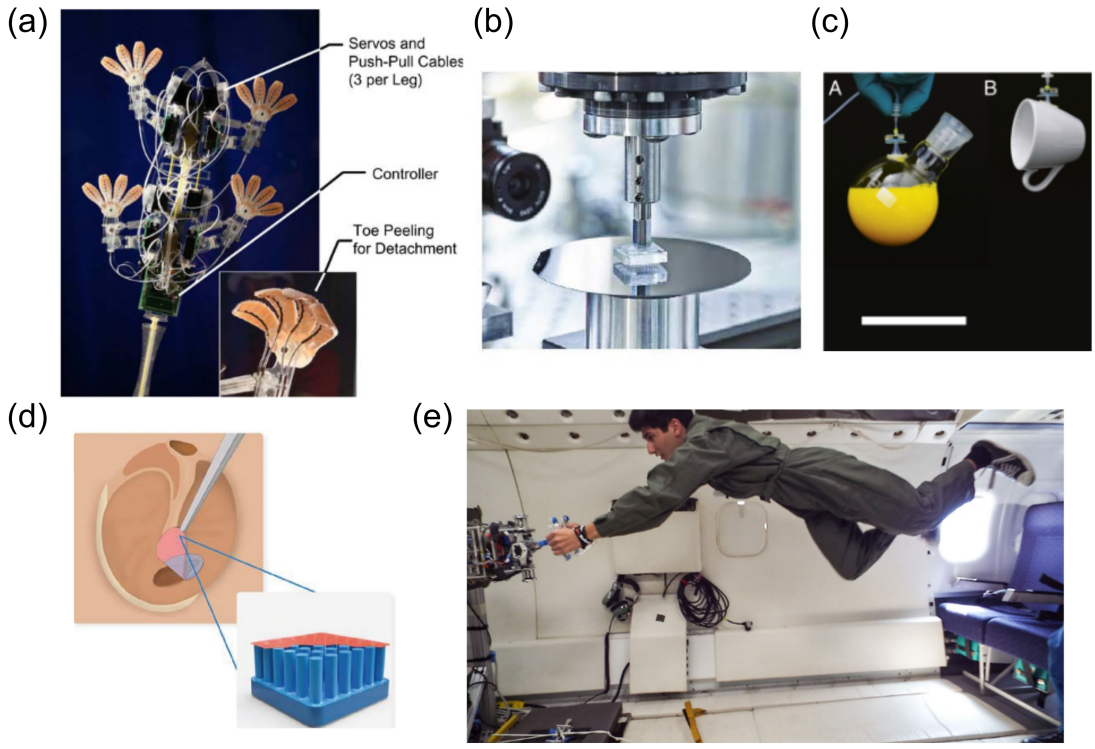

Figure 2.5: Application of fibrillar adhesives. **a)** Stickybot, bioinspired robot for climbing smooth surfaces [65]. **b)** Reversible pick-and-place handling of fragile silicon wafers [6]. **c)** Soft adhesive gripping system holding 3D objects [66] (A) round glass flask, (B) coffee cup . **d)** Schematic drawing of the film terminated microfibrillar adhesive for eardrum-perforation repair [1, 67]. **e)** An autonomous multi-unit gripper with gecko-inspired directional microwedge adhesive anchoring to a carbon fiber panel in zero gravity [68].

applications have been developed, for instance, fibrillar adhesive-based wound healing band-aids, see **Figure 2.5 d**, controlled drug release, or sensor attachment to the human body [67, 76, 77].

Additionally, fibrillar adhesives can be integrated in the pick and place application for object handling as an alternative to the traditional gripping systems. The use of fibrillar structures as gripping devices demonstrated multiple advantages for grasping flat and fragile objects of different sizes in both air and vacuum conditions [6, 78–80]. The release mechanism in the case of the pick and place application is as important as the attachment. The established concept for release is to use mechanical actuation. Compressive overloads, for instance, induce an elastic instability due to the fibrils buckling, which initiates detachment [81–83]. Other concepts to switch adhesion is to use materials and components where the bending of the structure is actuated by temperature, magnetic field, or UV light [84–87].

2.2 Adhesion to rough surface

The importance of adhesion in nature and technology is indisputable. As mentioned in section **2.1.3.2**, the presence of surface roughness weakens strongly the adhesive bonds and in some cases leads to total suppression of adhesion due to a reduced intimate contact [88]. Surface roughness exists on different length scales, even on highly polished surfaces [89]. The first approach to study adhesion to rough surface dates back to the 1970s with the classical paper by Fuller and Tabor [88]. In their work, Fuller and Tabor provided an approximate solution for the understanding of adhesion to rough surfaces. They developed a model where surface roughness is presented as high asperities with the same radius of curvature and height following the Gaussian distribution. By applying the Johnson-Kendall-Roberts (JKR) contact theory to each asperity, they were able to obtain the total contact force. Persson [89] argued that this simplistic model works only for an exceedingly small real contact area and that the assumption of roughness on single length scale does not represent the reality of rough surfaces. Subsequently, Persson [89–92] proposed a model that considered the roughness on different length scales and presented numerical results for multiple cases such as self-affine fractal surfaces.

Load displacement curves obtained from indenting an elastomer show an adhesion hysteresis i.e., work of adhesion. It results from the presence of the small asperities that jump into or snap out of contact as the surface of the elastomer becomes unstable [30]. Modeling this adhesion hysteresis in the presence of roughness can certainly improve the optimization of adhesive structures and the prediction of adhesion properties.

Different numerical strategies were adopted to tackle the adhesive contact challenge [93]. In the context of this thesis, Greens Function Molecular Dynamics (GFMD) was developed by Campañá *et al.* [94] where they implemented a molecular dynamics methodology to model semi-infinite elastic solids and their application to various contact mechanic problems based on a Green's function. In the first application of the GFMD they were able to model self-affine contacts accurately following Perssons's theory [94]. However, it was only used for nonadhesive contact. Thereafter, Carbon *et. al* [95, 96] developed a numerical procedure based on Greens function to analyze the adhesive contact between a soft elastic layer and a rough rigid substrate. Müser *et. al* [30, 97–99] continued the development and the extension of the GFMD. As a result of the further developments, the thickness of the elastomer became explicitly included instead of assuming semi-infinity [97]. Further extensions have been later developed to account for the variation of the materials elasticity [99] and viscoelasticity [100].

In this work, simulations by GFMD (performed by Christian Müller in his thesis) will be compared with experimentally observed dependencies of the contact between a viscoelastic film and a cylindrical punch with a single wavelength, small-scale roughness.

2.3 Adhesive fibrillar contacts: the concept of "contact signature"

During the last century, scientist have developed high contrast observation techniques for the inspection of the interface and the contact between two surfaces. These techniques allowed the extraction of the "contact signature", which delineates the contact from the non-contact regions and encompasses various features of the contact.

The most used approach to extract the contact signature between surfaces is the inverted optical microscope. The use of optical lenses allows a magnified observation of the contact between the object and a transparent target [101, 102]. The resolution and contrasts obtained with optical lenses were however found insufficient for different applications and studies, particularly for micro- and nanoscale contact observation. The need for higher contrast between the contact and non-contact areas for more precise results has pushed scientists to develop and implement new techniques.

Phase contrast microscopy

One of the approaches used is the phase contrast microscopy developed by physicist Frits Zernike [103]. This technique allowed the generation of high-contrast images of transparent specimens. In fact, the phase contrast technique converts phase variation into changes in brightness and amplitude, which are then observed as differences in contrast. In order to intensify the contrast between contact and non-contact areas, Dyson and Hirst used this technique for observing the contact between a metallic sheet and a transparent glass [104]. The phase contrast microscope allowed them to visualize deformations at the glass surface with a few Ångstroms in depth (when the lateral extension was above the resolution limit of the microscope).

Frustrated total internal reflection, FTIR

Another technique used by Harrick [105] and McCutchen [106] for the observation of surface topography, is the frustrated total internal reflection (Frustrated Total Internal Reflection (FTIR)). It is based on the principle of total internal reflection, which occurs when an incident ray strikes an interface that separates a more refractive medium and a less refractive medium at an angle greater than the limit angle. The first experiments by Harrick [105] have shown that the penetrating power can be absorbed or diverted if a contact of the absorbent with a high index material occurs, i.e., the internal reflection is frustrated. FTIR has

proved to be a reliable technique for contact observation. In the context of the present thesis, it was used by Eason *et al.* for the estimation of the stress distribution on gecko's toes [107]. They built an optical tactile sensor consisting of a force transducer that transforms the measured stresses to images using FTIR. Tinnemann *et al.* combined FTIR with an adhesion tester for *in-situ* observation of contact formation and separation of micropatterned adhesives [62]. Using this technique, they were able to investigate more closely the detachment behavior at the array and single pillars scale under different conditions, see **Figure 2.6**.

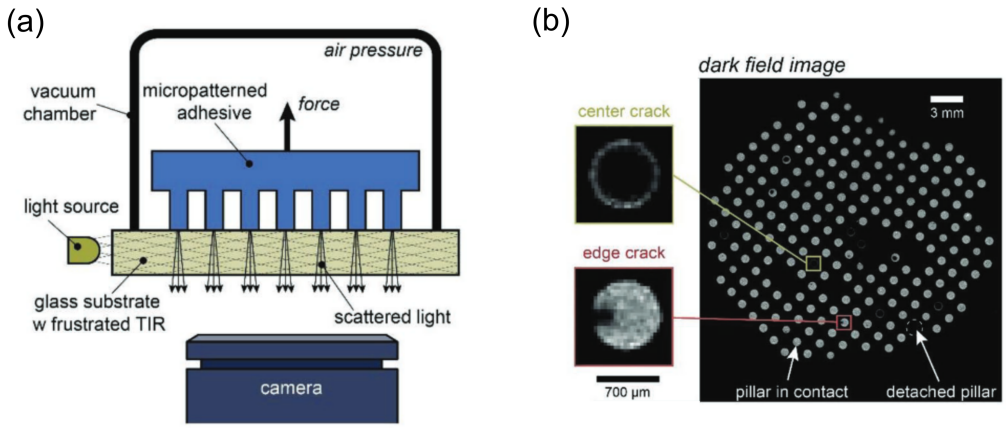

Figure 2.6: Application of FTIR for contact observation. **a)** Schematic illustration of the principle of FTIR for the use in *in-situ* observation of detachment mechanisms in micropatterned structures. **b)** Image of the contact between a micropatterned adhesive and a transparent substrate at the start of detachment, the small images show the two types of crack initiation at the pillars scale (center crack and edge crack). Reproduced from [62]

Interferometry

A third technique used for contact observation is interferometry. It is a family of techniques in which waves of different phases are superimposed, producing the phenomenon of interference. This interference is used in different fields of science to extract information. The optical interference observed as Newton's rings was employed by McCutchen [106] for contact examination. Newton's rings are a phenomenon that occurs when a spherical surface is in contact with a flat one. The interference pattern is created by the reflection of the light between two surfaces. The constructive and destructive interferences appear as a series of concentric alternating bright and dark rings around the point of contact. In fact, a destructive fringe of the 0th order will be observed at the center of the contact points between the two objects. When the objects are separated and the gap between them increases, the fringe pattern will alternate from dark to light and higher-order fringes will appear. This allows an observation of the contact and

detachment between the two objects. Using the interferometric technique, Krick *et al.* developed an *in-situ* optical micro tribometer to investigate the intimate contact between solids during loading and sliding experiments [108]. Federle employed Interference Reflection Microscop (IRM) to investigate the adhesive contact mechanism in different biological organisms [109–111].

Coaxial illumination

Coaxial illumination is a method that was developed to enhance the contrast by improving the illumination of the specimen. It consists of a beam splitter which redirects light from the light source and projects it onto the object parallel to the optical axes of the camera, as can be seen in **Figure 2.7**. This technique was employed in different fields for process control and contact observation [112–114].

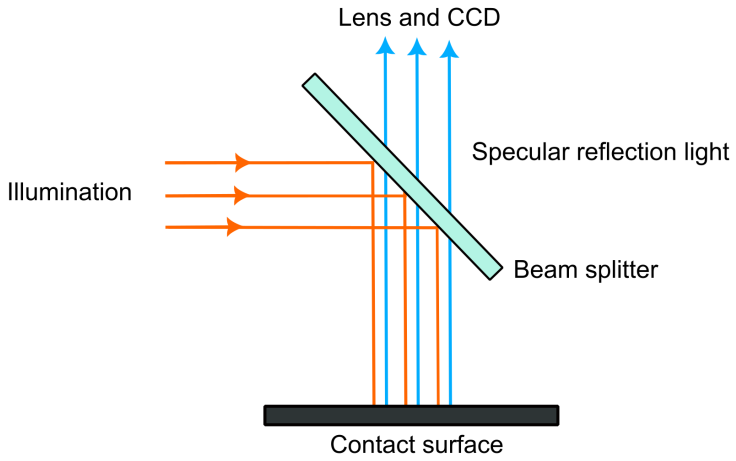

Figure 2.7: Schematic of the coaxial illumination principle [115]

In the present thesis, FTIR was employed in **Chapter 3** and **4** for obtaining the contact signature of fibrillar adhesives. **Chapter 5** introduces new optical devices to observe the contact of the fibrillar microstructures with opaque and rough surfaces. The coaxial Illumination technique was used in **Chapter 6** to enhance the contrast of the contact signature of a cylindrical punch with roughness-like surface and a viscoelastic film.

2.4 Machine learning

2.4.1 Definition and categories

Machine Learning (ML), is a subset of Artificial Intelligence (AI), with the first algorithm "the perceptron" created in the late 1950s [116]. It is a modern science based on mathematical and statistical approaches, pattern recognition, and predictive analyses. It gives the computers the ability to "learn" from the data and give data-driven predictions, recommendations, and decisions without being explicitly programmed [117]. Over the last few decades, ML has become a powerful tool used in different scientific areas. It has proven to be more efficient than traditional techniques for creating correlations in large sets of diverse and changing data. Its powerful abilities have become a huge part of our daily life and the areas of application are increasing remarkably, from web searches [118], email/spam filtering [119], personalized advertising [120], image and speech recognition [121] to self-driving cars [122]. Recently, materials science and engineering has benefited greatly from the progress of ML algorithms for discovering new materials, the prediction of materials properties and materials design optimization [123–126].

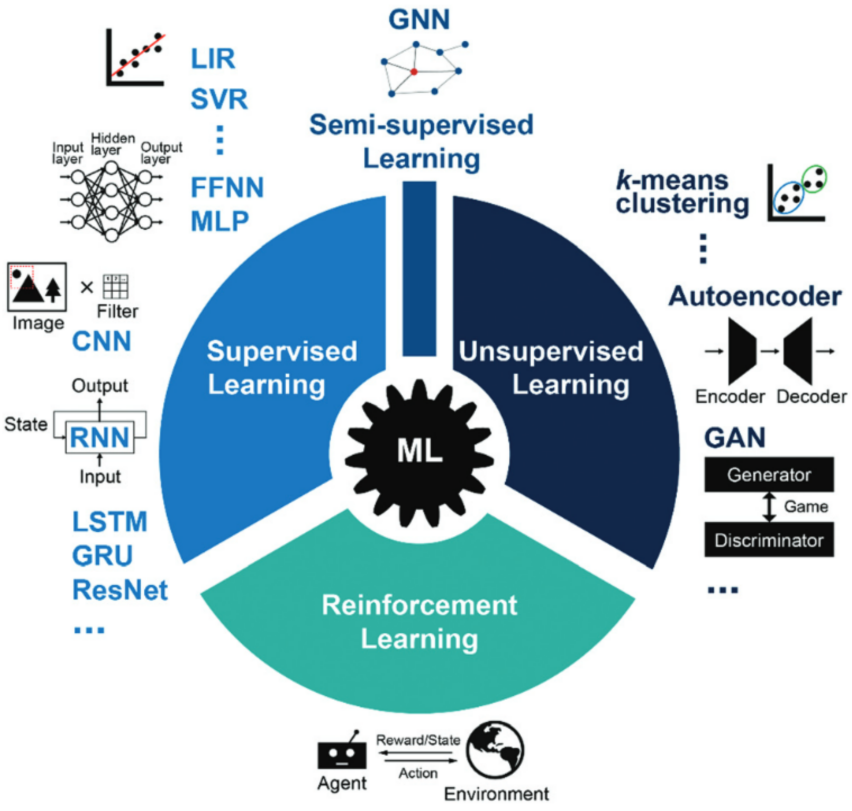

Figure 2.8: Major categories of machine learning. Reproduced from [124].

ML approaches can be divided into different categories [117], **Figure 2.8** [124]:
Supervised learning: A predictive model where the goal is to map the unknown function that connects an input x to an output y, given patterns found in a labeled set of input-output pairs, i.e., the training data. The used training data, D, for supervised learning, is constructed from N input/output duos [117] such as:

$$D = (x_i, y_i)_{i=1}^{N} \tag{2.3}$$

Supervised learning problems fall into two categories:

- **Regression**: When the output to be predicted is a value in a continuous set of reals $y \in \mathbb{R}$, we speak of a regression problem. It is mainly used for predicting and determining cause-and-effect relationships between variables.
- **Classification**: The goal of the task in the classification approach is the prediction of a discrete class label, i.e., the set of the output values is finite $y = \{y_1, y_2, ..., y_n\}$. The resulting prediction function is then called a classifier. The simple cases are binary classifications with a yes/no answer, [126].

Unsupervised learning: Unlike supervised learning, unsupervised learning is based on finding natural patterns in unlabelled data (only from the inputs x) [117, 127]. D is composed from N input as follow:

$$D = (x_i)_{i=1}^{N} \tag{2.4}$$

Multiple techniques are used for this purpose such as Principal Component Analysis (PCA) [128] and clustering methods [129].
Semi-supervised learning: Halfway between supervised and unsupervised learning, semi-supervised learning combines both labeled and unlabeled data with the majority of the training data being unlabeled [130].
Reinforcement learning: Reinforcement learning relies on a reward system without the need for prior data [131]. It is used when feedback about good and bad choices is accessible for decision-making problems. Namely, the machine learns from interactions. One of the most famous reinforcement learning models is AlphaGo, in which the trained model was able to beat the world champion in Go game [132].

2.4.2 Models optimisation and evaluation

In this thesis supervised learning models will be used to create regression and classification predictive models. Regardless of the goal of the supervised learning task, it is usually recommended to follow specific processes in order to develop effective models. The most important steps are the correct partitioning of the data, model optimization, and evaluation. In this section, we present the different optimization and evaluation approaches used for the models in this project. A detailed description of the models will be given in section **2.4.3**.

2.4.2.1 Data partitioning and cross-validation

In machine learning methodology, evaluating a trained model and testing it on the same data is not advisable as it would lead to over-fitting problems. In the case of over-fitting, the model will show correct predictions on the used data but will fail to repeat the same high score on new unseen data. To avoid this, two approaches can be taken [133, 134]:

1. If the data is sufficient, a simple approach is to divide it into training, validation, and testing sets [135], see **Figure 2.9 a**. The data split should be defined randomly and without bias. The training set is used to define the different parameters of the trained model, these parameters are then compared to the ones obtained from the validation set. The parameters selected at the end are the ones with the best predictive performance. The model is finally tested and evaluated on the testing set as will be explained in section **2.4.2.2**.

2. When the data set available is limited, dividing it into three sets drastically reduces the number of samples used for learning the model. In that case, the resulting model would depend on the random choice of the training and validation sets. Thus, a K-fold cross-validation approach can be used for the training and the validation as illustrated in **Figure 2.9 b** [136]. In this case, the training data is partitioned into k groups. In each run, K-1 groups are used for training the model and 1 group is left for validation. In each iteration, the held-out group is changed. The final performance is calculated as the average of the K runs. The number of folds is chosen depending on the amount of data available. If the data set is extremely small, a leave-on-out technique can be used where K=N (with N the number of data). However, increasing the number of folds can be computationally expensive.

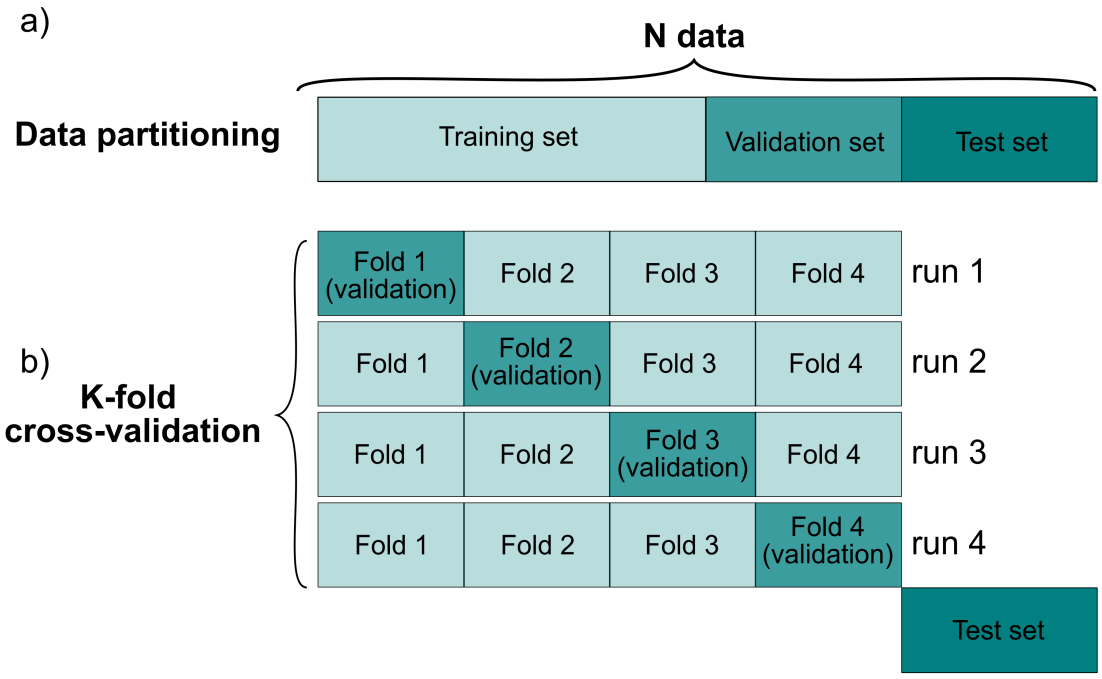

Figure 2.9: Data partitioning and cross-validation. **a)** Data partitioning into training, validation, and testing sets. **b)** K-fold cross-validation, with K=4 in this example. In each run, one of the four groups is chosen for the validation of the models parameters and the rest for training. A test set is left out for testing the model [134].

2.4.2.2 Models evaluation

For the creation of reliable predictive models, evaluation can be a crucial step. It helps in understanding and assessing the performance of the model, and can be a way to compare and choose between different models. For supervised learning models, various metrics can be used for evaluating the models depending on the approach.

Regression models evaluation

For evaluating and reporting regression models performance, three error metrics are commonly used:
R Square (R^2), calculated as:

$$R^2 = 1 - \frac{\sum_i (y_i - \hat{y}_i)^2}{\sum_i (y_i - \bar{y}_i)^2} \tag{2.5}$$

For a perfect prediction, $R^2 = 1$ (i.e., $y_i = \hat{y}_i$) . If the regression line is worse than when fitting the mean value, the calculated R^2 is negative. Although R^2 is a good way to determine how well the model fits the dependent variables, it does

not take the over-fitting problem into account.
Root Mean Square Error ($RMSE$) is the average magnitude of the error. It describes how well the data is concentrated around the fitted regression line.

$$RMSE = \sqrt{\frac{\sum_{i=1}^{n}(\hat{y}_i - y_i)^2}{n}} \tag{2.6}$$

$RMSE$ values range from 0 to ∞. With 0 representing the case of the perfect prediction. The units of the error score match the units of the predicted target value.
Mean Absolute Error (MAE), measures the error between the predictions and the real values such as:

$$MAE = \frac{\sum_{i=1}^{n}|\hat{y}_i - y_i|}{n} \tag{2.7}$$

Similarly to the $RMSE$ the lower the value of the MAE the better the predictions. with y_i the value of the i-th observation in the validation data, $\hat{y}_i$ the predicted value, $\bar{y}_i$ the mean of the observed data, n the number of observations.

Classification models evaluation

Classification models' performance is evaluated using various metrics calculated from:

- The True Positive (Tp) predictions, which represent the correct predictions of what are considered positive values (for example: in a binary classification of 1 and 0 classes, 1 is considered the positive class).
- True Negative (Tn), i.e. the correct prediction of the negative class (0).
- False Positive (Fp), i.e. the incorrect prediction of the positive class (the class is 0 and the prediction is 1).
- False Negative (Fn), i.e. the incorrect prediction of the negative class (the class is 1 and the prediction is 0).

The classification evaluation metrics used in this thesis are:
Accuracy: It represents the percentage of true results compared to the total number of cases examined, such as :

$$Accuracy = \frac{Tp + Tn}{Tp + Fp + Fn + Tn} \tag{2.8}$$

Even though the accuracy could inform about the quality of the predictions, it can be misleading if there is an uneven class distribution in the data. Thus, other

metrics should be also considered.
Precision (P): The precision is the positive predictive value. It is calculated as follows:

$$Precision = \frac{Tp}{Tp + Fp} \tag{2.9}$$

It is maximized when all the true positives are predicted correctly such as $Tp = Tp + Fp$. This means that high precision is associated with a low false positive rate.
Recall (R): also known as the sensitivity of the model. It calculates how many positive values the model was able to predict correctly from all the positive data.

$$Recall = \frac{Tp}{Tp + Fn} \tag{2.10}$$

The Recall value is maximized when $T = Tp + Fn$, i.e., the false negative values are minimized.
Score (F_1): The score takes into consideration both the precision and recall such as:

$$F_1 = 2 * \frac{P * R}{P + R} \tag{2.11}$$

2.4.3 Supervised learning models

In supervised machine learning, various linear and non-linear algorithms and computation techniques are used, whether for classification or regression tasks. Listed below are the methods applied to this project in **chapters 3** and **4**.

2.4.3.1 Linear Regression

Linear Regression (LnR) is the best known and understood algorithm in statistics and machine learning [133, 137]. The simplest linear regression type uses traditional slope-intercept $y = ax + b$, with x the input variable, a and b the coefficients that the algorithm will try to "learn" for an accurate prediction, and y is the prediction.
In applications, the input variable is usually more than one. A multivariable more complex equations can be then constructed such as:

$$y(x) = \sum_{j=1}^{D} w_j x_j + e \tag{2.12}$$

where w_j represents the j coefficients or weights, the model will try to learn and e is the residual error between the linear prediction and the true response. The goal of LnR is therefore to minimize the sum of the squares of the residuals to

find the best fit to the training data.
LnR has different assumptions that should be taken into consideration before use [117]:

- First, a continuous target variable ($y \in \mathbb{R}$).
- No collinearity between the different explanatory variables (x_j).
- A linear relationship between target and explanatory variables.
- Gaussian or normal distribution of the residuals, e.
- A constant variance of the residuals (homoscedastic distribution) with no autocorrelation. In the case of heteroscedasticity, a transformation of the target variable is necessary. The common transformation used is to take the logarithm of the target variable.

2.4.3.2 Logistic Regression

In spite of the name, Logistic Regression (LR) is a classification model. It is a linear statistical model which is efficient for binary classification problems but can be also extended to multi-class classification (called multinomial regression) [138]. In contrast to LnR, LR does not require linearity between the input and the output. It models the probability of an event happening using a logistic function rather than a straight line or hyperplane [139]. Moreover, the output range is limited between 0 and 1. The logistic function has an S-shape as can be seen in the example in **Figure 2.10** and is defined as follow [139]:

$$S(z) = \frac{1}{1 + e^{-z}} \tag{2.13}$$

where z is the input to the function. In order to transform the S(z) probabilities into discrete binary predictions, a threshold value is selected. Typically, the threshold is set at 0.5. For example, the Class is 1 if $S(z) > 0.5$ and 0 otherwise.

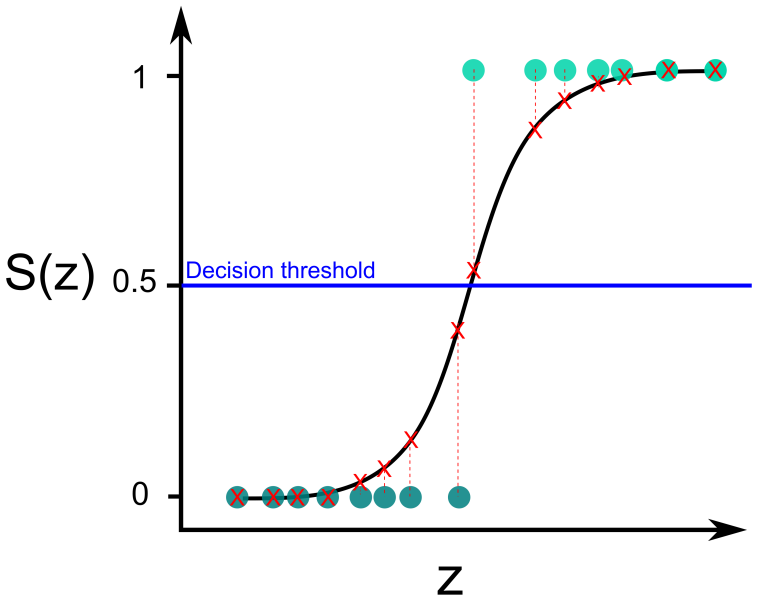

Figure 2.10: Example of logistic regression classification. The black line represents the sigmoid or logistic function given in **Eq.2.13**. The red x's represent the probability of getting class 1. The blue line is the decision boundary based on a threshold of 0.5. The light green dots represent the data classified as 1 and the dark ones classified as 0.

2.4.3.3 Support Vector Machine / Support Vector Regression

Support Vector Machine (SVM) is a kernel-based* supervised learning technique that was originally created for binary classification [117, 140, 141]. It was later generalized to solve multi-class classification and regression problems. SVM works by finding the best hyperplane that separates the different classes in the data with the largest margin, see **Figure 2.11**. The decision function in SVM is specified by a small subset of the data called the support vectors. In a two dimensional space, the hyperplane is a line, see the example in **Figure 2.11**. In this example, the two distinct classes (light and dark green) can be separated by the created hyperplane.

Support Vector Regression (SVR), on the other hand, uses the same principle for finding the best fit for the data. The best fit, in this case, is defined as the hyperplane with the maximum number of points [142, 143].

*Kernel methods essentially allow the use of linear classifiers to non-linear problems. They take the input vector in the original space and transform it into one point in the features space [133].

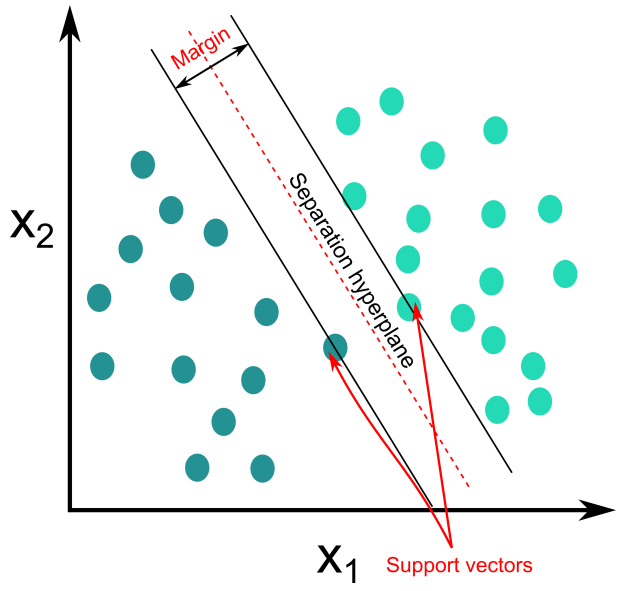

Figure 2.11: Example of Support Vector Machine. The SVM finds the optimal hyperplane while maximizing the margin. The support vectors are the points closest to the decision hyperplane.

2.4.3.4 Decision Trees and Boosting model

Decision trees were first introduced in 1986 [144]. They are among the most widely used supervised learning models. The decision trees represent a recursive splitting of the input space, which can be presented in the graphical form of a tree, see the example in **Figure 2.12**. In this example the input x has two coordinated i.e., features x_1 and x_2, and the output y contain two values (y_1 and y_2) represented by the dark and light green circles. If the values of y are a finite number as presented in this example, the task will be a classification. Otherwise, if $y \in \mathbb{R}$, the problem will be solved as a regression task. The model in both cases tries to learn the hyperplanes that separate the data classes/values, **Figure 2.12 b**. These hyperplanes correspond to each node in the decision tree. The model determines at each node, the feature and split threshold (x_m,t_m) of that feature which maximizes the information gain G, for the model. G is measured based on user-defined splitting criteria. It gives information on how well the defined split is able to separate the data in order for the target values of the data at each node to be homogeneous in the case of classification and close to each other in the case of regression. The mathematical formula of G is given in **Eq.2.14** [145].

$$G(Q,\theta) = \frac{n_{left}}{N_m} H(Q_{left}(\theta) + \frac{n_{right}}{N_m} H(Q_{right}(\theta) \tag{2.14}$$

N_m is the number of samples, H is the chosen split criteria function, Q is the data at node m, and $\theta = (x_m, t_m)$ is the feature and threshold being evaluated.

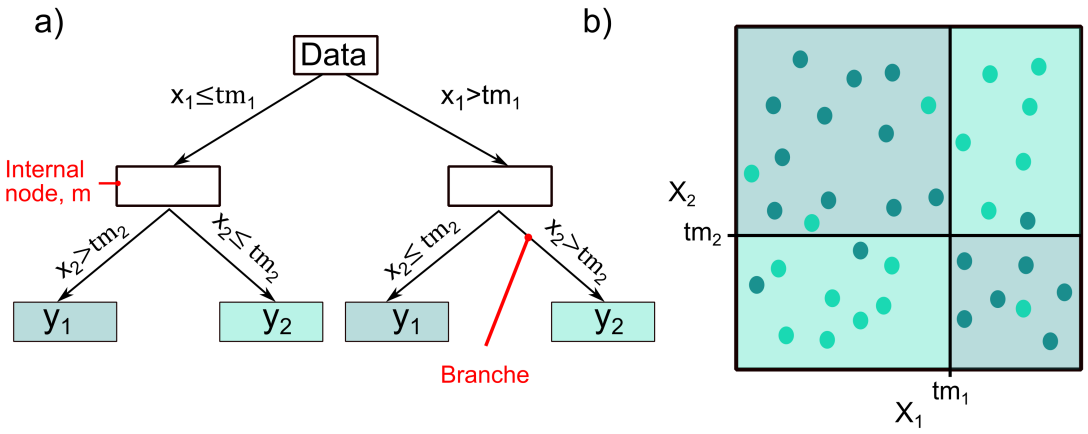

Figure 2.12: Example of a binary decision tree a) Decision tree to separate two groups (dark green :y_1 and light green y_2). The first node asks if x_1 is smaller or larger than a threshold value (val_1). Taking the response into consideration it moves to the second layer and asks if the second input x_2 is smaller or larger than the second threshold (val_2). This continues until reaching a final decision. **b)** Partition of two predictor variables.

Decision trees are intuitive models, easy to explain and use. Moreover, the training data does not require a lot of effort in the prepossessing as they are relatively robust in the presence of noise and outliers [146]. However, they have some disadvantages in comparison to other models. In fact, small changes in the data can lead to a big variation in the structure of the decision tree [146]. They usually require longer time to train the model and the training can be relatively expensive as the complexity of the model increases [117]. In order to overcome these issues, multiple ensemble methods such as random forests, or gradient boosting that consider many trees at the same time were developed.

Gradient boosting: Boosted Tree (BT)

Gradient boosting is an ensemble of weak prediction models. It is typically used with decision trees as a way to reduce variance, bias, and over-fitting. Gradian boosting originated from an observation by Breiman in 1997 [147] but was explicitly developed by Friedman [148, 149].

2.4.3.5 K-Nearest Neighbor

K-Nearest Neighbor (KNN) is an instance-based supervised learning technique. This means that the learning does not create a general model, but stores the data set instances for comparison during the training [150]. Thus, the classification of each new point is determined based on the vote of the nearest neighbors [151]. The vote is done after calculating the euclidean distance as follows:

$$d_{Euclidean} = \sqrt{(x_{1.B} - x_{1.A})^2 + (x_{2.B} - x_{2.A})^2} \tag{2.15}$$

KNN can be used for both classification and regression, problems. The k-neighbor is determined by the user for the number of near neighbors to be considered. It is optimized based on the data. As the value of k increases, the effect of the noise is decreased. However, it reduces the distinction of the boundaries between the different classes.

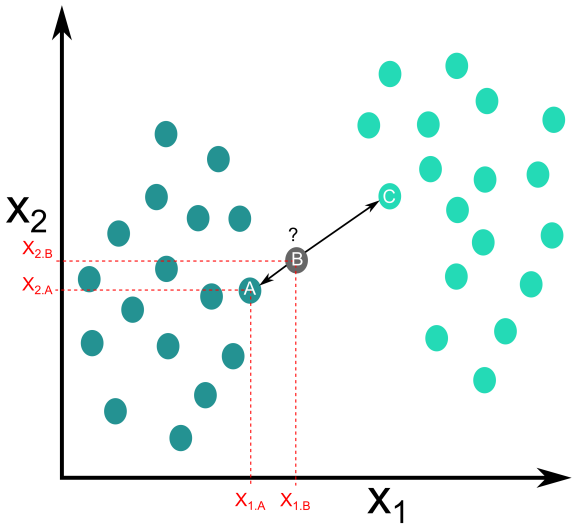

Figure 2.13: Example of KNN classification. When the new data B is brought for classification, the euclidean distance to the nearest neighbors A (dark green class) and C (light green class) is calculated and compared in order to make a decision.

2.5 Scope of this work

As discussed in section **2.1.5**, synthetic fibrillar adhesives may enable the development of new innovative robotic gripping systems. However, for industrial applications where failed gripping could have high costs, anticipating adhesion performance and contact signature could be crucial. The present thesis comprises four chapters with different approaches to monitor the contact and predict the adhesion of the bioinspired structures.

The **Chapters 3** and **4** present two in-line monitoring systems that combine an *in-situ* observation technique, image processing, and machine learning. With the goal to predict the adhesion performance, two solutions were proposed: Supervised regression models were trained to predict the adhesion force of the patterned structures to a stationary target surface. The models were compared to a linear mathematical model and to an existing analytical model, see more details in **Chapter 3**. In order to span the gap between laboratory adhesion experiments and actual manipulation processes, **Chapter 4** presents a classification approach where data was collected in pick-and-place experiments. In this case, various models were trained and compared to predict the successful and unsuccessful grasping of a target object.

The following subsequent of this thesis, **Chapter 5**, introduces two newly developed optical systems. The essential objective for these devices is to improve the effectiveness of patterned adhesives as grippers by monitoring the contact with various types of target surfaces.

Chapter 6 outlines a new approach to predict the contact signature of a soft polymer film in contact with roughness-like surface topography using simulation. The rate and preload-dependency of the adhesion strength were analyzed and the results were compared to experimental data.

Chapter 3

Predicting the adhesion strength of micropatterned surfaces using supervised machine learning*

3.1 Abstract

Fibrillar dry adhesives have shown great potential in many applications thanks to their tunable adhesion, notably for pick-and-place handling of fragile objects. However, controlling and monitoring alignment with the target objects is mandatory to enable reliable handling. In this paper, we present an in-line monitoring system that allows optical analysis of an array of individual fibrils (with a contact radius of 350 µm) in contact with a smooth glass substrate, followed by the prediction of their adhesion performance. Images recorded at maximum compressive preload represent characteristic contact signatures that were used to extract visual features. These features, in turn, were used to create a linear model and to train different linear and non-linear regression models for predicting adhesion force depending on the misalignment angle. Support vector regression and boosted tree models exhibited highest accuracies and outperformed an analytical model reported in literature. Overall, this new approach enables predictions in gripping objects by contact observations in near real-time, which likely improves the reliability of handling operations.

*This chapter is a published article in **Materials Today**.
The article is available under: `https://doi.org/10.1016/j.mattod.2022.01.018`

3.2 Introduction

Over the last decade, the market of automated gripping devices has remarkably grown in the context of ongoing industrial digitalization [152,153]. Such devices are used to grasp and handle delicate objects of diverse geometries and sizes. A new concept for innovative grippers is the implementation of "hairy" or fibrillar dry adhesives inspired from geckos and many insects [8,111,154]. Such adhesives make use of molecular van der Waals interactions enhanced by surface fibrils and function equally well in air and under vacuum conditions [1,62,78,155]. However, their overall performance depends on a multiscale contact engagement that has been subject of multiple studies [1,6,48,156]. Briefly, the adhesion strength on the fibrillar level strongly depends on the fibril size, geometric design and their mechanical properties; these parameters are known to affect the stress distribution in the interface between the fibril tip and the target substrate [17,38,47]. On the array level, the performance depends on the load sharing efficiency and statistical variations throughout the array [53,55,63,64]. Under non-ideal conditions, arrays can exhibit adhesion strengths that are significantly reduced when compared to the sum of all individual fibrils [48].

Despite numerous successful demonstrations of the benefits of fibrillar adhesives in comparison to non-patterned adhesives and other gripping technologies, their reliability in a specific gripping situation needs to be ensured. Van der Waals interactions have short range and act appreciably only over a few nanometers. Loss of intimate contact, caused by interfacial defects due to surface roughness or contaminants or by insufficient alignment, can drastically reduce adhesion [54,56]. The effect of misalignment on the pull-off force was previously reported by Bacca *et al.* [53,55] and Booth *et al.* [54]. They theoretically demonstrated that several design parameters such as array size, fibril length, spacing between fibrils, and compliance of the backing layer affect the sensitivity of adhesion to alignment errors [53–55]. These results were experimentally validated and proved that even a small misalignment, of order of 0.1°, will initiate detachment by peeling and, thus, drastically decrease the adhesive force [54].

To predict the pull-off force, F_p, in terms of the misalignment angle, θ, Booth *et al.* evolved an analytical model as follows:

$$F_p = \begin{cases} N\, f_{max}[1 - \frac{\pi\, a^2\, E}{2\, f_{max}}(n-1)\, \tan\theta\, \frac{d}{h}, & \tan\theta \leqslant \frac{f_{max}}{\pi\, a^2\, E}\, \frac{h}{d\,(n-1)} \\ \frac{N\, f_{max}}{2\, n}[1 + \frac{f_{max}}{\pi\, a^2\, E}\frac{1}{\tan\theta}\frac{h}{d}], & \tan\theta > \frac{f_{max}}{\pi\, a^2\, E}\frac{h}{d(n-1)} \end{cases} \tag{3.1}$$

where $N = n^2$ is the total number of fibrils in a square array, f_{max} the pull-off force of an individual fibril, the elastic modulus E and a the radius of the

fibril, h the length of the fibril, and d the center-to-center spacing. However, the model is only valid in the limits of a rigid backing layer and complete contact of all fibrils with the target surface, where all fibrils detach at the same maximum force (f_{max} = const.). These conditions can barely be met in real applications, since, for example, the fibril array is typically connected to an elastic foundation instead of a rigid backing layer [54]. Depending on the size of the array and the angle of misalignment, bringing all fibrils in contact with the object can be difficult.

Moreover, recent *in-situ* observation techniques have enabled the determination of the adhesion strength of individual fibrils; the experiments showed that the strength can vary by more than an order of magnitude between the weakest and strongest fibril, contradicting the tacit assumption of a constant pull-off force [62]. In fact, the adhesion performance of an individual microscopic fibril is mainly governed by critical interfacial defects, originating from surface roughness, fabrication imperfections, contaminations or dust particles [51]. Defect sizes and their locations can randomly vary in the adhesive contact, leading to a pull-off force distribution across the array [60]. Recently, Booth *et al.* proposed a statistical framework based on Weibull statistics to predict adhesion forces by considering the Weibull modulus, m characterizing the width of the force distribution, and the reference elongation at detachment, u_0 [63]. Both parameters can be determined experimentally, but remain specific to each adhesive contact of a specimen adhering to a target surface [64, 157]. Overall, calculating the performance of fibrillar adhesives is a multiscale contact mechanics problem that, for a specific case, can potentially be solved by numerical methods. However, such an approach would be too slow for an in-line monitoring of a dynamic pick-and-place handling operation and, thus, cannot be implemented in robotics applications.

Toward this goal, the training of machine learning systems provides an alternative approach as a powerful tool for near real-time decision making. In the present paper, we make use of the *in-situ* observation of fibrillar adhesive contacts, providing characteristic contact signatures which delineate attached and detached regions that can be readily recorded and analyzed in-line. Based on these contact signatures we identified visual features that were used to train regression models to predict the pull-off force in terms of the misalignment angle. The models were compared to a feature-based linear model and to the analytical model in **Eq.3.1**.

3.3 Materials and methods

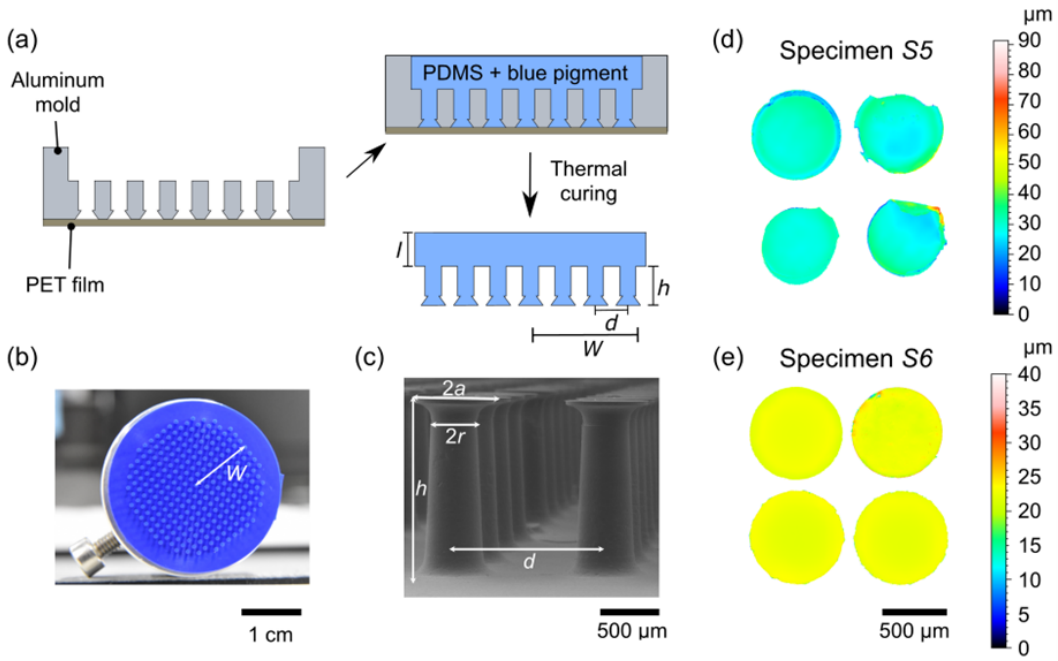

Figure 3.1: Design and fabrication of the microfibrillar adhesives. a) Schematic of the fabrication process using replica molding. PDMS was mixed with blue pigment, filled into an aluminum mold, and subsequently cured. **b)** Optical image of a micropatterned adhesive specimen that typically consisted of 241 fibrils. **c)** Scanning electron micrograph showing the mushroom-shaped fibrils with a typical fibril length $h = 160\,\mu m$, stalk radius $r = 200\,\mu m$, and mushroom tip radius $a = 350\,\mu m$. The center-to-center distance between adjacent fibrils is $d = 1350\,\mu m$. Half the width of the array is $W = 11\,mm$. **d,e)** Confocal microscope images showing the range from defected (S5) to almost perfect (S6) tip topography.

Ten micropatterned specimens (S1-S10) were fabricated from polydimethylsiloxane (PDMS, Sylgard 184, Dow, Midland, MI, USA) using replica molding as illustrated in **Figure 3.1 a** and thoroughly described in previous reports [62,157]. The transparent PDMS was mixed in a ratio 10 : 1 of base and curing agent. To enhance the optical contrast for the in situ observation, 10 wt% blue pigment (PK 5091, Degussa, Essen Germany) was added to the pre-polymer mixture, which was subsequently either cured at 95 °C for 1 h [157] or 75 °C for 2 h [62]. The dimensions of the micropatterned specimens are summarized in **Table A1** in the Supporting Information (SI). Note that five specimens were previously employed in recent studies: Specimens S4 and S5 were used to study local detachment mechanisms and suction effects [62]; specimens S6 and S7 were used to investigate the contact aging [157]; and specimens S4-S8 were used for a statistical analysis of the detachment instabilities [64]. Specimens S1, S2, S3, S9, and S10

were made for the present study as described above. The thickness of the backing layer was 3 mm for S1-3 and 5 mm for S4-10.

3.3.1 Adhesion measurement

Pull-off forces of the micropatterned adhesives were measured using a custom-built tensile tester (Inspekt table BLUE, Hegewald&Peschke, Nossen, Germany) equipped with a 50 N load cell with a stiffness of $k_{50} = 134.6\,\mathrm{Nmm}^{-1}$. For adhesion tests, the micropatterned specimens were brought in contact with the target object, a smooth and transparent glass disc at a velocity of 1 mm/min. Upon first contact with the substrate, the specimen was compressed by 105 µm , then immediately retracted at a rate of 1 mm/min. The highest tensile force obtained was defined as pull-off force, F_p. The stiffness, k of the fibrillar specimens was determined from force-displacement curves in the compressive regime. To remove dust and contaminants, the glass substrate was cleaned with isopropanol after each test, i.e., every 55 cycles.

The alignment between the specimens and the substrate was varied between 0 and 1° in steps of 0.1°. The orientation of the adhesive array to the fixed misalignment direction was further analyzed by repeating the measurements 4 times, where the specimen was rotated by 45° before each test. In addition to misalignment, we enhanced the variations of the tests by emulating off-center gripping. For this purpose, a device with an aluminum beam was added between the specimen and the load cell (**Figure 3.2 b**). The beam was 10 cm long, 3 mm thick, and 10 mm wide, resulting in a stiffness of $6.73\,\mathrm{Nmm}^{-1}$. The device introduced a torque, which led to a peeling moment, M, at the contact. The peeling moment superimposed onto the chosen misalignment angle. Therefore, two cases were considered: (i) The peeling moment acted in the same direction as the misalignment, referred to as $+M$; or (ii) was opposite to it, referred to as $-M$.

Experiments to determine the Weibull moduli, m, and the reference displacements, u_0, were conducted using a 200 N load cell with $k_{200} = 935\,\mathrm{Nmm}^{-1}$ to ensure stable detachment [64]. All experiments were performed in a laboratory with regulated temperature and relative humidity at 21 ± 0.2 °C and 50 ± 5 % .

3.3.2 Contact observation and image analysis for features extraction

In order to investigate the contact between the adhesive and the counter surface, the principle of frustrated total internal reflection was used as illustrated in **Figure 3.2 a**. The internally reflected light in the transparent glass substrate

scattered when a contact with the adhesive's fibrils was formed. Thus, a high contrast between the fibrils in contact and the detached ones can be obtained [62,157]. Images of the contact at preload, i.e., the contact signatures, were extracted from the recorded videos and analyzed using Computer Vision and Image Processing toolboxes from MATLAB (MathWorks, MA, USA). To convert from pixel to micrometer scale, the mean distance between fibril centroids, $d = 1350\,\mu m$, was used. The images were binarized by selecting a threshold gray value. Then, pixels with gray values higher than the threshold were considered white and represented contact (attachment) while pixels with lower gray values were considered black and represented non-contact (detachment). The binarization is motived by its high reproducibility when being transferred to another setup or the usage of other specimens. Considering only a single image at max. compressive preload further reduces the complexity of multiple frame analyses and potential delays during inline processing in robotic applications. From binarized images (**Figure 3.2 d,e**), the number of attached fibrils, N_a, the contact area, A, which is the sum of the real contact areas of the individual fibrils (either at full or partial contact), and the center position (x and y-coordinates) of each fibril were determined. From the latter, the length of the misalignment vector, $\vec{v}$ was calculated, which is the distance between the center of mass of a reference full contact and the center of mass of the specimen in partial contact (**Figure 3.2 f**). The length of the misalignment vector can range from 0 (full contact) to 11 mm (i.e., the half-width of the array, W, see **Figure 3.1 b**). Finally, the dimensionless number of fibrils in contact with the substrate, N_a, the length $W - |\vec{v}|$, and the real contact area, A were used as visual features for training the machine learning algorithms (see details below). Note that the pixel size of the contact signatures was about 50 µm, which is most likely too large to detect location and sizes of potentially critical interfacial defects. Therefore, we limited our investigations to rather macroscopic features.

For determining the statistical parameters of the Weibull distribution, m and u_0, of each specimen, the detachment videos were correlated with the force-displacement measurements [48]. For synchronization, the frame showing the detachment of the last fibril was attributed to the time when the tensile force dropped to zero. The fraction of the detached fibrils in terms of the fibril elongation, u was then obtained and fitted by **Eq.3.2** which represent the cumulative Weibull distribution (see **Figure 3.2 c**):

$$\frac{N_d}{N} = 1 - \exp\left\{\left(-\left[\frac{u}{u_0}\right]^m\right)\right\}, \tag{3.2}$$

with N_d the number of the detached fibrils and N the total number of pillars in

an array.

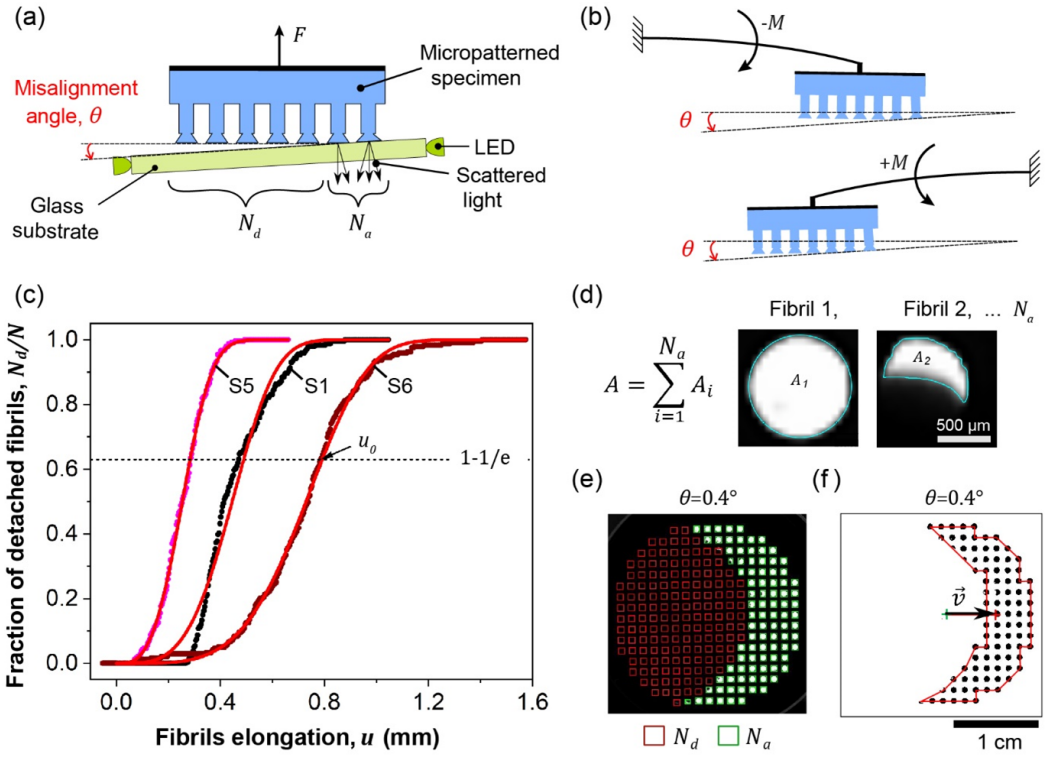

Figure 3.2: Adhesion testing and visual features. a) Schematic illustration of the adhesion measurement set-up. Frustrated total internal reflection was used to enhance the contrast between N_a attached and N_d detached fibrils. Force, F was applied normally to the adhesive array. The angle of misalignment, θ was introduced by tilting the substrate. **b)** Off-center loading was emulated in two directions (left and right) in separate measurements using an aluminum beam leading to a peeling moment -M or $+M$, for the left and right directions, respectively. **c)** Fraction of detached fibrils versus the elongation of the fibrils, u for specimens S1, S5 and S6. The red line is the fitted Weibull distribution given by **Eq.3.2**. The reference elongation, u_0 is attributed to $N_d/N = 1 - 1/e$ (dashed line). d-f) Visual features extracted from contact signatures at maximum compression: **d)** Full (left) or partial (right) contact of individual fibrils, where the sum of all fibrils provides the contact area. **e)** The number of attached (number of green boxes) and detached (number of red boxes) fibrils. **f)** The length of the misalignment vector (black arrow), corresponding to the distance between the center of mass of the complete contact ($\theta = 0°$) and the center of mass of a partial contact ($\theta = 0.4°$). Here, the black dots and the red contour represent the centroids of the attached fibrils and the area for the calculation of the center of mass, respectively.

3.3.3 Machine learning

For creating predictive models, supervised learning algorithms were used by the Statistics and Machine Learning toolbox from MATLAB (ver. R2019b). The Regression Learner toolbox was used to train various regression models: Linear Regression (LnR), Support Vector Regression (SVR), and Boosted tree (BT). The LnR was chosen as a simple linear model, whereas SVR and BT were the result of a pre-evaluation with the highest accuracy upon validation. Fully connected neural networks were considered as an alternative but discarded as the amount of training data was insufficient for an effective training. Avoiding the manually defined features altogether and using convolutional neural networks on a pixelates representation of the fibrils might seem an obvious alternative, but the total number of fibrils would result in an input resolution below the receptive field size of any reasonable network. The hyperparameters of the SVR and BT were optimized directly through the Regression Learner toolbox. The experimental data of 10 specimens was divided into training, validation and testing data on the specimen level with ratio 6:2:2, respectively. Specimens S1 to S8 were used for training and validation. To avoid overfitting during training, a four-fold cross-validation, again at the specimen level, was performed. Therefore, 6 specimens of S1 to S8 were randomly picked and validated by the remaining 2 specimens. Trained models were tested using 2 new specimens S9 and S10, which were fabricated once all models were trained and validated.

Before training, the extracted features A, N_a, and $W - |\vec{v}|$ were normalized by min-max scaling such as $A' = (A - \min(A))/(\max(A) - \min(A))$ by using the training data. Normalization parameters obtained were then used to normalize the testing data.

To evaluate the models, three metrics were calculated as follows: the R-squared, $R^2 = 1 - \frac{\sum_i (y_i - \hat{y}_i)^2}{\sum_i (y_i - \bar{y}_i)^2}$, the root mean square error, $RMSE = \sqrt{\frac{\sum_{i=1}^{n} (\hat{y}_i - y_i)^2}{n}}$, and the mean absolute error, $MAE = \frac{\sum_{i=1}^{n} |\hat{y}_i - y_i|}{n}$, where y_i is the value of the i-th observation in the validation data, $\hat{y}_i$ the predicted value, $\bar{y}_i$ the mean of the observed data, and n the number of observations. Note that for the LnR model, the features A, N_a, and $W - |\vec{v}|$ were transformed logarithmically before normalization to maintain a homoscedastic distribution of the data with similar variances (**Figure A1** in the Supporting Information (SI)) as a prerequisite for the linear regression approach.

3.4 Results and discussion

3.4.1 Variations of the specimens

Micropatterned adhesives with mushroom-shaped fibrils were successfully fabricated from PDMS using replica molding (**Figure 3.1**). The tips of the fibrils were replicated from different PET films that were used to close the bottom of the mold (**Figure 3.1 a**). The film topography was then transferred to the fibril tips, which in turn, caused a distribution of the fibril adhesion strength across the array, as described in earlier reports [62–64, 157]; see **Figure 3.1 d,e**. The fibril dimensions, as determined by optical microscopy, are summarized in **Table A1** in the SI. To quantify these strength distributions, the maximum elongation, u of each fibril was determined from *in-situ* observations of the fibril detachment events. Following Weibull statistics, the ratio of the N_d to the total number of fibrils, N is assumed to be given by **Eq.3.2**. **Figure 3.2 c** displays exemplarily the fit of **Eq.3.2** to the experimental data for three specimens S1, S5, and S6. The characteristic statistical values m and u_0 for each specimen are summarized in **Table 3.1**. Considering the stiffness of the specimens, k (obtained from load-displacement curves), the reference force, $f_0 = ku_0/N$ could be estimated by ignoring the backing layer deformation. Weibull moduli ranged from 2.0 to 13.9, u_0 from 0.28 to 0.79 mm, k from 38.4 to 56.8 kN/m, and f_0 from 47.8 to 141.5 mN, which all together represent statistical variations of the specimens used in the present work.

Table 3.1: Variations of the specimens in terms of Weibull moduli, m, reference elongation, u_0, stiffness of the specimen, k, and the reference force, f_0.

specimen	m	u_0 (mm)	k (kN/m)	f_0 (mN)
S1	3.8	0.49	42.5	86.4
S2	6.5	0.40	39.1	64.9
S3	9.0	0.38	38.4	60.5
S4	5.1	0.38	56.8	91.5
S5	3.3	0.28	40.5	47.8
S6	4.4	0.79	42.8	141.5
S7	2.0	0.32	44.6	59.2
S8	3.6	0.29	45.3	54.5
S9	13.1	0.28	50.2	58.3
S0	13.9	0.32	47.4	63.5

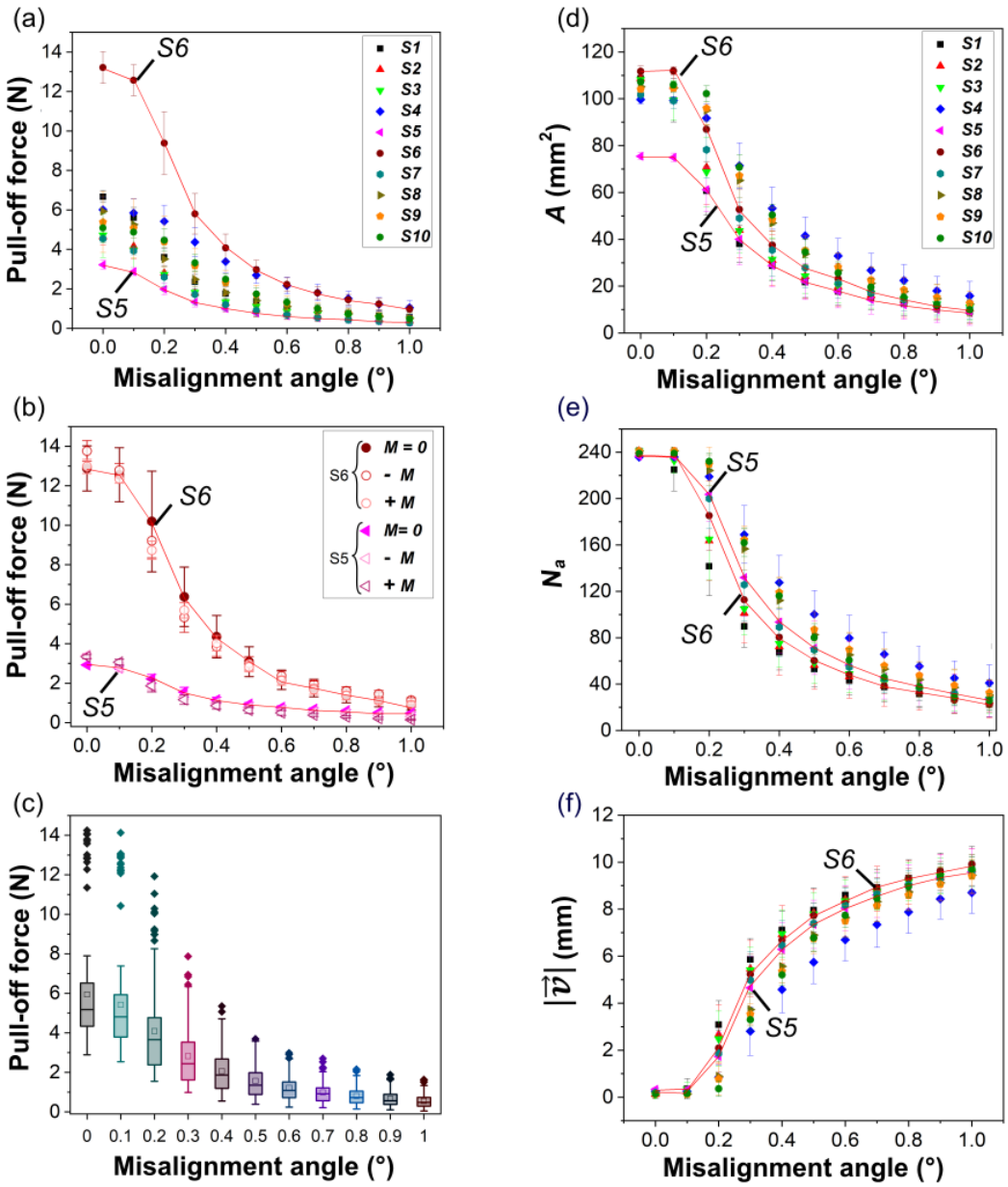

Figure 3.3: Adhesion results. **a)** Pull-off force versus misalignment angle for all specimens including variations of the specimen rotation and the peeling moment induced by the beam. Symbols represent the mean value of 15 measurements and the bars the standard deviation. The lines highlight the weakest and strongest specimens. **b)** Pull-off force variations as a function of the induced peeling moment $+M$ and $-M$ for two specimens S5 and S6. **c)** Box plot showing the one-way ANOVA analysis of the pull-off force in terms of misalignment angles. The top and bottom of each box are the 25th and 75th percentiles, respectively. The line in each box is the median and the square represents the mean value. Lines extending above and below each box represent 1.5 times the interquartile range. The solid diamonds correspond to outliers according to this analysis. **d-f)** Features in terms of the misalignment angle of all tests conducted: **d)** Contact area, A **e)** number of attached fibrils, N_a and **f)** the length of the misalignment vector, $\vec{v}$. All features were extracted from contact signatures at max. preload. The lines highlight the weakest and strongest specimens S5 and S6.

3.4.2 Adhesion analysis results

Adhesion tests comprised 1635 measurements in total, where the misalignment angle, the orientation of the specimen to the misalignment axis, and the peeling moment induced by a lever were varied. **Figure 3.3 a** depicts the pull-off force versus misalignment angle of all measurements conducted, exhibiting a large variation of the pull-off force over different specimens. For the aligned case ($\theta = 0°$), the adhesion force ranged from $3.2 \pm 0.23\,\mathrm{N}$ for the weakest specimen (S5) to $13.2 \pm 0.8\,\mathrm{N}$ for the strongest specimen (S6, see solid lines to guide the eye). As a general trend, the pull-off force decreased with increasing misalignment angle and forces dropped below 1 N for all specimens at $\theta = 1°$.

Figure 3.3 b depicts the effect of the peeling moment on the results for the strongest (S6) and the weakest (S5) specimen. For S6, the peeling moment led to a reduction of the pull-off force by 10 to 20 % between 0.2 and 0.5° of misalignment, whereas the impact of the peeling moment decreased considerably as the misalignment angle was larger than 0.5°. The pull-off force of specimen S5 decreased by 15–35% over the entire range of θ. For both specimens, the direction of the beam compared to the misalignment direction (see **Figure 3.2 b**) made no significant difference to the pull-off forces. Overall, the introduction of the peeling moment increased the variation of the resulting pull-off force; however, the direction of the applied peeling moment did not significantly affect the results.

Figure 3.3 c presents the results of the one-way analysis of variance (ANOVA, OriginLab, Northampton, MA, USA) including all experimental data. Mean and median values decreased with increasing misalignment. Similarly, the box size (i.e., the interquartile range from 25 to 75 %) decreased. Thus, also the variation of the pull-off force decreased as misalignment increased. Note that multiple data points belonging to specimen S6 were considered as outliers (diamonds) as they are outside the interquartile range, multiplied by 1.5, due to their comparably high pull-off forces.

The contact area, A, represents one of the three visual features obtained from the *in-situ* observations at maximum compressive preload. **Figure 3.3 d** displays the contact area versus the angle of misalignment. The contact area varied at $\theta = 0°$ for the various specimens with a minimum of $75.5 \pm 1.5\,\mathrm{mm}^2$ (S5) and maximum of $111.7 \pm 0.2\,\mathrm{mm}^2$ (S6). This variation is caused by slightly different sizes of the mushroom tips, interfacial defects and missing fibrils, see **Figure 3.1 d,e** and **Table A1** in the SI. At the smallest misalignment $\theta = 0.1°$, full contact upon preloading was still achieved but a small drop of the pull-off force can be observed for the different specimens. This can possibly be explained by the unequal load-sharing between the different pillars resulting from a small

misalignment [53]. For $\theta \geq 0.2^{\circ}$, the contact area dropped considerably for all specimens. Here, only partial contact was achieved at the fixed compressive displacement of 105 µm upon first contact. Despite the fact that the contact area for S6 fell more drastically with increasing θ than for the other specimens, the specimen with the highest adhesive force was still stronger, as the reference pull-off force, f_0 was the highest for S6 (**Table 3.1**). In **Figure 3.3 e,f**, the number of attached fibrils, N_a and the length of the misalignment vector, $\vec{v}$ are shown in terms of the misalignment angle. For $\theta = 0.1^{\circ}$, both values were similar to the aligned case for most specimens due to full contact. For $\theta \geq 0.2^{\circ}$, N_a decreased monotonically, whereas $\vec{v}$ increased up to 10 mm.

Figure 3.4 presents the variation of the pull-off force in terms of the three different visual features for the training data, i.e. specimens S1 to S8. As expected, the pull-off force increased linearly with a larger contact area, a higher number of attached fibrils, and a larger value of $W - |\vec{v}|$. Despite the approximately linear relationships, significant variation was observed when comparing the different specimens; the solid lines linking the lowest (S5) and highest (S6) values were drawn to guide the eye. Linear fits for these limiting cases result in similar slopes of 3.64 ± 0.06 and 12.24 ± 1.2 N (see **Figure 3.4 a**), 2.25 ± 0.05 and 12.52 ± 0.2 N (see **Figure 3.4 b**), and 2.3 ± 0.01 and 12.3 ± 0.5 N (see **Figure 3.4 c**). From the linear trends observed in **Figure 3.4** , we created a linear model to predict the pull-off force, F_p based on the normalized visual features, as follows

$$F_p = \bar{C} \cdot A' N_a' \left(W - |\vec{v}|\right)', \tag{3.3}$$

where A', N_a', and $(W - |\vec{v}|)'$ are normalized contact area, number of fibrils in contact, and length of the misalignment vector. The constant $\bar{C} = 5.56$ N is the mean slope of all linear fits for each specimen. **Figure 3.5 a,b** show the calculated pull-off force using the mathematical model, **Eq.3.3**, versus the testing data, i.e. specimens S9 and S10. For both specimens, the model was able to predict accurately pull-off forces for small misalignments of $\theta \leq 0.2^{\circ}$. However, larger misalignment angles led to underestimated forces up to 78 % for some cases. To overcome this limitation, we trained several regression models.

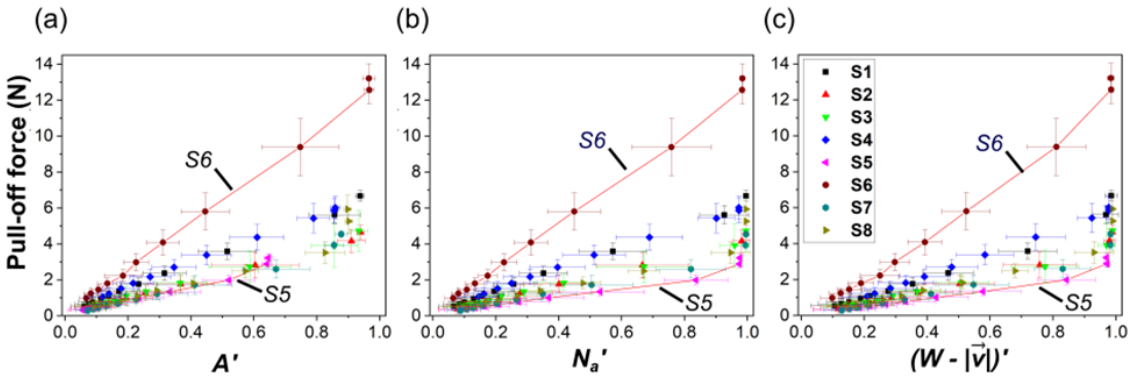

Figure 3.4: Pull-off force versus visual features for the training data. **a)** the normalized contact area, A'; **b)** the normalized number of fibrils in contact, N_a'; and **c)** the normalized length of the misalignment vector, $(W - |\vec{v}|)'$.

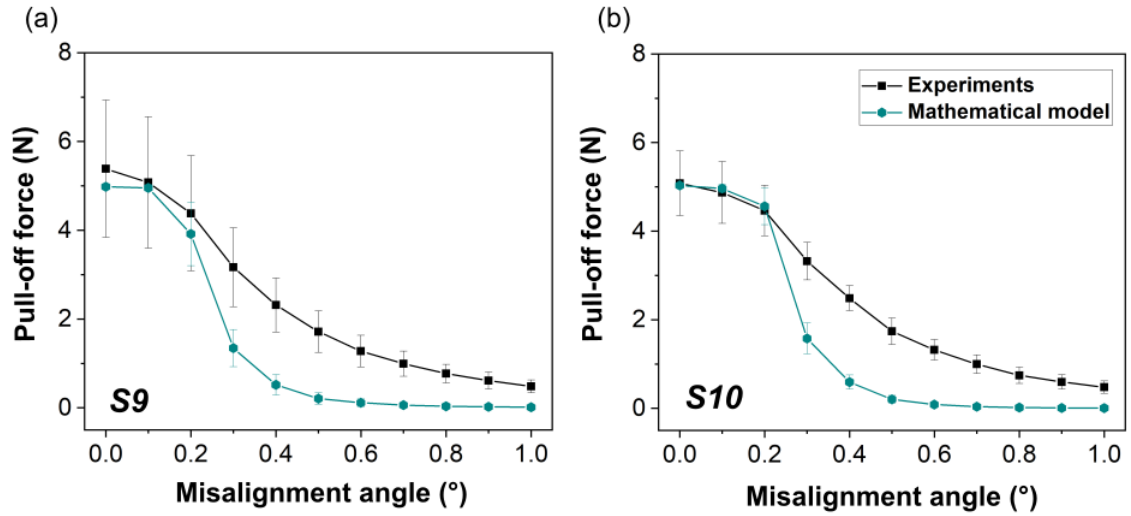

Figure 3.5: Calculated pull-off forces using the mathematical linear model Eq.3.3 (green hexagons) in comparison to the test specimens **a)** S9 and **b)** S10 (black squares).

3.4.3 Supervised machine learning

A linear regression model (LnR) and two non-linear models, the support vector regression (SVR) and the boosted tree (BT) were used. To avoid misspecification of the LnR model (which assumes homogeneous variance of the residuals), the data were logarithmically transformed before normalization, see **Figure A1** in the SI. **Figure 3.6** depicts the predicted versus the experimental pull-off forces for all models. The LnR model drastically underestimated the pull-off forces, i.e. similar trends obtained for the linear mathematical model. The SVR and BT model showed better predictions, since predicted pull-off forces scatter closely to the red line, corresponding to perfect prediction. The highest accuracy was

obtained for the SVR with the highest $R^2 = 0.84$ and lowest root mean square error, $RMSE = 0.72$ and mean absolute error, $MAE = 0.46$.

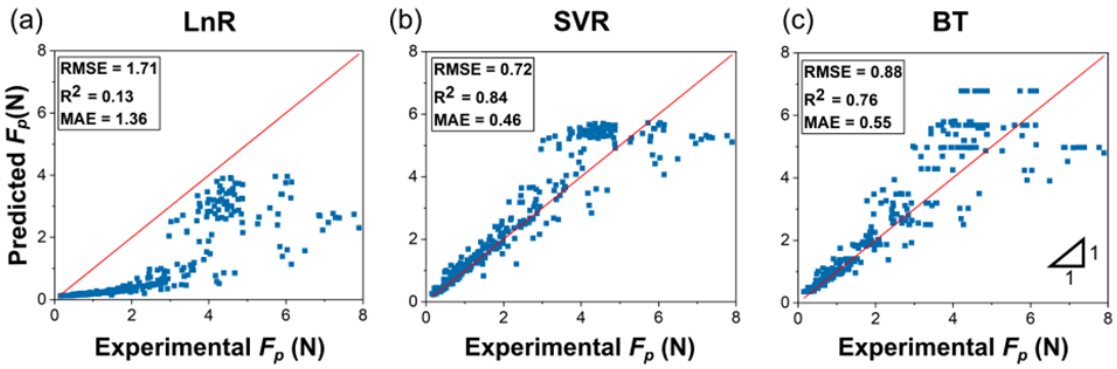

Figure 3.6: Regression results. Predicted versus experimental pull-off forces F_p, of the testing data (blue squares) for **a)** linear regression (LnR), **b)** support vector regression (SVR), and **c)** boosted tree (BT) models. Measures of accuracy are R^2, the root mean square error $RMSE$, and the mean absolute error MAE. The red solid lines represent perfect prediction.

Finally, the trained regression models were tested and compared to the limiting case (stiff backing layer and full contact of all fibrils with the target surface) using the analytical mechanical model (**Eq.3.1**) and the mathematical model based on the visual features (**Eq.3.3**). **Figure 3.7** displays the pull-off force versus the angle of misalignment for the test specimens S9 and S10. For $\theta = 0°$, the experimental pull-off force was used to calibrate the analytical model adjusting $f_{max} = F_p/N_a$ (see **Eq.3.1**). However, the analytical model (red solid line) strongly underestimated the pull-off forces for $0.1° \leq \theta \leq 0.8°$, even though the model assumes full contact between the fibrillar array and the target surface.Note that the analytical model assumes a rigid backing layer and full contact for all θ. Thus, the model ignores the benefit of the compliant backing layer and only represents a limiting case [54]. The mathematical model agrees with the experiments for small misalignment angles ($\theta \leq 0.2°$), but underestimates pull-off forces for larger misalignment degrees. This discrepancy has been overcome by the SVR and BT model, which both provided accurate fits to the experiments by replicating the entire S-shape of the curves. The LnR model drastically underestimated the pull-off forces, similarly to the linear mathematical model. **Table 3.2** summarizes the fitting parameters of all models for the two test specimens which again highlights the good agreement of the SVR and BT model.

Overall, predicting the force using the analytical model is limited to the prior knowledge of the misalignment angle, the specimen's maximum adhesion force, and ignoring the backing layer compliance. Therefore, the analytical model only serves as a limiting case. In contrast, the machine learning approach provides

a more suited way to predict unwanted detachment failures and, in combination with an in-line image analysis, to monitor pick-and-place devices. Since we have focused on selecting features from binarized frames acquired at compressed preload, the in-line processing should be fast and realistic to be applied to real robotic systems. However, there exists other factors that could still limit their integration. Force-controlled object handling by robotic grippers could alter the adhesion performance and detachment compared to a displacement-controlled setup used in the present experiments [64]. Furthermore, other parameters such as velocity and acceleration of the gripper or larger peeling moments due to object rotations possibly reduce the predictive power of the machine learning algorithms. Finally, the techniques as presented is applicable only to transparent or translucent objects. However, further improvements and model optimization are possible and will allow to significantly enhance the reliability of the predictions in realistic pick-and-place processes.

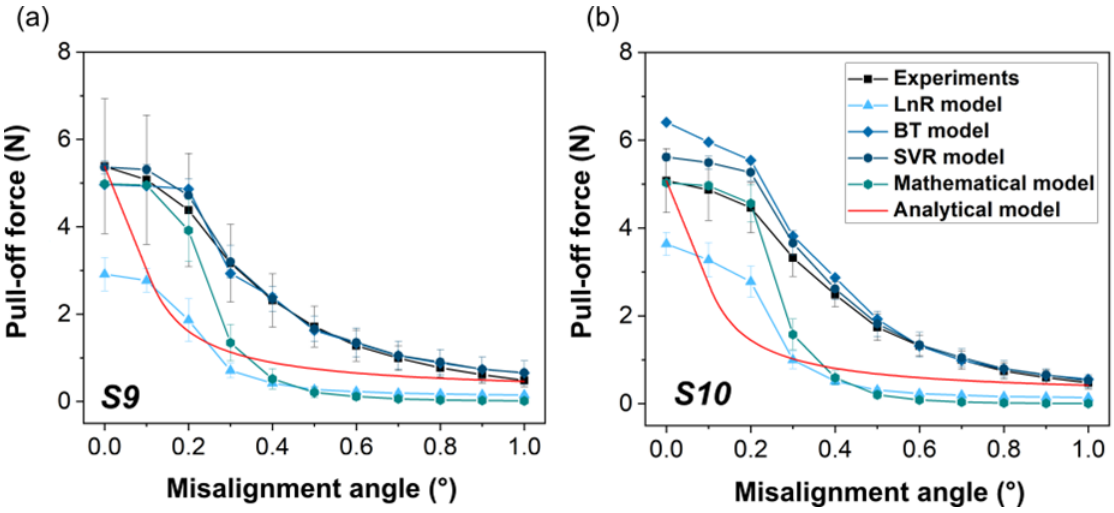

Figure 3.7: Model testing. Pull-off forces versus misalignment angle comparing experiments of specimens **a)** S9 and **b)** S10 (black squares) with the LnR, BT, and SVR regression models, the analytical model (red line) given by **Eq.3.1**, and the mathematical model (green hexagons) given by **Eq.3.3**.

Table 3.2: Accuracies obtained from fitting the experimental results obtained from specimens S9 and S10 using the different models as shown in **Figure 3.7**.

specimen	model	R^2	$RMSE$	MAE
S9	SVR model	0.80	0.87	0.59
	BT model	0.76	0.93	0.6
	LnR model	-0.006	1.94	1.48
	Analytical model	0.34	1.56	1.11
	Mathematical model	0.5	1.37	1.18
S10	SVR model	0.90	0.53	0.33
	BT model	0.77	0.83	0.51
	LnR model	0.29	1.46	1.24
	Analytical model	0.23	1.52	1.15
	Mathematical model	0.56	1.14	1.00

3.5 Conclusions

We explored supervised learning algorithms for predicting the adhesion performance of micropatterned dry adhesives by optical observation. The variation of the pull-off forces was determined as a function of the misalignment angle between specimens and the nominally flat glass substrate, the statistical distribution of the adhesion force of the individual fibrils, and center and simulated off-center gripping. Predictions rely on the contact signatures, i.e. the visual features extracted from optical images, that were taken from the contact at preload. Frustrated total internal reflection in the transparent substrates was utilized to enhance the contrast. Adhesion prediction was approached by regression models and the following conclusions can be drawn:

- Feasibility demonstration: Supervised learning algorithms and *in-situ* observation techniques have been demonstrated to successfully predict the adhesion performance with high accuracy. In fact, this new approach not only overcomes the limited accuracy of a linear mathematical model and an existing analytical model but also time-consuming numerical simulations and facilitates near real-time predictions during the handling process.

- From the regression algorithms tested, the SVR model has the most predictive power with the highest R^2 and lowest root mean square and mean absolute errors. Comparison with experiments confirmed this result and showed higher accuracy than the mathematical and analytical model.

Supporting information: chapter 3

Table A1: Dimensions of the micropatterned specimens. Data represent mean values and standard deviations of 10 randomly selected fibrils.

specimen	Stalk radius, r (µm)	Tip radius,a (µm)	Fibril length, h (µm)	Total Number of fibrils, N
S1	203.31 ± 2.98	360.040 ± 2.05	1550.11 ± 10.34	241
S2	205.48 ± 1.46	353.941 ± 2.31	1563.19 ± 15.42	241
S3	206.26 ± 2.23	360.126 ± 11.52	1587.43 ± 13.11	241
S4	204.26 ± 4.19	350.672 ± 11.75	1580.16 ± 11.53	236
S5	202.83 ± 2.45	319.775 ± 34.88	1516.85 ± 18.17	237
S6	208.98 ± 0.96	364.778 ± 2.70	1578.31 ± 8.13	239
S7	205.03 ± 2.90	353.461 ± 3.79	1577.56 ± 11.44	241
S8	209.71 ± 1.35	350.270 ± 7.87	1559.15 ± 10.64	241
S9	208.22 ± 1.58	353.559 ± 1.77	1556.37 ± 9.10	241
S10	207.56 ± 0.80	352.287 ± 1.64	1563.17 ± 3.47	239

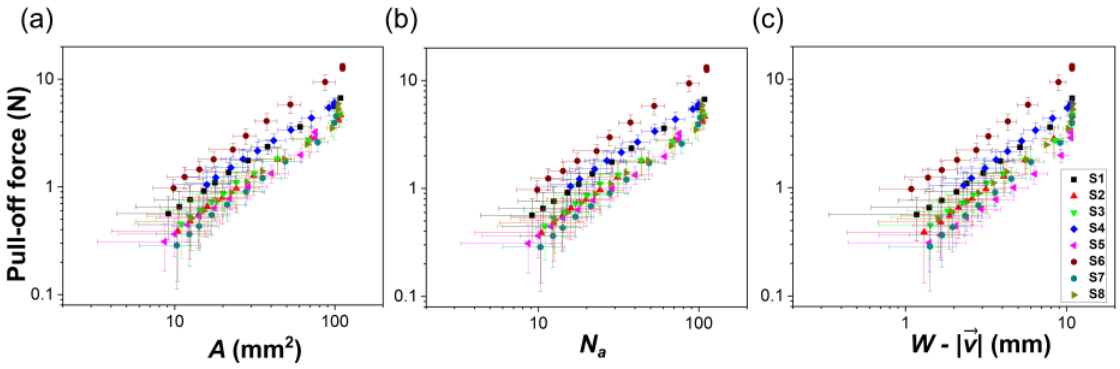

Figure A1: Logarithmic transformation of data presented in 3.4 for training the linear regression model. Pull-off force, F_p versus **a)** contact area, A; **b)** number of fibrils in contact, N_a; and **c)** the difference of half of the width of the array and the length of the misalignment vector, $W - |\vec{v}|$.

Chapter 4

Application of machine learning to object manipulation with bioinspired microstructures

4.1 Abstract

Bioinspired fibrillar adhesives have been proposed for novel gripping systems with enhanced scalability and resource efficiency. Here, we propose an *in-situ* optical monitoring system of the contact signatures, coupled with image processing and machine learning. Visual features were extracted from the contact signature images recorded at maximum compressive preload and after lifting a glass object. The algorithm was trained to cope with several degrees of misalignment and with unbalanced weight distributions by off-center gripping. The system allowed an assessment of the picking process for objects of various masses (200, 300, and 400 g). Several classifiers showed a high accuracy of about 90 % for successful prediction of attachment, depending on the mass of the object. The results promise improved reliability of handling objects, even in difficult situations.

4.2 Introduction

We are right on the edge of the fourth industrial revolution. As industries are transitioning towards automation and digitalization of their production lines, the need for smart grippers has grown rapidly. The goal for this transformation is to increase efficiency, speed, and quality of objects manipulation [158, 159]. For nearly half a century, robotic grippers have relied on various technologies, such as suction and vacuum, electrostatic and magnetic attraction, and, most widespread, mechanical gripping [152]. Since the development of gecko-inspired fibrillar polymer surfaces [5, 8, 14, 21, 160–165], a new gripping principle is now in the process of entering the market [71, 74, 166–170]: manipulation of objects by microfibrillar elastomer surfaces, whose adhesion can be switched on and off. Such surfaces achieve, after application of small compressive preloads, strong adhesion by van der Waals interaction and allow residue-free and silent handling, effective in both air and vacuum conditions [9,78,155]. These properties promise significant benefits over conventional gripping technologies, especially in manipulation of delicate and fragile objects of diverse sizes and geometries.

Object manipulation has to also work under non-ideal conditions. It has to tolerate loss of the intimate contact with the target object due to interfacial defects or due to inevitable alignment inaccuracies [53, 54, 56]. As opposed to previous assumptions, it has been proven by Tinnemann *et al.* [62] that the different fibrils behave largely independent from each other and can have widely distributed individual adhesion strengths [48, 62]. This variation comes from the different types of interfacial defects, i.e., manufacturing imperfections, surface roughness or dust and contaminations, which can lead to an unbalanced strength distribution within the fibrillar array [48]. Moreover, misalignment or unintentional off-center gripping can lead to unreliable gripping of the target object. Thus, it is crucial to monitor the correct grasping to avoid unintended loss of the object.

Microfibrillar grippers are amenable to optical observation of contact formation and breakage. In previous studies [62, 107, 157, 166], vision based tactile sensors were used to analyze the contact of fibrillar adhesives with counter surfaces. Eason *et al.* [107] used frustrated total internal reflection to characterize the stress distribution on gecko toes. This technique was later adopted by Tinnemann *et al.* [62] to investigate in detail the detachment behavior of artificial single fibrils and fibrillar arrays. Pang *et al.* [166] developed and integrated a vision-based tactile sensor for a shear-induced gecko gripper to obtain real-time measurements of contact area and shear force. In our recent work [171], *in-situ* observation coupled with supervised learning regression models was successfully used to predict the adhesion force of microfibrillar surfaces from visual features

extracted from contact images (the "contact signature").

In the present paper, we propose an in-line monitoring system to detect the presence and correct grasping of a glass object using frustrated total internal reflection, FTIR, and supervised learning classification models. These models will be trained on data collected directly using a pick-and-place robotic arm. In this way, we bridge the gap from laboratory adhesion experiments to actual manipulation processes using bioinspired microstructures with improved reliability.

4.3 Materials and methods

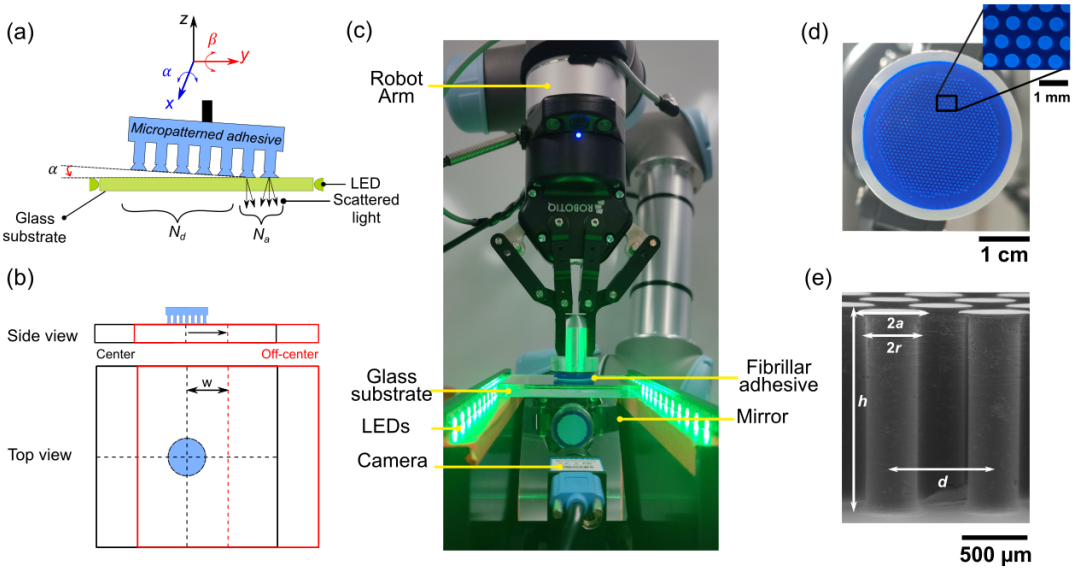

Figure 4.1: Experimental set-up for data collection. a) Schematic illustration of the micropatterned adhesive attaching to a smooth glass substrate. Frustrated total internal reflection enhances the contrast for N_a attached and N_d detached fibrils. Misorientation between the adhesive and the glass surface is introduced by robotic actuation: rotation along x and y axes, resulting in misalignment angles α and β. **b)** Schematic illustration of the off-center gripping where the glass object was moved in one direction with $w \approx 3\,\text{mm}$. **c)** Robotic arm equipped with microfibrillar surface adhering to the glass. LEDs are used for the frustrated total internal reflection. A mirror reflects the contact signature to the camera. **d)** Image of the micropatterned specimen that typically consisted of $N = 844$ fibrils. The inset shows the hexagonal arrangement. **e)** SEM of the mushroom-shaped fibrils.

4.3.1 Preparation of fibrillar arrays

In the present study, eight specimens (S1-S8) of micropatterned polydimethylsiloxane (PDMS, Sylgard 184, Dow, Midland, MI, USA) with 844 mushroom-shaped fibrils were fabricated using replica molding as described in earlier publi-

cations [62, 157]. The fibrils had a length of $h = 1600\ \mu m$, a stalk radius or $r = 200\,\mu m$ and a mushroom tip radius of $a \approx 300\ \mu m$. The center-to-center distance between neighboring fibrils was $d = 800\ \mu m$. A polished brass disc was used to seal the bottom of the mold, which replicated the smooth topography of the brass to the fibril tips. Blue pigments (PK 5091, Degussa, Essen, Germany) were added to the transparent PDMS in order to enhance the optical contrast for the in situ imaging. Exact dimensions of the micropatterned specimens are given in **Table 4.1**.

4.3.2 Robot experimental steps

Experimental data was collected using a pick-and-place robotic arm (Cobot UR5, Universal Robots, Odense, Denmark), see **Figure 4.1 c**. A transparent glass plate was used as the target object. An aluminum ring was attached on top of the object to achieve a total mass of 200, 300, and 400 g. For contact observation, the object holder was equipped with LEDs and a camera in order to implement the principle of frustrated total internal reflection as illustrated in **Figure 4.1 a** and **c**. Light coupled in the transparent glass object was scattered after contacting the object with the fibrillar array, strongly improving the contrast between attached and detached fibrils [62, 157]. For each specimen, 50 pick-and-place cycles were performed by picking the object from the center; in another 50 cycles, the object was grasped off-center with $w \approx 3\,\text{mm}$ as can be seen in **Figure 4.1 b**. After each cycle a random rotation of the robotic arm along the x and y axes was introduced, resulting in the misalignment angles α and β, which ranged between -2 and $2°$. The glass object was cleaned with isopropanol and/or acetone after every 100 cycles to remove dust and contamination.

Before each experiment, the fibrillar adhesive was mounted on the robotic arm and aligned manually with the target object. Since the robot is not equipped with a force sensor, the preload for the different specimens was chosen manually as the first full contact (position 0). Position 0 was fixed by establishing contact through visual inspection, without applying any additional load. However, a slight variation of the preload could result from handling errors. Positions 1 and 2 corresponded to lifting by 2 and 20 mm above contact, see **Figure 4.2 a**. At the start, the robot recorded first two reference images of the contact signature, Ref 0 and Ref 2 at positions 0 and 2 for subsequent analysis. The robot arm moved at a velocity of 10 mm/s, and an acceleration of $40\,\text{mm/s}^2$. For detachment, the arm rotated at a rotation velocity of $25\ mm/s$, and an acceleration of $240\,\text{mm/s}^2$. In order to synchronize robot, camera, and image analysis, 1 to 2 s waiting time was added between the essential steps. A successful "pick" event was defined

after a hold time of 10 s after moving into position 2. The robot was controlled using the UR5 control interface along with a program created using MATLAB (MathWorks, MA, USA). **Figure 4.2 b** presents the flow chart to collect the necessary data.

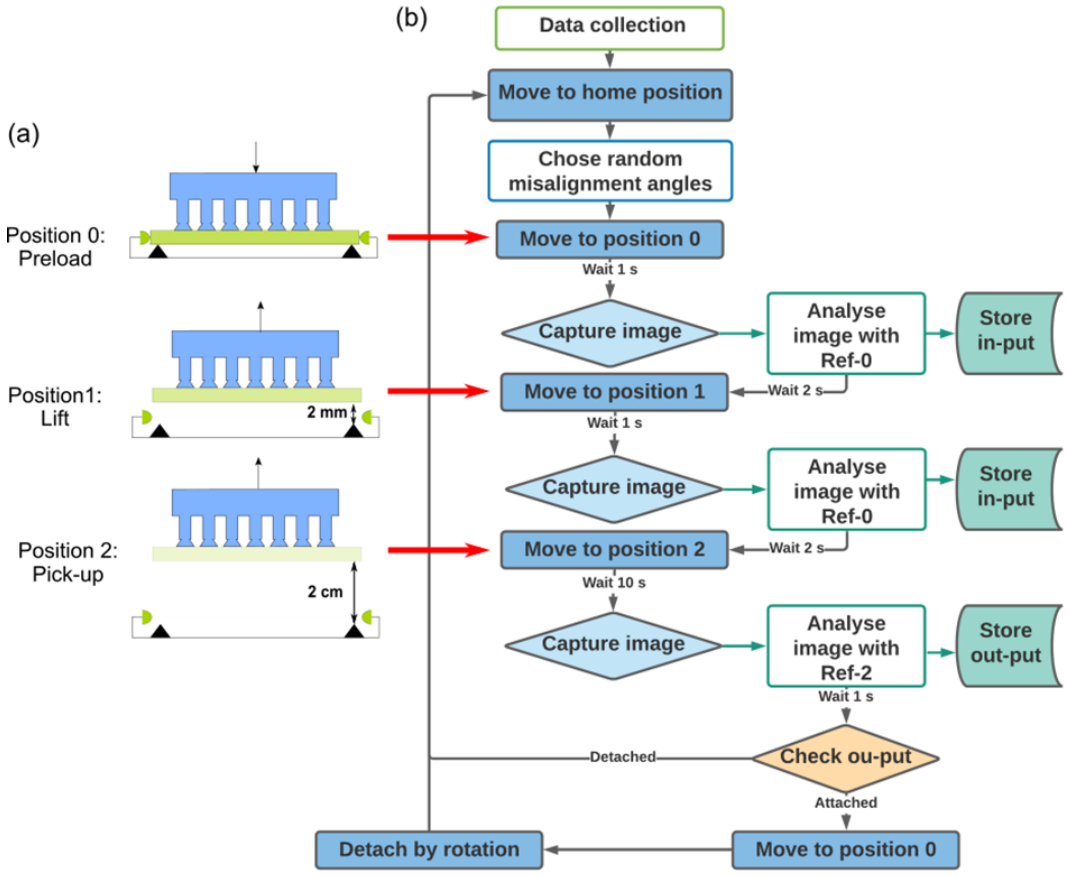

Figure 4.2: Data collection steps and flow chart. a) Schematic illustration of the three different positions for data collection. Position 0: Upon contact between array and object, a first set of visual features is extracted from the captured image (Ref-0). The robot lifts the object to position 1 and a second set of features is extracted. The object is then moved to position 2 where image capture after a hold time of 10 s decides upon a successful pick event. **b)** Flow chart of the experimental steps to collect data using the robot. The home position is the starting position of the robotic arm.

4.3.2.1 Image analysis and features extraction

The images collected at positions 0, 1, and 2 were analyzed using Computer Vision and Image Processing toolboxes from MATLAB as described in detail in our previous report [171]. Binary images were created by selecting a threshold gray value. Pixels with values above the threshold were defined as white and were attributed to fibrils in contact, whereas pixels with smaller values were considered black, indicating non-contact regions. The mean distance between fibrils centroids

$d = 800\,\mu m$, was used to convert from the pixel to the micrometric scale. Multiple inputs were extracted from the binarized contact signature images obtained at positions 0 and 1. The contact area A (A_0 at position 0 and A_1 at position 1) was obtained by calculating the number of white pixels at full or partial contact, see **Figure 4.3 a**. The number of centroids in contact acquired by computer vision represented the number of attached fibrils, N_a, **Figure 4.3 b**.For misaligned grasping, the position of the centroids is used to procure the misalignment vector, i.e. the vector linking the center of mass, C, of the array in full contact in Ref-0 to that in partial contact. The misalignment vector can be represented in polar coordinates by ($|\vec{v}|$,θ) with $|\vec{v}|$ its magnitude and θ its angle with respect to the x axis, see **Figure 4.3 c**. Observations of successful or unsuccessful attachment i.e., out-puts, were obtained by comparing the captured images at position 2 with Ref-2.

Since direct use of the captured images or the pixelated representation of the fibrillar contacts for a deep learning approach was limited by multiple factors (e.g. insufficient amount of data or input resolution below the receptive field size for training convolutional neural networks), the extracted visual features A_0, $N_{a,0}$, $|\vec{v}|_0$, and θ_0 at position 0, and A_1, $N_{a,1}$, $|\vec{v}|_1$, and θ_1 at position 1 were used to train supervised learning models as will be presented in the next section.

4.3.2.2 Machine learning

For creating predictive models, we utilized supervised learning algorithms from the Statistics and Machine Learning toolbox in MATLAB (ver. R2019b). From the visual features obtained, various models were trained using MATLAB's classification learner toolbox. We focused on three models: linear Logistic Regression (LR), non-linear models Support Vector Machines (SVM), and K-Nearest Neighbors (KNN). The experimental data for the three different classifiers was divided randomly into training and testing data at a ratio of 75 to 25 (6 specimens for training and 2 for testing). In addition, six-fold cross-validation was used to optimize the performance of the models and to avoid overfitting during training; for each iteration, 5 specimens were used for training and one for validation. A min-max normalization was used on the extracted features A_0, $N_{a,0}$,$|\vec{v}|_0$,A_1, $N_{a,1}$,and $|\vec{v}|_1$, as follows: $A' = (A - min(A))/(\max(A) - min(A))$. The features θ_0 and θ_1 were normalized by 2π such as: $\theta' = \theta/2\pi$.

For each of the chosen models, 3 classifiers were created. The first was trained using features extracted only from position 0 (A'_0, $N'_{a,0}$,$|\vec{v}|'_0$, θ'_0), the second using the features from the image at position 1 (A'_1, $N'_{a,1}$, $|\vec{v}|'_1$, θ'_1,), and the final one using all the features.

The trained classifiers were evaluated by the validation accuracy calculated by

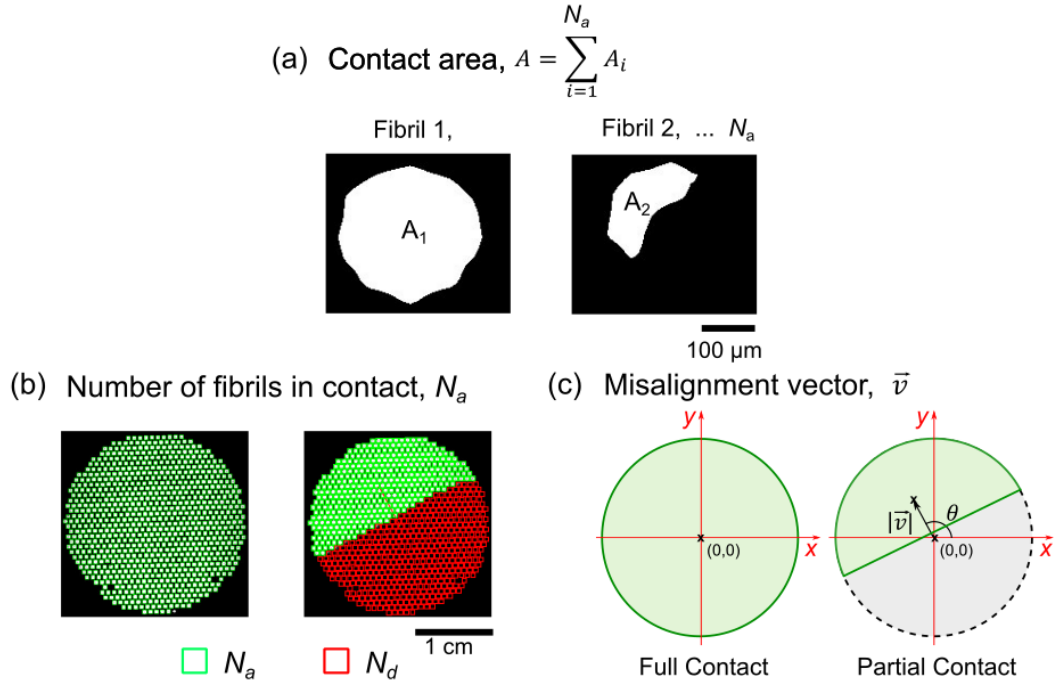

Figure 4.3: Capture of visual features corresponding to contacting fibrillar arrays. a) Full (left)/partial (right) contact of individual fibrils. The sum of the contact areas of all attached fibrils provides the total contact area, A. **b)** Full (left) /partial (right) contact of the array, where green corresponds to N_a attached, red to N_d non-attached fibrils. **c)** Misalignment vector (black arrow), $\vec{v}$, pointing from the centroid of complete contact to that of partial contact, and θ_1 its angle with respect to the x-axis.

$(Tp+Tn)/(Tp+Tn+Fp+Fn)$, and by plotting the confusion matrices for the test data, which included the values for true-positive Tp (True predicted attachment), true-negative Tn (True predicted detachment), false-positive Fp (False predicted attachment), and false-negative Fn (False predicted detachment). For these values, the precision, P, recall, R ,and score, F_1, can be calculated by $P = Tp/(Tp+Fp)$, $R = Tp/(Tp+Fn)$, $F_1 = 2PR/(P+R)$.

4.3.3 Adhesion properties of the specimens

To characterize the quality of the 8 specimens, pull-off forces and statistical properties of the fibrillar adhesives were measured using a customized tensile tester (Inspekt table BLUE, Hegewald & Peschke, Nossen, Germany) equipped with a 50 N load cell, a camera, and the FTIR system for *in-situ* observation. The array was brought into contact with the target object (a smooth glass substrate), at a velocity of 1 mm/min until a prescribed compressive load of 1 N, was reached. The array was then instantly retracted at the same velocity. The highest tensile force was reported as the pull-off force, F_p. The stiffness, k, of the fibrillar surface was obtained from force-displacement curves in the compressive regime after de-

ducing the load cell stiffness: $k_{50} = 134.6\,\mathrm{Nmm}^{-1}$ (from $1/k = 1/k_{slope} - 1/k_{50}$). Videos of the tests were recorded and correlated with the force-displacement measurement. To characterize the spread of the distribution of individual fibril pull-off forces, a cumulative Weibull distribution was fitted (**Eq.2.2** in section **2.1.4**, see also [63, 64]). The Weibull moduli, m, and the reference elongations, u_0, of the arrays are reported in **Table 4.1**.

4.4 Results and discussion

4.4.1 Distributions of fibril and of array strengths

The pull-off force measured for the different specimens ranged between 14 N for the weakest array S4 and 22 N for the strongest array S3, see **Table 4.1**. As the glass surface was free of contaminants, the likely reason for this distribution lies in the limitations of the replica molding process: surface defects and deviations in fibril radius induced a spread in pull-off strength across each array. These variations were quantified by fitting Weibull distributions (**Eq.2.2** in section **2.1.4**) and extracting characteristic values as explained in previous reports [48, 63, 64], and presented in **Table 4.1**.

Table 4.1: Dimensions and quality variations of the specimens in terms of the pull-off force, F_p, the pull-off stress,σ, the stiffness of the specimen, k, the Weibull moduli, m, and the reference elongation, u_0. Data for the diameter represent mean values and standard deviations of 10 randomly selected fibrils.

Specimen	a (µm)	N	σ	F_p (N)	k (kN/m)	m	u_0
S1	284.4±16.7	842	78.4	16.79	68.9	2.8	0.6
S2	278.9 ± 8.5	841	89.5	18.4	105.58	3.6	0.51
S3	264 ± 5.5	842	119.4	22.01	78.65	5.4	0.72
S4	264.3 ± 6.9	837	77.4	14.22	78.96	4.7	0.58
S5	257.3 ± 6.1	841	86.4	15.12	87.24	3.7	0.51
S6	249.6 ± 8.1	811	112.1	17.78	94.9	5	0.5
S7	247.7 ± 9.2	844	93.8	15.27	86.8	4	0.41
S8	256.3 ± 9.9	844	87.4	15.22	81.7	5.9	0.33

4.4.2 Contact signatures for misaligned gripping

Figure 4.4 a, b, and **c** show the random distribution of the misalignment angles β and α chosen during data collection for different object masses. **Figure 4.4 d** displays contact signatures at preload for specimens S1 (**i** and **ii**) and specimens S2 (**iii**) divulging the variation of the number of attached pillars N_a for similar misalignment angles ($\alpha \sim 0.6°$ and $\beta \sim 0.02°$). This variation is a result of the slight preload variation from the manual definition of position 0 for

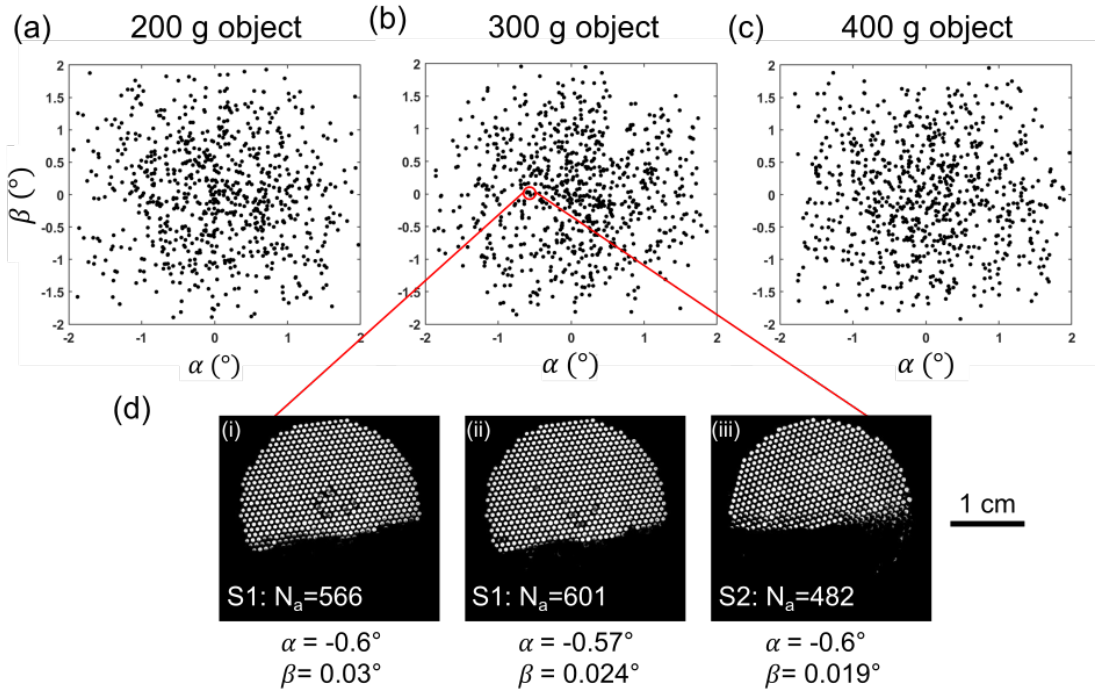

Figure 4.4: Variation of the misorientation. a-c) Rotation angles of the robotic arm β versus α, both ranging between -2 and 2°. Misorientation data for the different objects with mass **a)** 200 g, **b)** 300 g, and **c)** 400 g. **d)** Exemplary images of the contact at preload for specimens S1 (**i** and **ii**) and S2 (**iii**) with similar rotation angles, showing a variation in the number of fibrils in contact, N_a.

the different specimens. Moreover, the robot arm has a repeatability error of 100 µm when reaching a preset position. This can explain the significant difference in number of attached fibrils, N_a, for a similar preset values of α and β between different specimens ($N_{a,S1} = 566$ and $N_{a,S2} = 482$) and for two cycles of the same specimen ($N_{a,S1(i)} = 566$ and $N_{a,S1(ii)} = 601$) .

The patterned adhesives were successfully used to train the pick-and-place handling of glass objects with a mass of 200, 300, and 400 g. The data set obtained comprised 800 data points for each of the objects. This data included intentional variations such as the preset degrees of misalignment or balanced/unbalanced gripping due to variations of the gripping position and unpremeditated variations attributed to specimens' quality variations, inaccuracies in robot arm movements, or slight preload variations.

4.4.3 Effect of misalignment and off-center gripping

Figure 4.5 shows the combined effect of misaligned contact and off-center gripping after lifting the object to position 1. The unbalanced attachment induces a moment, M, leading to a rotation of the glass object. In **Figure 4.5 a**, the

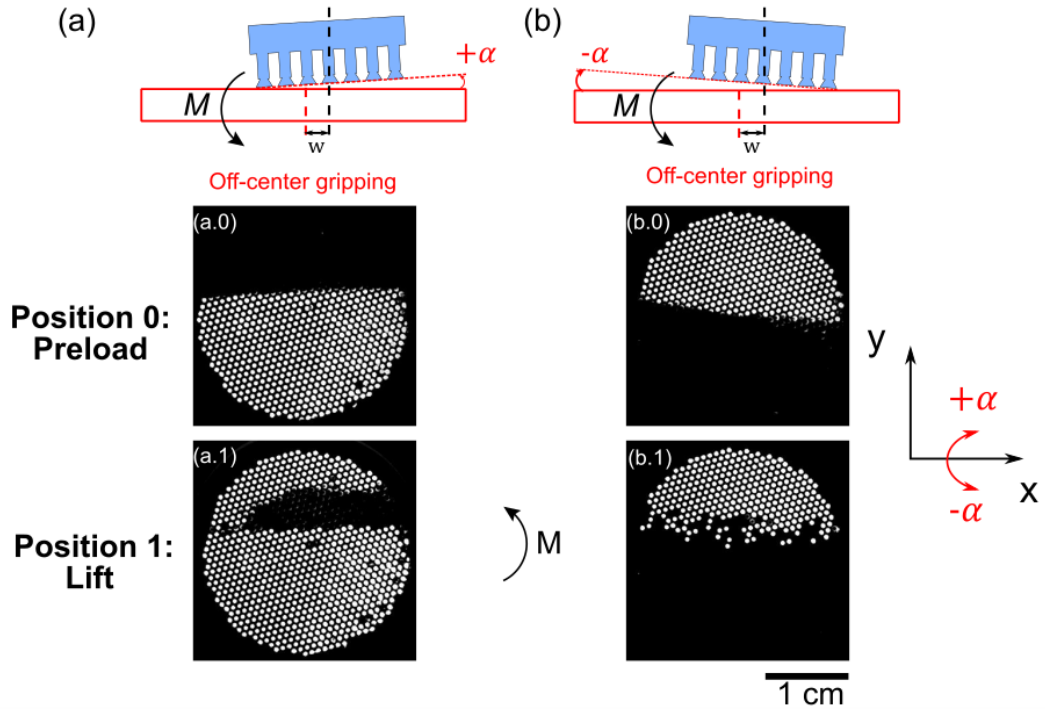

Figure 4.5: Rotation of the object during off-center attachment. a) The object rotates anti-clockwise similar to the rotation of the robotic arm, which potentially leads to the attachment of previously detached fibrils. This is shown in the images below taken at preload (position 0) and after lifting (position 1). **b)** The object rotates oppositely to the rotation of the robotic arm, which potentially leads to peeling. This is again shown by the images below.

rotation of the glass is similar to the rotation of the robotic arm (anti-clockwise) around the x-axes, which leads to the attachment of additional fibrils and counters the detachment, as can be seen on the image (**a.1**) at position 1. In contrast, when the rotation of the object is in the opposite direction to the robot arm rotation, a peeling moment is created and fast detachment can be observed, see **Figure 4.5 b**, image (**b.1**). The aim of the machine learning process is to anticipate these processes and thereby increase the reliability of handling.

Figure 4.6 depicts the misalignment vector $\vec{v}$ ($|\vec{v}|$,θ) in the polar coordinate system, grouped by the output results for the different object masses. The distance of each dot to the center corresponds to the length of the vector, $|\vec{v}|$, ranging between 0 and 10 mm. The angle of the misalignment vector, θ, is designated by the position of the dots in the polar plot and ranges between 0 and 2π.The blue dots represent successful attachment, while the red dots correspond to detachment (unsuccessful attachment). **Figure 4.6 a, c,** and **e** correspond to data collected at position 0, i.e., at maximum preload. The fraction of successful attachments decreased with increasing object mass: for the lighter (200 g) object, 71.4 % of the manipulations were successfully attached while only 38.1 % of the

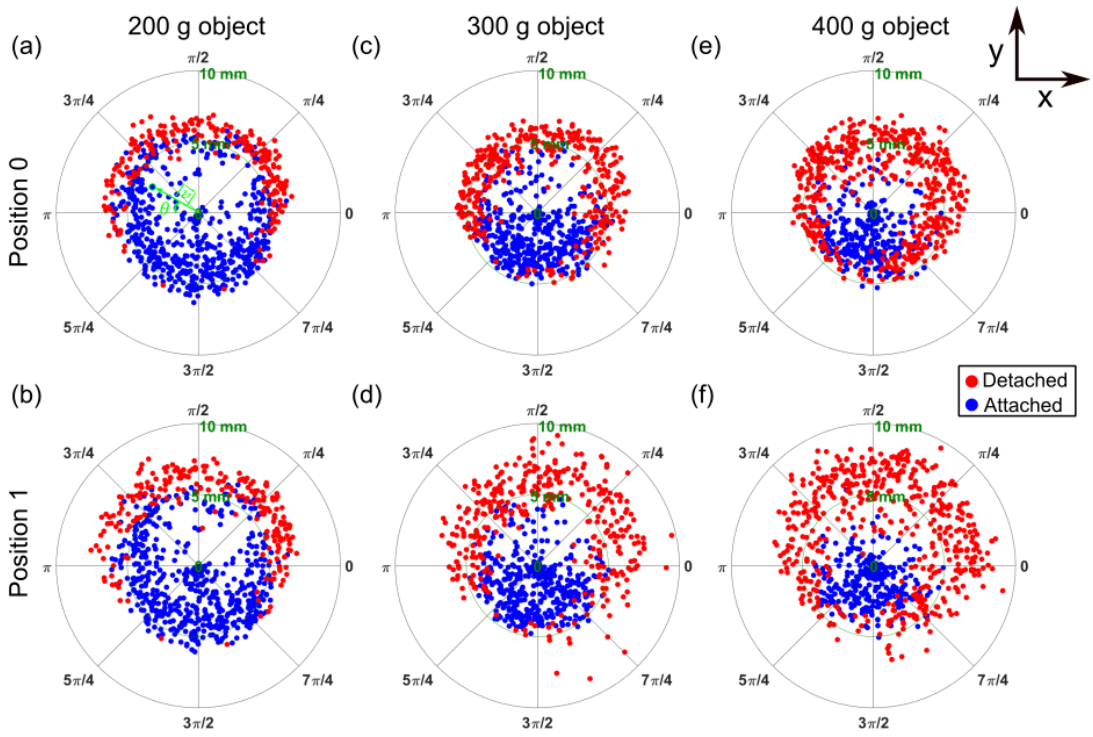

Figure 4.6: Misalignment vector, $\vec{v}$ in polar coordinate grouped by the output results attached (blue) and detached (red). Upper row **(a,c,e)** corresponds to contact images collected at preload (position 0), whereas the lower row **(b,d,f)** corresponds to contact images collected upon lifting at position 1. Columns correspond to the masses of the object of 200, 300, and 400 g. Each dot represents the length of the vector, $|\vec{v}|$ ranging between 0 and 10 mm and the misalignment angle, θ.

trials were successful with the 400 g object. For the 300 g object, the attachment to detachment ratio was about 1:1, see **Table B1** in SI. **Figure 4.6 b, d,** and **f** correspond to data collected at position 1.

The misalignment vector data collected at position 0 appears to be condensed around the center. After lifting the object to position 1 some of the data signifying detachment (red dots) expand in the y direction as the misalignment vector elongates. This can be related to the off-center gripping shown in **Figure 4.5 b**, where the peeling moment leads to the detachment of some fibrils after lifting and causes detachment of the object. The blue dots (attachments) on the other hand congregate around the center because in some cases the off-center gripping improves the contact during lifting as can be seen in **Figure 4.5 a**. The effect of off-center gripping on the misalignment vector after lifting increases as the mass of the glass object increases (the expansion and congregation of the data for the 400 g object is more pronounced than for the 200 g).

4.4.4 Supervised machine learning

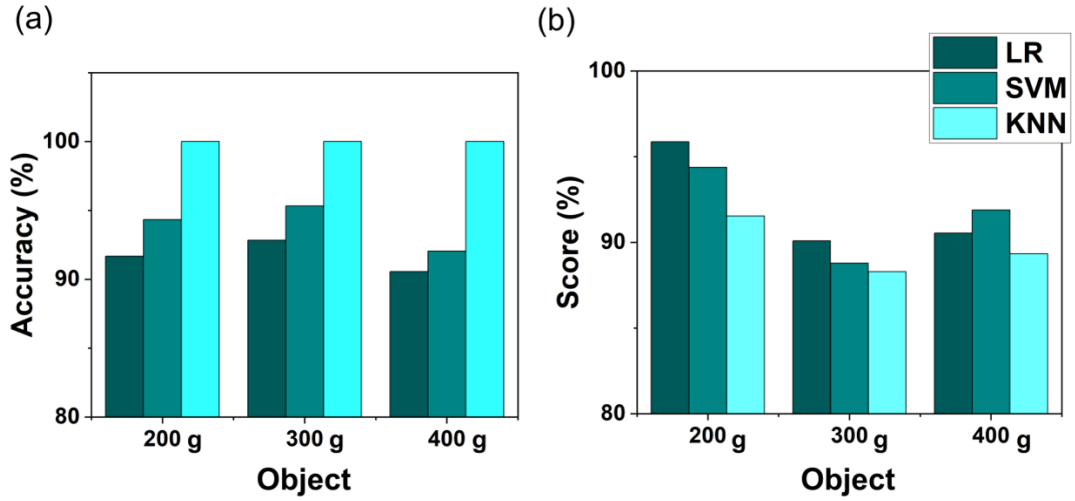

Figure 4.7: Classification results of three classifiers. a) The validation accuracy (training) and **b)** the score (testing) of the support vector machines (SVM), logistic regression (LR), and k nearest neighbors (KNN) trained by the three objects.

The normalized features, collected from the contact images at position 0 (A'_0, $N'_{a,0}$,$|\vec{v}|'_0$, θ'_0), and position 1 (A'_1, $N'_{a,1}$, $|\vec{v}|'_1$, θ'_1,), were implemented into supervised machine learning models to train and compare multiple classifiers. The classification models enable the prediction of attachment/detachment depending on the mass of the object. **Figure 4.7 a** depicts the accuracy of the training data as a function of the object mass for three different classifiers: support vector machines (SVM), logistic regression (LR), and the k-nearest neighbor (KNN).For all trained classifiers the accuracies obtained were always higher than 90 %, with KNN exhibiting an 100 % validation accuracy and LR showing the lowest accuracy ($\sim$ 90 %).However, this trend changes when testing the models with the remaining testing data. **Figure 4.7 b** shows the score of the testing data for the different trained classifiers. LRscores highest for the 200 g object at 95 % and for the 300 g object at 90 %. SVM has the highest score for the 400 g and comes in second for the other classifiers. The testing of KNN reveals the incapability of the model to adapt to new data as the score of the KNN comes in the third position for the three different object masses.

The confusion matrices in **Figure 4.8** and the column graphics in **Figure 4.9** depict the comparison ofLR trained first with features extracted at position 0,$P_0(A'_0, N'_{a,0}, |\vec{v}|'_0, \theta'_0)$ (**Figure 4.8 a**) , at position 1 $P_1(A'_1, N'_{a,1}, |\vec{v}|'_1, \theta'_1,)$ (**Figure 4.8 b**) , and the combined features from position 0 and 1, $P_{0,1}$(**Figure 4.8 c**). The number of false positives, Fp, and false negatives, Fn, diminished when features obtained at lifting position were included in the train-

ing. For the 200 g object, for example, 21 data points out of 40 true detachments were falsely predicted as attached when using only features from position 0, 16 when using features from position 1, and only 4 when using all features. The effect of the unbalanced distribution of the two result groups in the collected data is shown in the confusion matrices for the 200 and 400 g objects by the large variation between the true positives and true negatives.

As can be seen in **Figure 4.9**, the classifier P_0 has the lowest score with a maximum of $\sim 90\,\%$ for the 200 g object and only 71 % for the 400 g object. This drop can be explained by the lack of information in the data at position 0 about the off-center gripping, where the influence is more pronounced for the heavier objects. The score for the 400 g increases to 84 % for the classifier P_1, as more information is included. Combining the features in both positions (position 0 and 1) resulted in an increase of the accuracy and score for all the classifiers $P_{0,1}$ to more than 90 %. The remaining 5 to 9 % for perfect prediction could be attributed to the unbalanced distribution of the two result groups (attached/detached) in the collected data, see **Table B1** in SI, and to the undesirable variations that are not fully shown in the obtained features, which may induce the wrong classification. The confusion matrices and classifiers comparisons of the SVM, and KNN models are shown in **Figure B2** and **B3** in the SI. The accuracy, precision, recall, and score of all the models are presented in **Tables B2 to B10** in SI.

Overall, the high prediction accuracies demonstrated in this paper as a result of *in-situ* observation at two positions are encouraging as the method can therefore significantly increase the reliability of object handling with micropatterned adhesives. In particular, the inclusion of data from the lift position to train the classification models will allow an impending peeling to be readily anticipated; dramatic detachments and loss of objects could hence be avoided. Also, the reliability of handling asymmetric objects with various geometries and forms can profit. More specifically, the data collected directly using the robotic arm bridge the gap between laboratory adhesion experiments in displacement-control and the actual pick and place application under force-controlled loading [59, 64]. Certain limitations of the present approach should be noted. The trained models are highly related to the relevant application circumstances, such as object weight, the trajectory of the robot arm, and waiting times between different steps. Moreover, possible effects of additional parameters such as velocity and acceleration of the robot arm were not taken into consideration. Optimization of the experimental training data and development of new optical techniques compatible with opaque and rough objects bear great potential to significantly improve in-line control of handling processes even in demanding conditions.

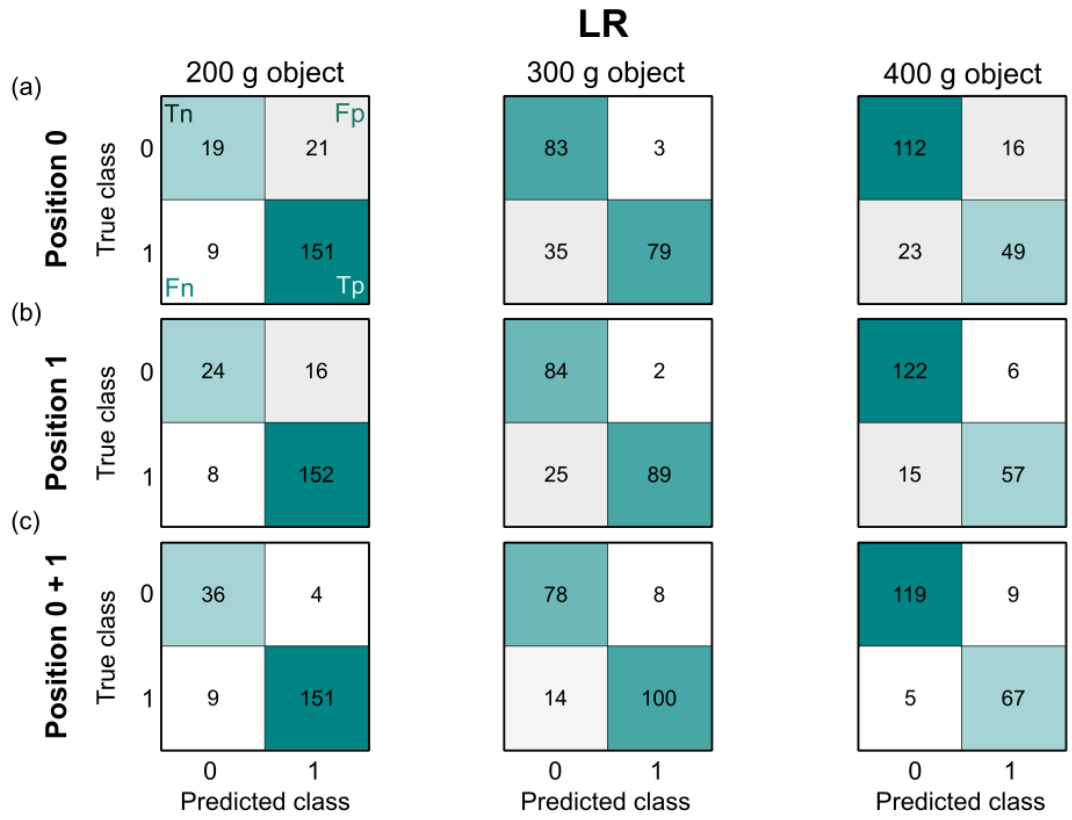

Figure 4.8: Confusion matrices of the different classifiers trained with the logistic regression (LR) model. Each matrix represents the total number of true negative (Tn), true positive (Tp), false negative (Fn) and false positive (Fp). Columns correspond to the masses of the object of 200, 300, and 400 g. **a)** Classifiers trained using data at preload (position 0). **b)** Classifiers trained using data upon lifting (position 1). **c)** Classifiers trained using data from positions 0 and 1.

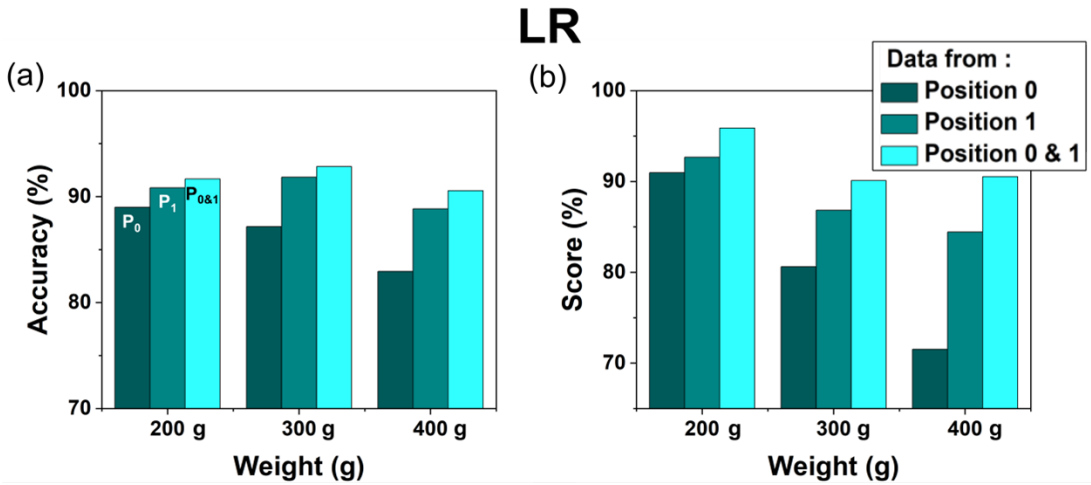

Figure 4.9: Comparing input data for the logistic regression (LR) model. **a)** The validation accuracy (training) and **b)** the score (testing) of three objects with the mass 200, 300, and 400 g when trained by data from position 0, P_0, position 1, P_1, and position 0 and 1, $P_{0\&1}$.

4.5 Conclusions

In this work, we present an in-line monitoring system using supervised learning classification models, optical observation, and image processing. Three classification models were trained and tested using visual features obtained from the contact signature at preload and after lifting the glass object. Successful and unsuccessful attachment of the object was demonstrated in a pick and place application. The following conclusions can be drawn:

- The performance of micropatterned adhesives can be affected by intentional or unintentional variations, notably, prescribed misalignment and off-center gripping or quality of the adhesive and preload/displacement variations attributed to the limited robot arm accuracy.
- All tested classifiers showed accuracies higher than $\sim 90\,\%$ for predicting impending attachment or detachment as a function of the objects mass. The highest testing score was obtained for logistic regression.
- Observation of the contact signature at compressive preload alone, i.e. before lifting of the object, resulted in a high predictive capability (between 70 and 90 %). Including data from the lifting position significantly increased the accuracy and score of the different trained models (to more than 90 %).

The present machine learning process is proposed as a means of enhancing the reliability of handling with micropatterned adhesives. It can furthermore be used to identify the degradation and wear of the polymeric micropatterns.

Supporting information: chapter 4

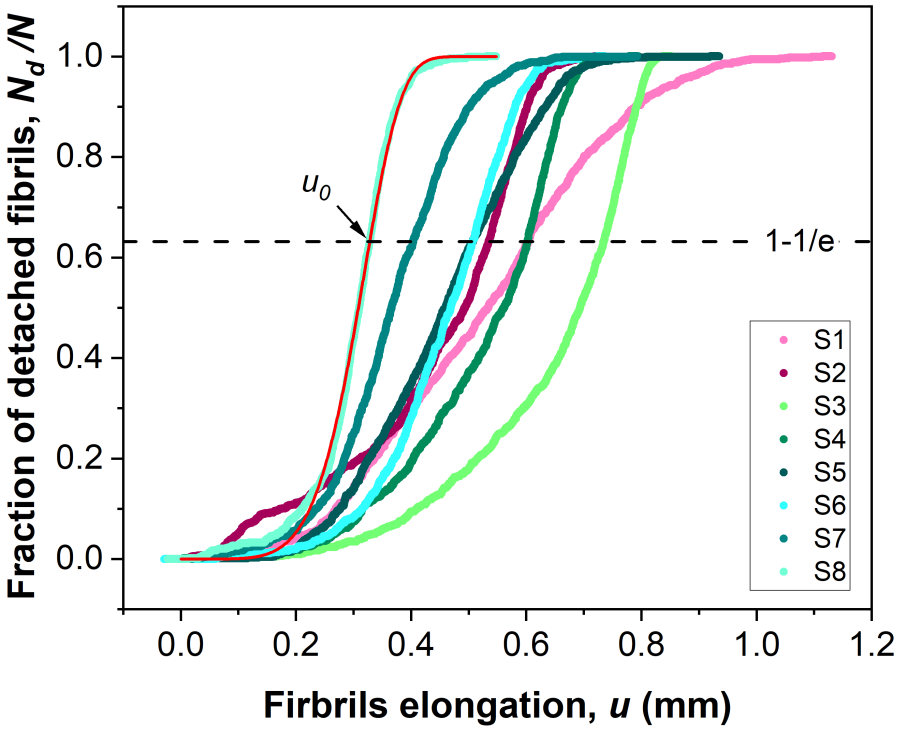

Figure B1: Fraction of detached fibrils in terms of the fibril elongation, u, for the used specimens. The red line on S8 is the fitted Weibull distribution given by **Eq.2.2** in section **2.1.4**. The reference elongation u_0 is assigned to $N_d/N = 1 - 1/e$ (represented by the dashed line)

Table B1: Ratio of attachment and detachment results for the different object masses.

Object	Attached (%)	Detached (%)
200 g	71.37	28.63
300 g	55.12	44.88
400 g	38.06	61.94

Table B2: Validation accuracy, and the testing precision, recall, and score for the 200 g classifier trained on data obtained for the image at preload.

Model	Validation accuracy (%)	Precision (%)	Recall (%)	Score (%)
LR	89	87.79	94.38	90.96
SVM	90.5	87.86	95	91.29
KNN	100	87.43	91.25	89.3

Table B3: Validation accuracy, and the testing precision, recall, and score for the 200 g classifier trained on data obtained for the image at the first pick-up position.

Model	Validation accuracy (%)	Precision (%)	Recall (%)	Score (%)
LR	90.83	90.48	95	92.68
SVM	93	90.48	95	92.68
KNN	100	89.76	93.13	91.41

Table B4: Validation accuracy, and the testing precision, recall, and score for the 200 g classifier trained on data obtained for the image at preload plus the first pick-up position.

Model	Validation accuracy (%)	Precision (%)	Recall (%)	Score (%)
LR	91.67	97.42	94.38	95.87
SVM	94.33	94.38	94.38	94.38
KNN	100	91.82	91.25	91.54

Table B5: Validation accuracy, and the testing precision, recall, and score for the 300 g classifier trained on data obtained for the image at preload.

Model	Validation accuracy (%)	Precision (%)	Recall (%)	Score (%)
LR	87.17	96.34	69.3	80.61
SVM	88.83	95.35	71.93	82
KNN	100	90.43	74.56	81.73

Table B6: Validation accuracy, and the testing precision, recall, and score for the 300 g classifier trained on data obtained for the image at the first pick-up position.

Model	Validation accuracy (%)	Precision (%)	Recall (%)	Score (%)
LR	91.83	97.8	78.07	86.83
SVM	94.17	95.79	79.82	87.08
KNN	100	93.00	81.58	86.92

Table B7: Validation accuracy, and the testing precision, recall, and score for the 300 g classifier trained on data obtained for the image at preload plus the first pick-up position.

Model	Validation accuracy (%)	Precision (%)	Recall (%)	Score (%)
LR	92.83	92.59	87.72	90.09
SVM	95.33	90.83	86.84	88.79
KNN	100	90.74	85.96	88.29

Table B8: Validation accuracy, and the testing precision, recall, and score for the 400 g classifier trained on data obtained for the image at preload.

Model	Validation accuracy (%)	Precision (%)	Recall (%)	Score (%)
LR	82.95	75.38	68.06	71.53
SVM	84.44	75.38	68.06	71.53
KNN	100	70.79	87.5	78.26

Table B9: Validation accuracy, and the testing precision, recall, and score for the 400 g classifier trained on data obtained for the image at the first pick-up position.

Model	Validation accuracy (%)	Precision (%)	Recall (%)	Score (%)
LR	88.85	90.48	79.17	84.44
SVM	89.9	84.51	83.33	83.92
KNN	100	85.92	84.72	85.31

Table B10: Validation accuracy, and the testing precision, recall, and score for the 400 g classifier trained on data obtained for the image at preload plus the first pick-up position.

Model	Validation accuracy (%)	Precision (%)	Recall (%)	Score (%)
LR	90.56	88.16	93.06	90.54
SVM	92.05	89.47	94.44	91.89
KNN	100	85.90	93.06	89.33

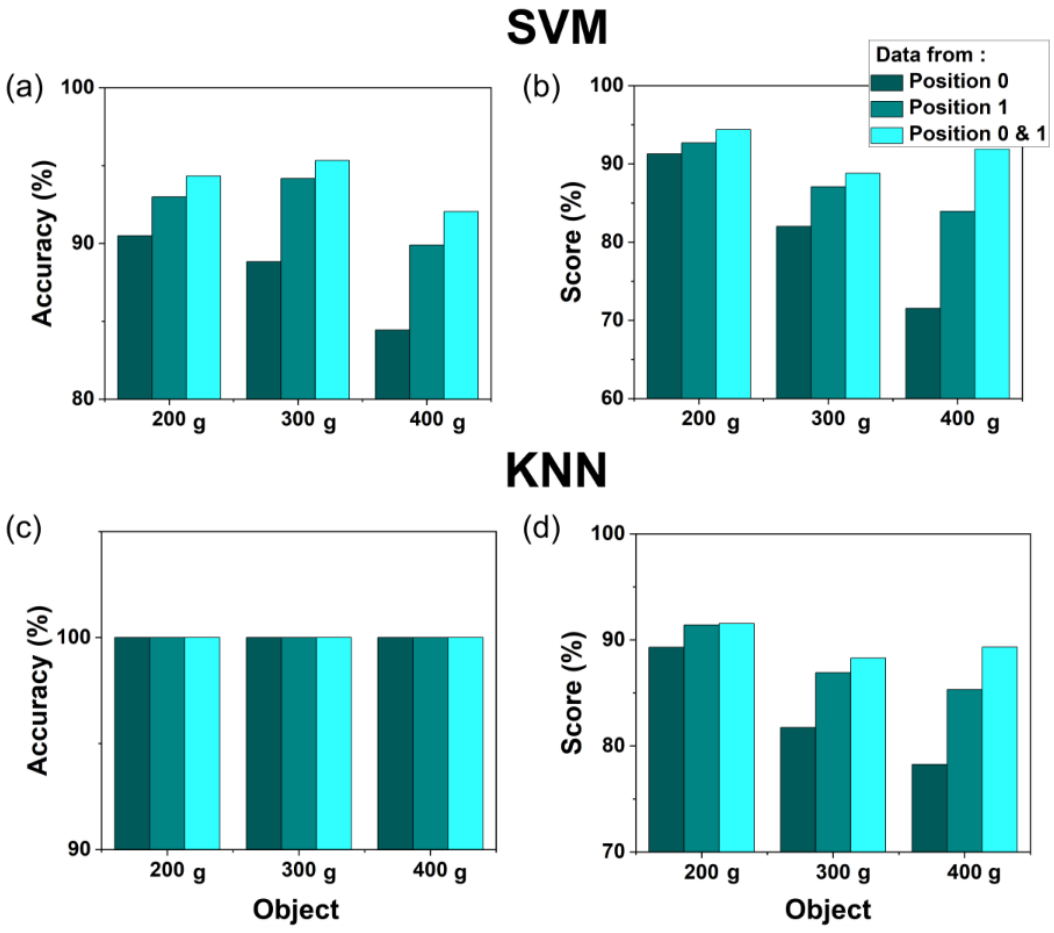

Figure B2: Classification results for the trained models. a-b) Accuracy and score for the trained classifiers for the three objects with the mass 200, 300, and 200 g using SVM. **c-d)** using KNN.

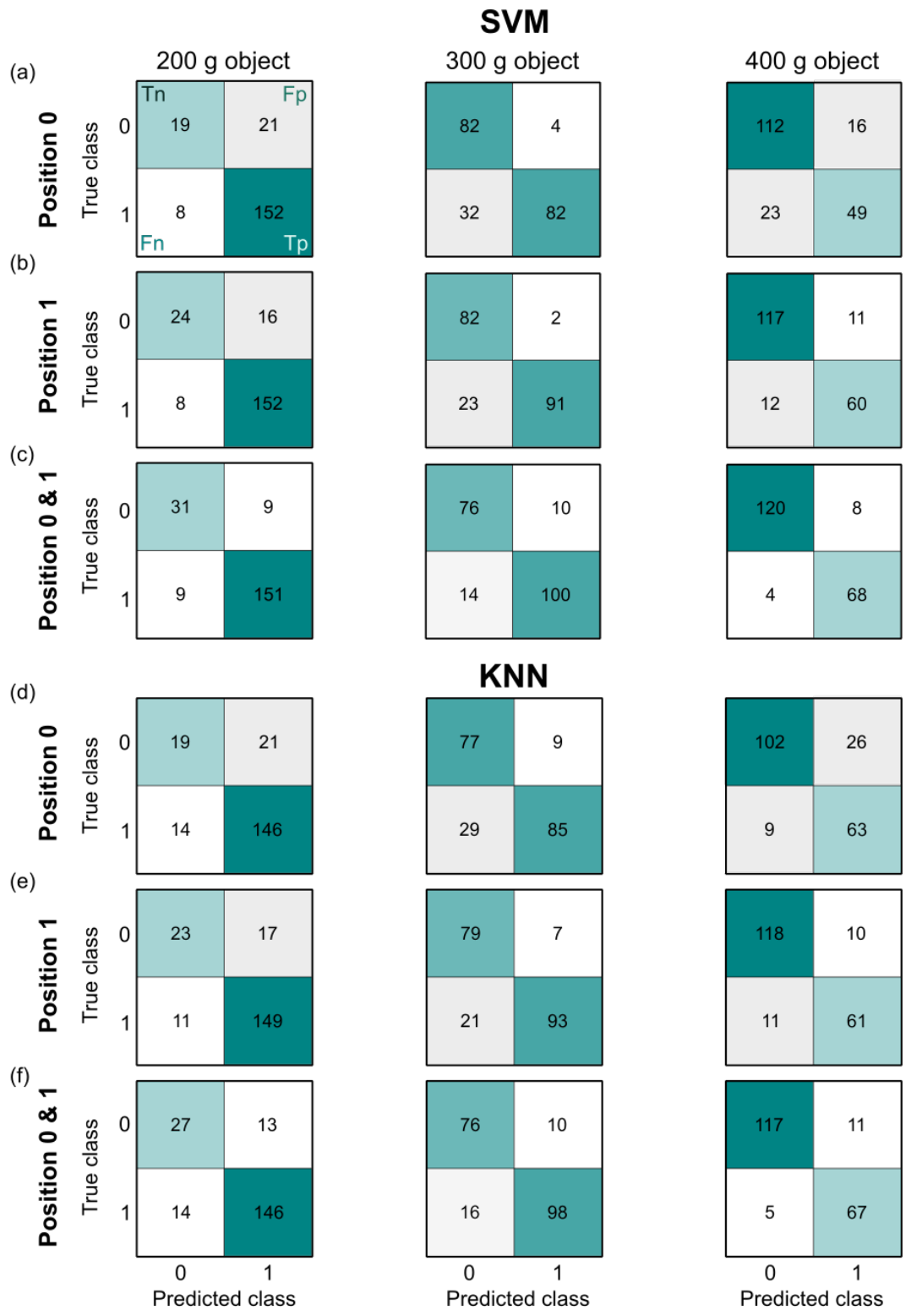

Figure B3: Confusion matrices for the different trained classifiers. a, b, c) using SVM. **d, e, f)** using KNN.

Chapter 5

Novel optical system for observing the contact signature of bio-inspired fibrillar structures by looking through the fibrils.

5.1 Abstract

Bioinspired fibrillar microstructures are in the process of revolutionizing gripping processes. Besides the inherent resource-efficiency and sustainability, a decisive advantage would be the ability of observing the microfibrillar contacts with a target object during gripping and detachment. We propose two newly developed optical systems that allow direct observation of the interfacial contrast, termed the 'contact signature'. The proposed tools can detect and quantify contact with various types of surfaces and objects (smooth, rough, and opaque) during pick-and-place processes. By improving the reliability of handling, they will also improve the acceptance of the new handling concept.

5.2 Introduction

In the last few years, a new generation of grippers has been developed based on gecko-inspired fibrillar structures [1, 6]. With switchable and residue-free adhesion, these fibrillar grippers are gradually making their way to the market. Based on molecular van der Waals interactions, the new technology has the potential to overcome the limitations of conventional grippers [9, 10, 162, 165, 172]. Fibrillar microstructures can be designed to exert small compressive preloads for handling fragile objects, and they work effectively in both air and vacuum conditions [1,78,155]. However, failure of the fibrillar gripper to correctly pick and place an object can have serious consequences in application (causing the destruction of the picked object or slowing the production line). Adhesion failure of these structures can come from various factors that affect the intimate contact with the target surface, such as interfacial defects at the fibrillar scale [48, 51, 63, 64], roughness of the target's surface [44, 56], or inaccuracies in the alignment with the object [53, 54]. Therefore, monitoring the effectiveness of gripping is crucial for a reliable function [152]. It can improve the gripping quality by detecting anomalies in the contact [171]. Optical inspection of contact formation and detachment could provide valuable information. In fact, contact observation has great importance in both scientific research for understanding different physical mechanisms such as adhesion and tribological processes [62,106–108,173–175] and for monitoring industrial applications [166, 176].

Observing the contact between two surfaces is a classical technique: Newton attributed the emergence of rings to the interference of light paths, a technique that was exploited by McCutchen for contact examination [106]. Using the interferometric technique, Krick *et al.* [108] developed an *in-situ* optical micro tribometer to investigate the intimate contact between solids during loading and sliding experiments. Another technique that proved to be efficient in enhancing contrast is coaxial illumination. It was used in different fields for process control and contact observation [112–114]. In order to observe surface topography, frustrated total internal reflection has been used since the 1960s [105, 106] and was later adopted, e.g., for the estimation of the stress distribution on gecko's toes [107]. The present authors used the technique for *in-situ* observation of contact formation and separation of micropatterned adhesives in contact with a glass surface [48, 62, 64, 157, 171, 175]. This enabled the understanding of the statistical behaviour of detachment in these structures [48, 64]. When combined with machine learning and image processing, this technique allowed us to monitor and predict the adhesion performance of the fibrillar structures [171].

Although these techniques have been successfully used for multiple applica-

tions, they rely on observing the contact with transparent smooth objects. As a result, contact monitoring is limited or not possible in the case of rough surfaces and/or opaque objects. In order to solve this limitation, we present two new optical systems. Placed in the back of the transparent fibrillar structure, the optical instruments allow contact observation with various types of objects by looking through the fibrils. We present a comparison of the two devices and the resulting contrast variations using an image quality assessment technique [177], and discuss their strengths and limitations.

5.3 Materials and methods

5.3.1 Description of the *in-situ* optical systems

Two approaches for contact observation, with different aspects and requirement profiles, were developed. The principles are illustrated in **Figure 5.1**.

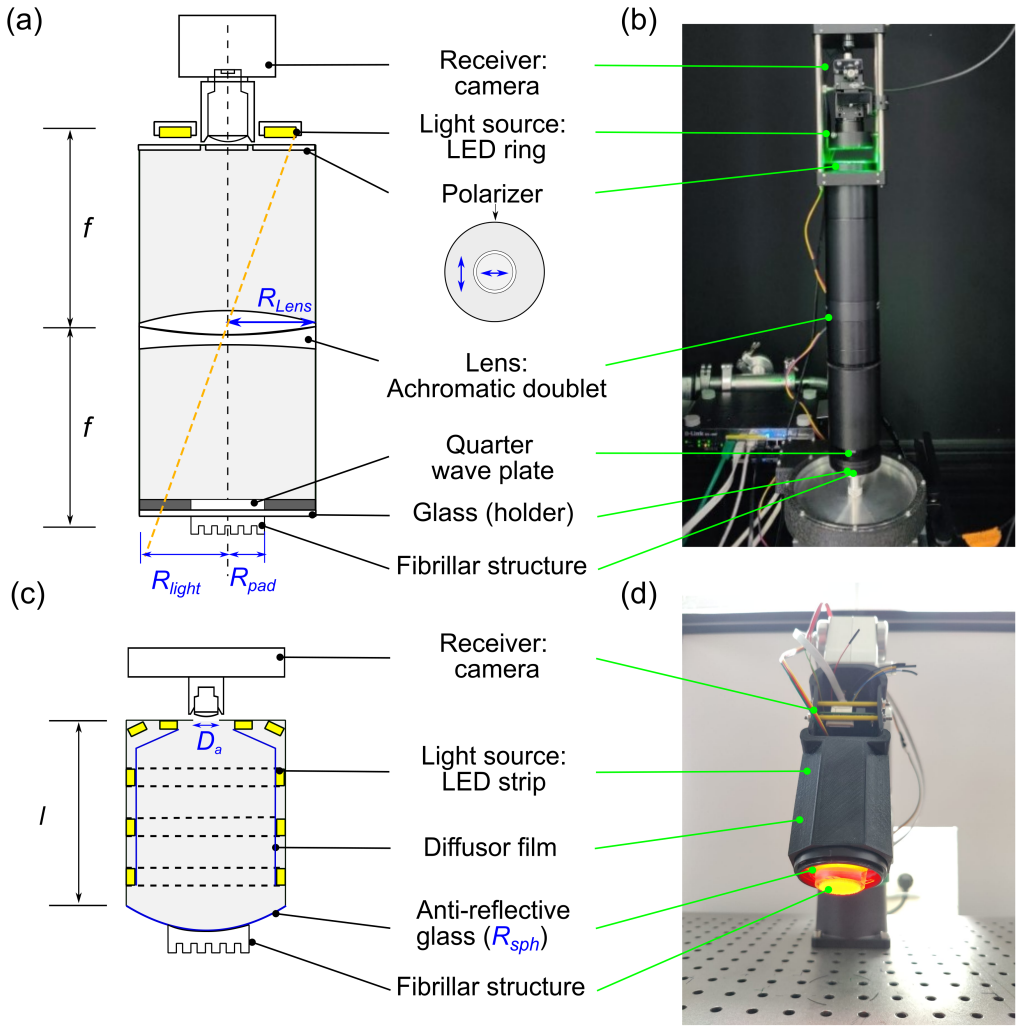

Figure 5.1: Schematic and images of the two setups for the observation of gecko-inspired gripper contact signature. . **a,b)** The "precision setup" composed of a receiver (camera), a light source (LED ring), a polarizer, an achromatic doublet lens with a focal point $f = 15\,\text{cm}$, and a quarter wave plate. The fibrillar structure is fixed on a transparent glass holder. **c,d)** The "compact setup" consist of a camera, a light source (LED strip) covered with a diffusor film. The fibrillar structure is fixed on an anti-reflective glass. Total height $l = 8.8\,\text{cm}$. In both setups the intensity of the multicolor LED light sources could be varied in four steps referred to as intensity levels 1 through 4 later on, corresponding to approximately 25% / 50% / 75% / 100% of the maximum brightness, respectively.

The first setup, called "precision setup", attempts to maximize the homogene-

ity of observation conditions over the area of the gripper. This is accomplished using a lens (an achromatic doublet to reduce aberrations) such that the tips of the fibrils are in the focal plane, whilst the receiver and the light source are located in the back focal plane. The receiver is simply a camera with an objective lens focused to infinity, and the light source is a ring of RGB LEDs (red, green, blue) around the camera lens. This setup ensures equal angular distributions of the incident light for all fibrils, and each fibril is observed exactly from the top. Note that this is a dark field configuration, as the reflection from a flat surface perpendicular to the axis of the setup will not hit the camera. Any edges, scattering centers, and curved surfaces will thus be highlighted, leading to high contrast.

To block unwanted reflections that may arise from the surfaces of the lens, polarized light with orthogonal polarization directions for light source and receiver is used. A quarter wave plate above the microstructure provides the rotation of the polarization direction required for observation. As this first setup is rather complex and bulky, a second "compact setup" using a more minimalistic approach was also tested. The light source is here composed of an LED stripe (with 78 LEDs) curled up inside a 3D printed tube. The LEDs are covered with a diffusor film to increase the homogeneity of the illumination. The camera observes the fibrillar structure directly through a small aperture in the top of the tube with a diameter $D_a = 3\,\text{mm}$. The fibrillar structure is mounted on a transparent CR-39 glass holder (Poly (allyl diglycol carbonate), PADC) as will be explained in section **5.3.2**. The curvature of the glass with a radius $R_{sph} = 112\,\text{mm}$ is chosen such that reflections from the back side into the camera are minimized. An antireflection coating on the glass helps to reduce the influence of unwanted reflections even further.

5.3.2 Microfibrillar adhesives and target surface fabrication

Mushroom-shaped fibrillar structures were fabricated using a replica molding technique, as described in earlier reports [62, 157]. The pre-polymer mixture of polydimethylsiloxane (PDMS) was prepared from the transparent SYLGARD 184 silicone elastomer kit (DOW Corning Corporation, Midland, USA) in a 10:1 ratio of the base and the curing agent. The PDMS pre-polymer was thoroughly mixed using a speedmixer and cross-linked in an oven at 95 °C for 1 h. The specimen used for the precision setup was bonded to the glass holder by activating both the surface of the backing layer of the specimen and the glass using plasma treatment in air for 1 min. The plasma treatment modified the surface chemicals

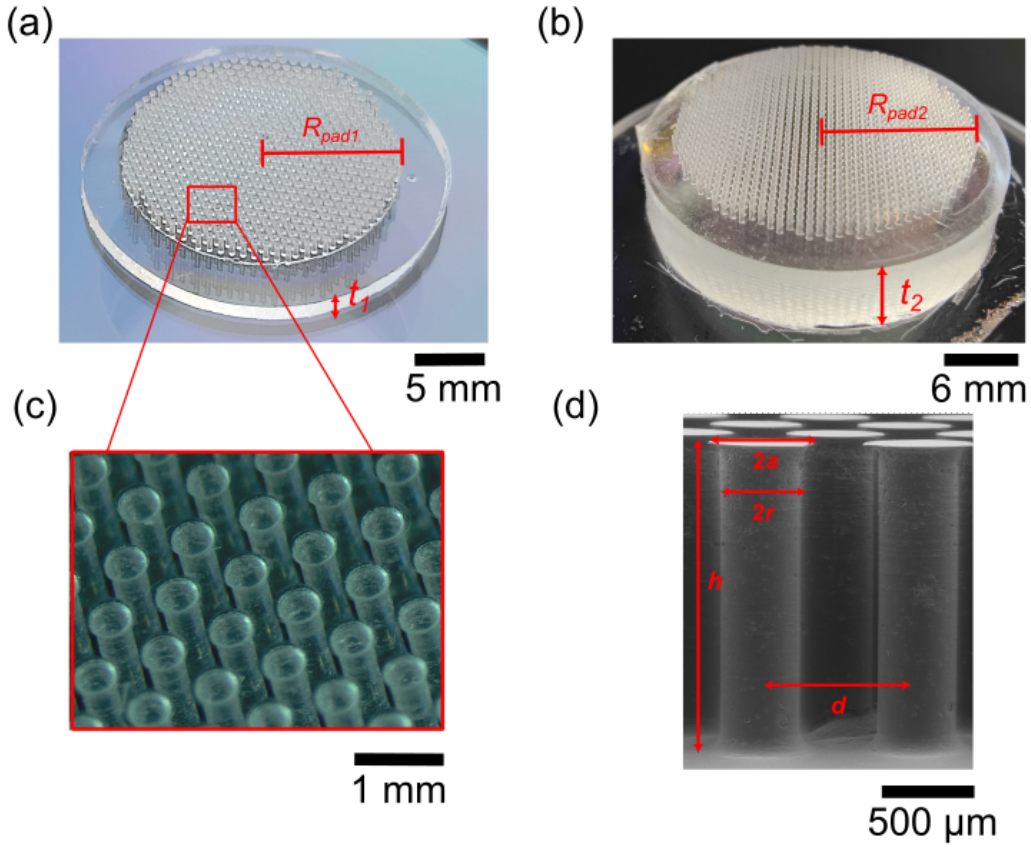

Figure 5.2: Mushroom-shaped fibrillar structures used with the optical devices. a) Specimen used for the precision setup, the inset **c)** shows the hexagonal arrangement. **b)** specimen used for the compact setup. The backing layer thicknesses are $t_1 = 1.5\,\text{mm}$ and $t_2 = 6.4\,\text{mm}$ for the two setups, the pad radii were $R_{pad1} = 10\,\text{mm}$ and $R_{pad2} = 12.5\,\text{mm}$. d) SEM of the mushroom-shaped fibrils. Typical fibril length is $h = 1600\,\mu\text{m}$, stalk radius $r = 200\,\mu\text{m}$, and mushroom tip radius $a \approx 300\,\mu\text{m}$. The center-to-center distance between adjacent fibrils is $d = 800\,\mu\text{m}$.

and allowed the PDMS to stick to the glass substrate. For the compact setup, the CR-39 curved holder was used to close the mold during the fabrication process. The cured PDMS bonded with the holder directly. The specimen for the precision setup was placed at the center of the holder. In the case of the compact setup, the curved holder moved slightly during curing resulting in a calculated 1 mm off-center position.

Flat aluminum surfaces were used as a target counter surface. The color and roughness of the target surface were varied by using different types of powder paints. The resulting surfaces in blue, red, and green had a smooth texture. In contrast, surfaces red.R, and blue.R were rough. Roughness measurements are presented in **Figure C1** and **Table C1** in the supporting information, SI.

5.3.3 Contact observation and image analysis

In order to apprehend the effect of light and camera settings on the contrast of the obtained contact signature, images before and in contact between the fibrillar structure and the target surface were captured and analyzed. For the light settings five different light colors were tested (blue, red, green, white, and yellow) and four light intensity levels (noted as INT1 to INT4, with 4 the highest intensity). For the camera settings, three levels of exposure and two of the gain were analyzed. As the two setups require different parameters to function properly, light intensity levels and camera settings were chosen differently (in a range going from very dark to very bright images).

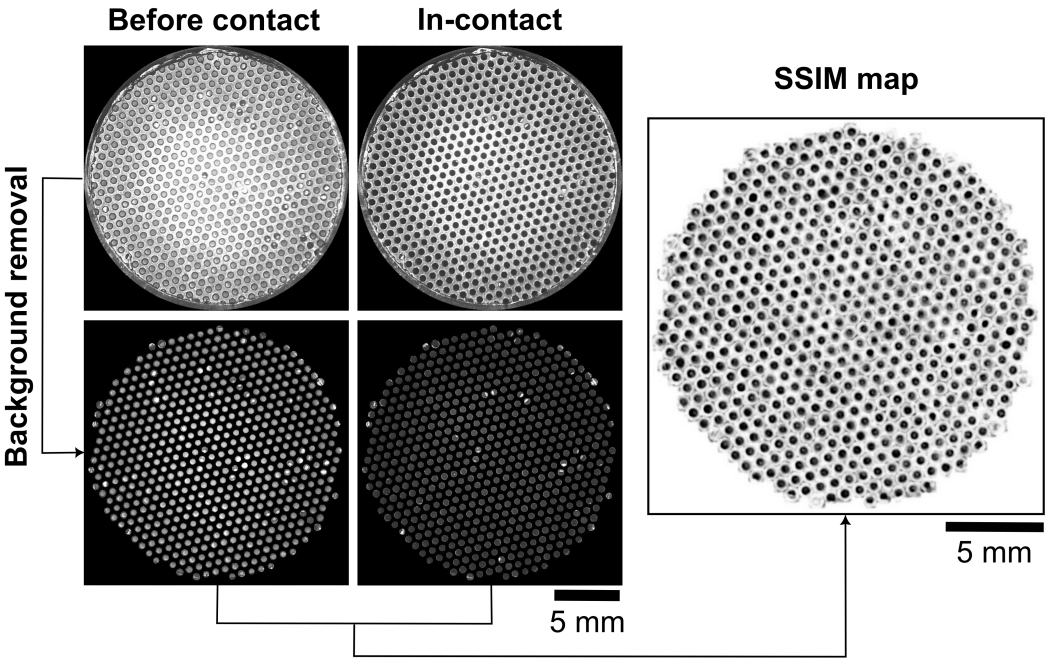

Figure 5.3: Image processing steps. First, the background was removed from the original images (lower row). Then, a local structural similarity index (SSIM) map (right) was obtained comparing pixel by pixel between the image in contact and before contact (The presented images were obtained using the precision setup).

The collected images were analyzed using the Image processing toolbox from MATLAB (MathWorks, MA, USA). The background of the images was removed to reduce the noise and allow a comparison based only on the contact regions. For this purpose, a mask was created from one image in the same batch and subtracted from the rest of the images. The images before contact and in contact were then compared using the structural similarity index measure, SSIM [177]. Initially developed to assess perceptual image quality, it can be used as a metric to measure the similarity between two given images. The SSIM of two given

images x and y, is given by **Eq.5.1**:

$$SSIM(x,y) = \frac{(2\mu_x\mu_y + c_1)(2\sigma_{xy} + c_2)}{(\mu_x^2 + \mu_y^2 + c_1)(\sigma_x^2 + \sigma_y^2 + c_2)} \tag{5.1}$$

with μ_x the average of x, μ_y the average of y, σ_x^2 the variance of x, σ_y^2 the variance of y, and σ_{xy}^2 the covariance of x and y. c_1 and c_2 are two variables to stabilize the division with weak denominator (i.e. If either the averages or the variances of both x and y were zero, the division would fail).

Global and local SSIM values were calculated for the image and for each pixel. The latter was used to create an SSIM map, see the example in **Figure 5.3**. SSIM values varied between -1 and 1: the value was 1 when the two pixels or images compared before and in contact were identical, and -1 when they were completely different. Small values of the local SSIM appear as dark pixels in the SSIM map and large values as bright pixels.

Visual features: number of fibrils in contact, N_a, and misalignment vector, $\vec{v}$ (i.e., the difference between the center of mass of the full contact and the center of mass of the partial contact in the case of misalignment) were extracted from the image of the contact signature using Computer Vision and Image Processing toolboxes from MATLAB as was previously reported in [171].

5.4 Results and discussion

The two optical devices were successfully used to collect images of the contact signature of the micropatterned structures on different target surfaces under various light and camera settings.

For illustration, **Figure 5.4** shows images of the fibrillar structure in contact with a rough blue surface under red illumination as an example (a comparison of all the light settings used is going to be presented further in **Figure 5.8**). A close-up of the structure in each case is also shown before contact for comparison.

The precision setup offers a perpendicular view from the top on each fibril even at off-center positions, whereas the simpler design of the compact setup leads to an oblique angle of incidence, such that parts of the side wall can be seen as well. Note that there is some reflection from the tips of the fibrils as well as from the base plane (i.e. the bottom plane of the fibrils), **Figure 5.4 b**. The reflections from the side wall are less visible in the upper region of the contact image (see **Figure C2** in SI for a close-up look of this region). In the compact setup, this can be readily explained by the light incident from many different directions, such that there will always be some light paths leading to the camera. The difference between the contrast in the upper and bottom region could be

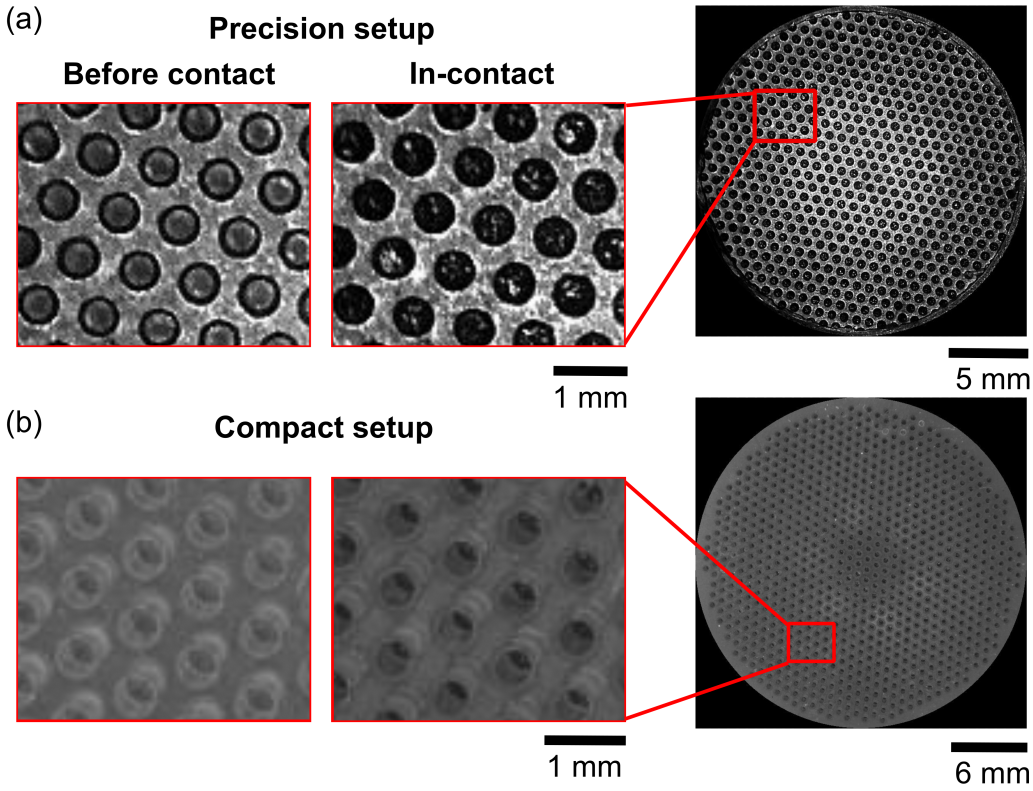

Figure 5.4: Example contact images of the fibrillar array in contact with a rough blue surface. The insets are zoomed-in images of the selected area for **a)** the precision setup and **b)** the compact setup. The close-up images in both case present also images before contact for comparison. Red illumination was used for these images.

related to the position of the specimen in comparison to the concave glass holder (i.e., the specimen is positioned at $\approx$ 1 mm off-center). In contrast, precision setup is a dark field optical system, so the observed reflections can be related to the unevenness of the micropatterned structure surfaces (i.e., the tip of the fibrils and the base plane). The granular appearance of the reflections supports that assumption. Moreover, the distribution of the light reflected from the tips of the fibrils changes drastically upon contact in the precision setup, which indicates a deformation by the rough surface of the target. This is less visible in the compact setup. The main change from the before-contact to the contact state, however, is a significant reduction of the light reflected from the tips of the fibrils. This is due to frustration of the Fresnel reflection upon contact, and absorption of the light in the colored target surface.

The observation of the interface through the whole cross-section of the fibril in the precision setup maximizes the contrast variation between fibrils before and in contact. The compact setup also achieves a significant contrast variation even under oblique observation, most likely because the light reaching the camera from the side wall of the fibril has also gone through a reflection at the tip before.

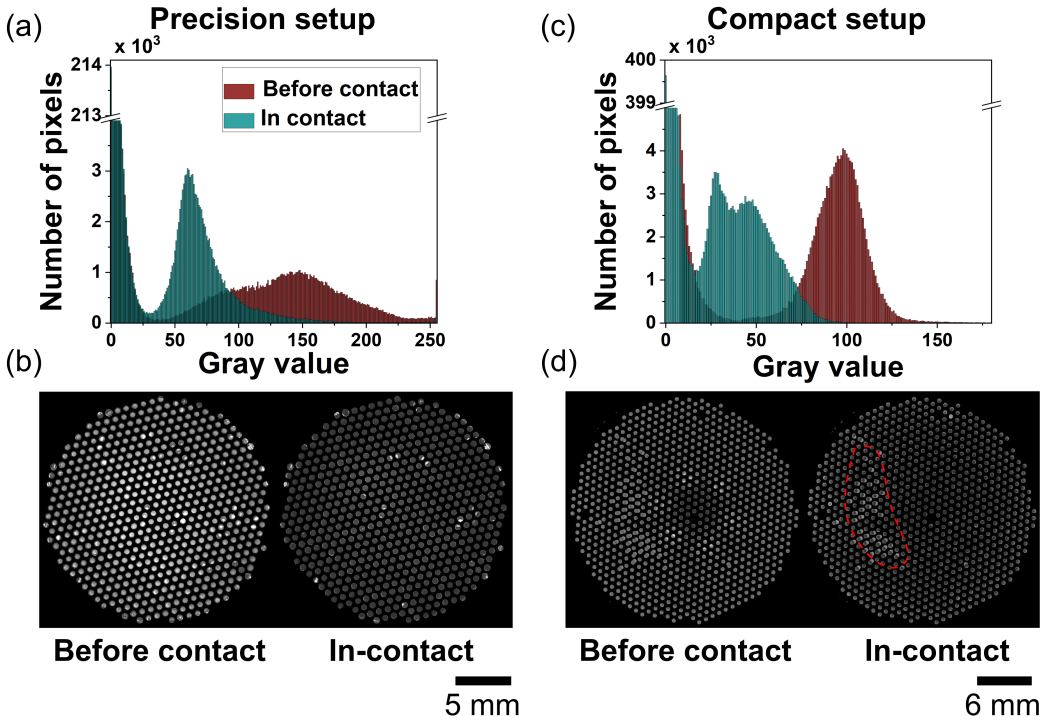

Figure 5.5: Images and the corresponding gray value histogram for a red surface with green light and intensity 4. a,b) using precision setup. **c,d)** using the compact setup.

Figure 5.5 presents images before and after contact for the precision and compact setups (after background removal) and the corresponding gray value histogram using green light. The first peaks from 0 to 25 correspond to the dark background. For both setups, the second peaks shift to a darker tone as the fibrillar structure goes into contact. The highest peak for set-up 1 is about 150 before contact and about 60 in contact, **Figure 5.5 a**. For the compact setup, the peak changes from around 100 to two peaks between 25 and 50, **Figure 5.5 c**. Note that some fibrils in the contact signature obtained using the precision setup appear to be brighter than the rest of the fibrils, **Figure 5.5 b**. These fibrils are either defected, slightly tilted, or partially in contact. The defected areas lead to the scattering of the light and to a brighter contrast as explained previously in section 2.1. For the compact setup, one can distinguish two levels of the gray values on the same fibril for some fibrils, see the dashed area in **Figure 5.5 d**. This effect is due to reflections from the side wall of the fibrils in the compact setup that interfered with the mask creation for background removal.

Figure 5.6 a shows contact signature images collected using the precision setup of the patterned structure in contact with a red surface illuminated using green light for this example. **Figure 5.6 b** present the corresponding SSIM map and SSIM value depending on the variation of the camera settings. Similar analysis for images obtained using the compact setup is presented in **Figure C3**

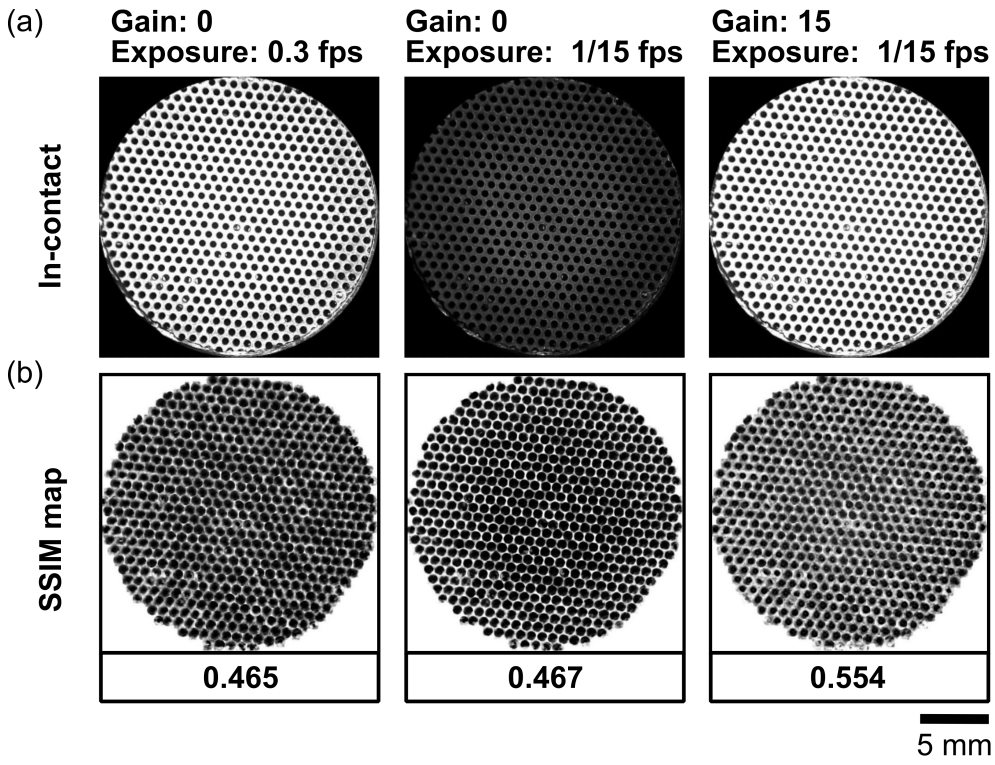

Figure 5.6: Camera setting variations in terms of the exposure time and the gain for the precision setup. a) The original images and **b)** the SSIM map and the SSIM global value (in the box). A red surface as a target surface was illuminated with green light at intensity level 4.

in SI. Looking at the original images it is easier to detect the contact signature of the fibrils as the exposure time or the gain is increased, for both setups. This is due to the change in the brightness of the background pixels. However, after removing the background and comparing the before and in-contact images, the SSIM values and SSIM map show a negligible difference between the various camera settings.

Figure 5.7 displays SSIM maps and global values as a function of 4 different light intensities (INT1- INT4). Original images used to calculate the SSIM map and global values are presented in **Figure C4** in the SI. For the precision setup increasing the light intensity decreased the SSIM value and increased the obtained contrast until saturation. For the compact setup, the variation of the SSIM values and contrast with the increase of the intensity is small. In theory, the light intensity is just a scaling factor for the information contained in the images, i.e., the increase of the intensity should increase the brightness of all pixels equally. Thus, it should not affect the extracted data (as can be seen for the compact setup, **Figure 5.7 b**). However, random fluctuations, quantization noise, and the saturation of bright pixels can be the reason for the higher variability observed in the precision setup, **Figure 5.7 a**. The smaller variation in the compact setup

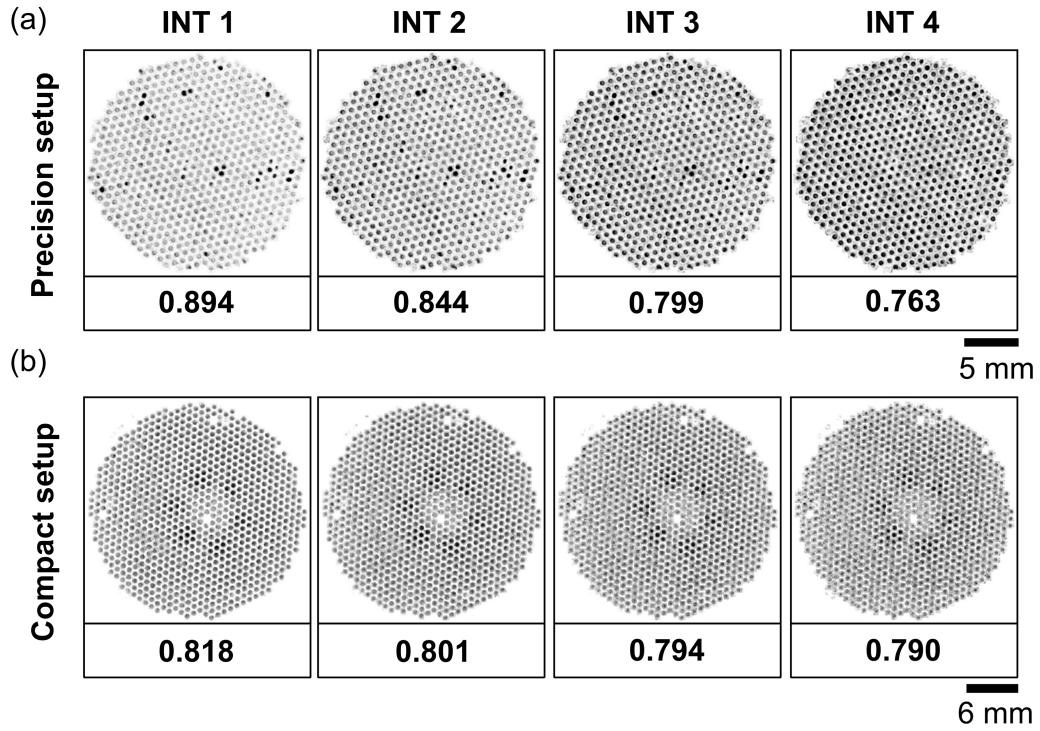

Figure 5.7: SSIM map and SSIM global value depending on the light intensity for a red target surface using green light for **a)** the precision setup and **b)** the compact setup

can be attributed to its lower dynamic range, which makes it less sensitive to light intensity and exposure. In contrast, the dynamic range of the precision setup is too high, resulting in a dependence on the light intensity.

A particular effect of this intensity dependence can be seen in the darker fibrils in the SSIM map observed for INT1. These present fibrils that either have a defect, are slightly tilted or are partially in contact. When the light intensity is increased, the difference in the local SSIM values between these fibrils and the rest of the pad is less pronounced. As mentioned before, these fibrils result in bright pixels in the original images due to the scattering of the light. The bright pixels in this example are observed in images before contact. As the fibrils go into contact the scattering is slightly reduced. Hence, for INT1 as the brightness is low in the image before contact, the difference between these fibrils and the rest of the pad is quite prominent. As we increase the intensity, the brightness of the pixels of all fibrils before contact increases and reaches saturation for INT4. In this case, the difference between the defected fibrils and the rest of the pad is less noticeable.

Figure 5.8 represents values of the global SSIM in the form of a heat map where bright colors present a low contrast, i.e., high SSIM values and dark colors present higher contrast, i.e., low SSIM values. SSIM global values for the precision setup range between 0.59 and 1 depending on the light color and intensity, while

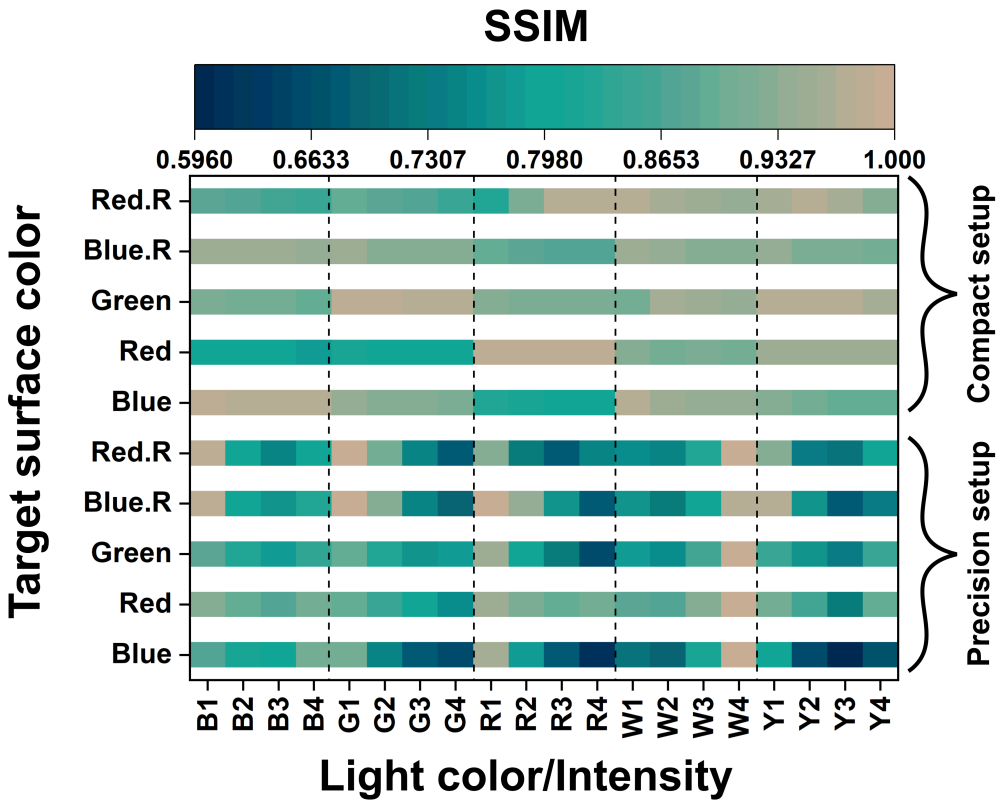

Figure 5.8: SSIM heat map showing the contrast variation between the precision setup and the compact setup for the different target surface colors, light colors (B: blue, G: green, R: Red, W: white, Y: yellow light) and light intensity (level 1, 2, 3, and 4). A dark blue-green field in the map (low SSIM value) indicates that the respective combination of colors and light intensity produces high contrast between the images before and in contact. These conditions are more suitable for detecting the contact than the low contrast (high SSIM) combinations marked in the map by bright reddish hues.

for the compact setup it ranges between 0.785 and 1. The ability of the precision setup to reach lower SSIM values shows that the contrast in the precision setup with the proper light parameters can be better than the compact setup. This can be due to the inhomogeneity and the scattering of the light in the compact setup which reduces the contrast in different areas of the fibrillar structure.

As mentioned before, the intensity of the light has a higher effect on the precision setup. As can be seen in **Figure 5.8** for the precision setup, intensity level 4 generates the best contrast when green or red light is used whereas the contrast deteriorates when using white, yellow, and blue light. However, in all cases, intensity level 1 exhibits the highest SSIM values and therefore the lowest contrast. We can deduce that the saturation of the pixels is dependent on the color of light used.

For both devices, target surfaces with the same color as the light used result in

higher SSIM values and therefore a lower contrast, for example, the blue light with a blue surface (SSIM=0.91 for the precision setup intensity 4). Whereas when choosing a different color of the light the contrast is enhanced, for example blue surface with red light (SSIM=0.62 for the precision setup intensity 4). Overall, the contrast for both setups is dependent on the right choice of the light color with the corresponding color of the target surface. In fact, if the light color is similar to the target surface color, the reflections from the target surface in contact may just replace the reflection from the fibril tip out of contact. Thus, the difference in the contrast, in this case, is very minimal.

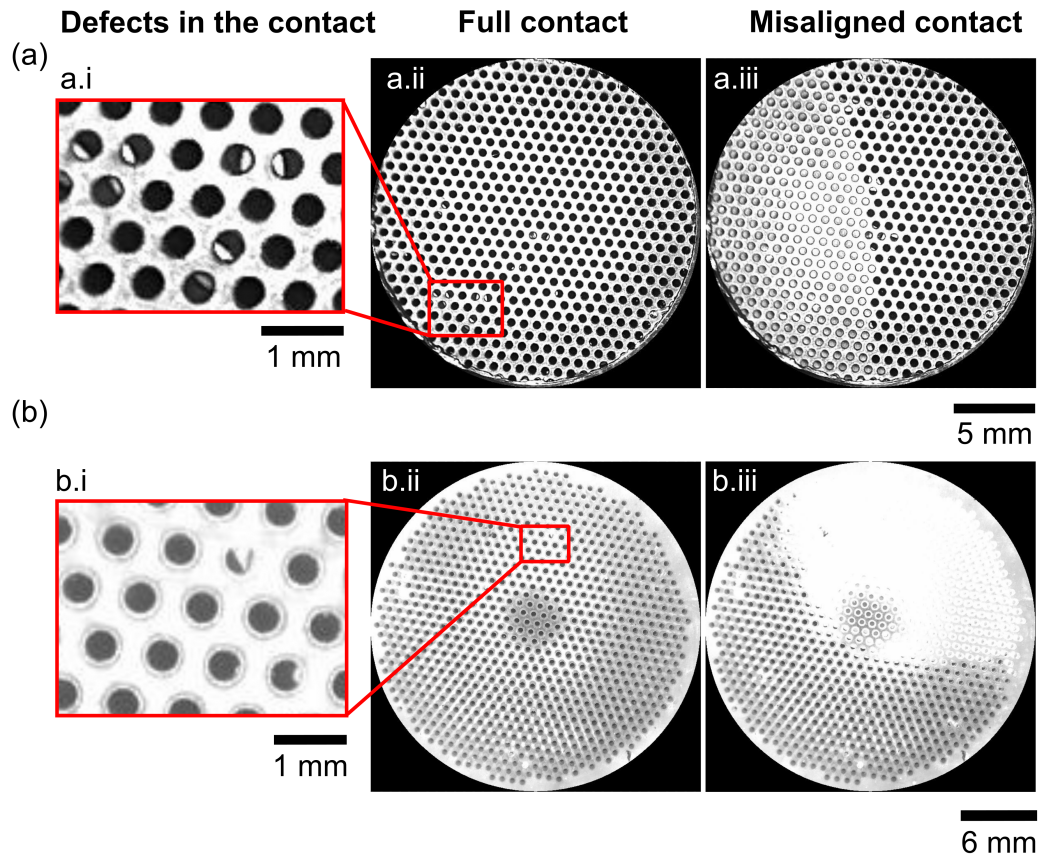

Figure 5.9: Contact signature (unprocessed images) of the fibrillar structure showing full contact (**ii**), misalignment of the fibrillar array with the target surface (**iii**) and defects in the contact interface (**i**) at the fibrils level for **a)** the precision setup and **b)** the compact setup, respectively.

Figure 5.9 highlights conceivable applications of the novel setups to detect anomalies in the contact. Using these new optical devices, some defects at fibrils interface (**Figure 5.9 a.i** and **b.i**) or even roughness (**Figure 5.4 a** and **b**) are also visible for both setups. Based on statistical evaluation, it should be possible to distinguish between roughness affecting all fibrils in contact in a similar way and defects present in a small proportion of fibrils only. However, it should be mentioned that it is not always easy to characterize the type of a defect. Com-

paring the two setups, the task of analyzing the contact at the level of individual fibrils is probably simpler in the precision setup, since all fibrils are seen from the same perpendicular angle of incidence.

Furthermore, we are able to detect alignment imperfections with both setups, as can be seen in **Figure 5.9 a.iii** and **b.iii**. Without any image processing, the fibrils that are in contact (black for the precision setup and dark gray for setup2) are clearly distinguishable from the ones that are detached due to misalignment. Further image processing allows the extraction of visual features that can be used for different applications. **Figure 5.10** presents examples of the visual features that can be extracted from the contact signature. Although the number of fibrils and the misalignment vector can be extracted accurately, the real contact is still difficult to obtain due to the different reflections at the fibrils scale.

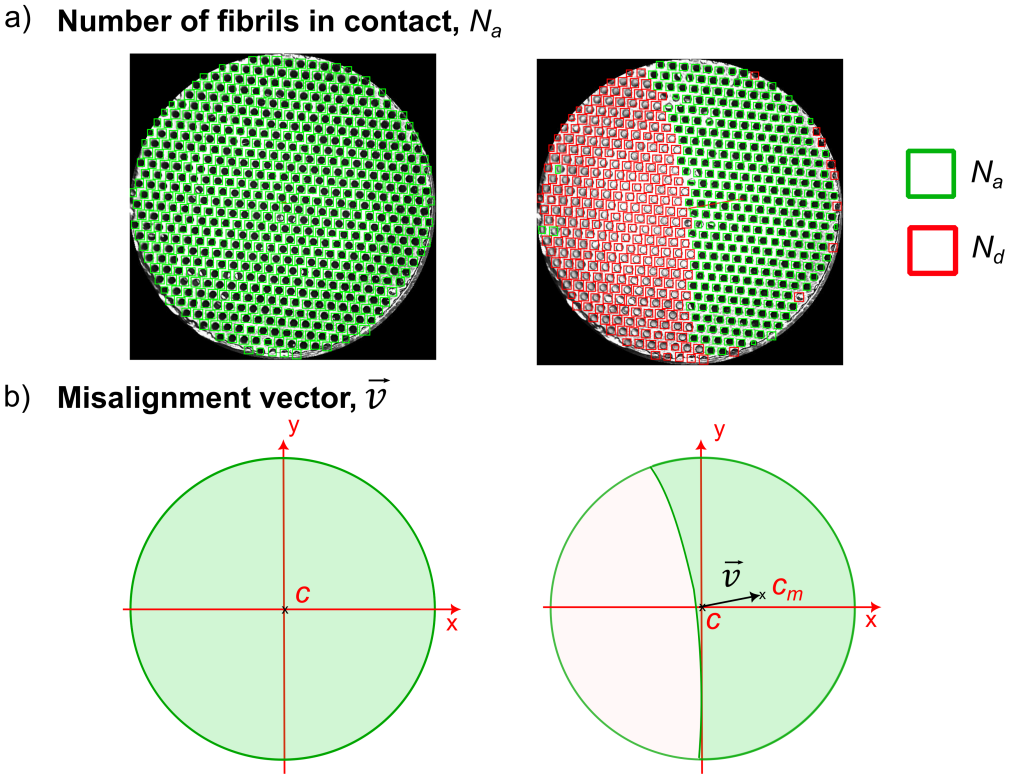

Figure 5.10: Extracted visual features. a) Number attached, N_a, and detached fibrils, N_d. **b)** Misalignment vector, $\vec{v}$, the vector between the center of the full contact, C and the centre of the misaligned contact, C_m.

5.5 Conclusions

For the observation of the contacts between fibrillar structures and target surfaces, novel optical systems were presented. The optical system should allow for a clear distinction between fibrils in contact with the target surface and fibrils out of contact. Ideally, the distinction should not depend on the position of the fibril in the array, i.e., the image quality should be the same for fibrils in the center region or at the edge of the array. Furthermore, the compactness of the device is an asset for practical applicability. In summary, the two setups met these requirements to different extents:

- The precision setup showed high contrast between before and in-contact. It allowed the detection of single fibril contact, roughness, and other possible contact imperfections such as misalignment and defects in the contact interface. However, this device is bulky with a total length of 40 cm.
- To reduce the size, a different approach was taken to build the compact setup. This setup is also cost-saving avoiding the use of expensive optics. However, the homogeneity of the light and the reflections are still a problem for this device.
- Light intensity had more effect on the precision setup. However, both devices were not affected by the camera settings.
- For both setups, the choice of the light color depending on the object can enhance the contrast of the obtained image.

The two setups open a wide range of applications for monitoring the correct attachment, the deterioration of the quality of the fibrillar structures as well as the detection of contamination at the interface. Nevertheless, further improvements on both devices to avoid reflections and enhance the homogeneity of the lighting would increase the imaging quality and pave the way for new applications.

Supporting information: chapter 5

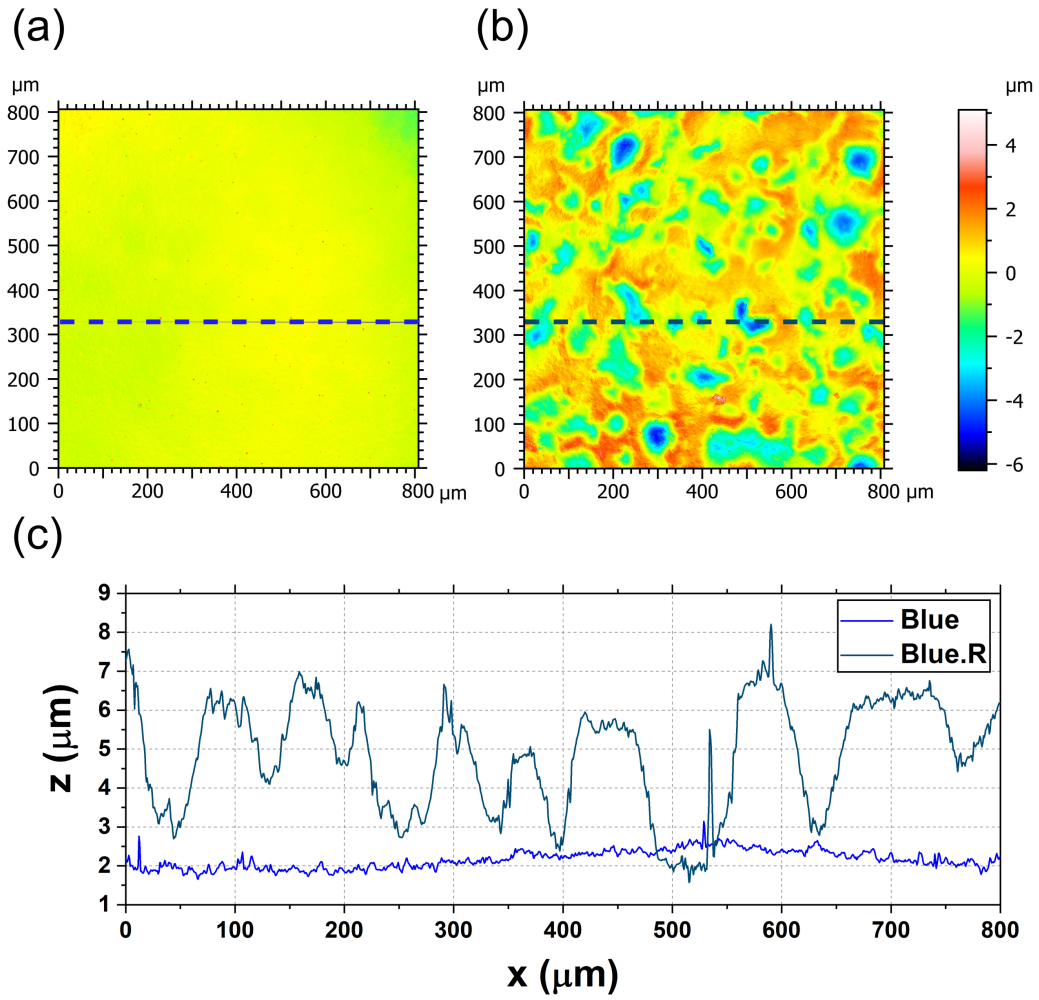

Figure C1: Confocal microscope topography images for **a)** Blue and **b)** Blue.R surfaces. The dashed lines represent the extracted profiles. **c)** The two extracted profiles.

Table C1: Roughness of the target surfaces

Surface	Rz (µm)
Red	0.43
Red.R	1.92
Blue	0.615
Blue.R	2.07
green	0.44

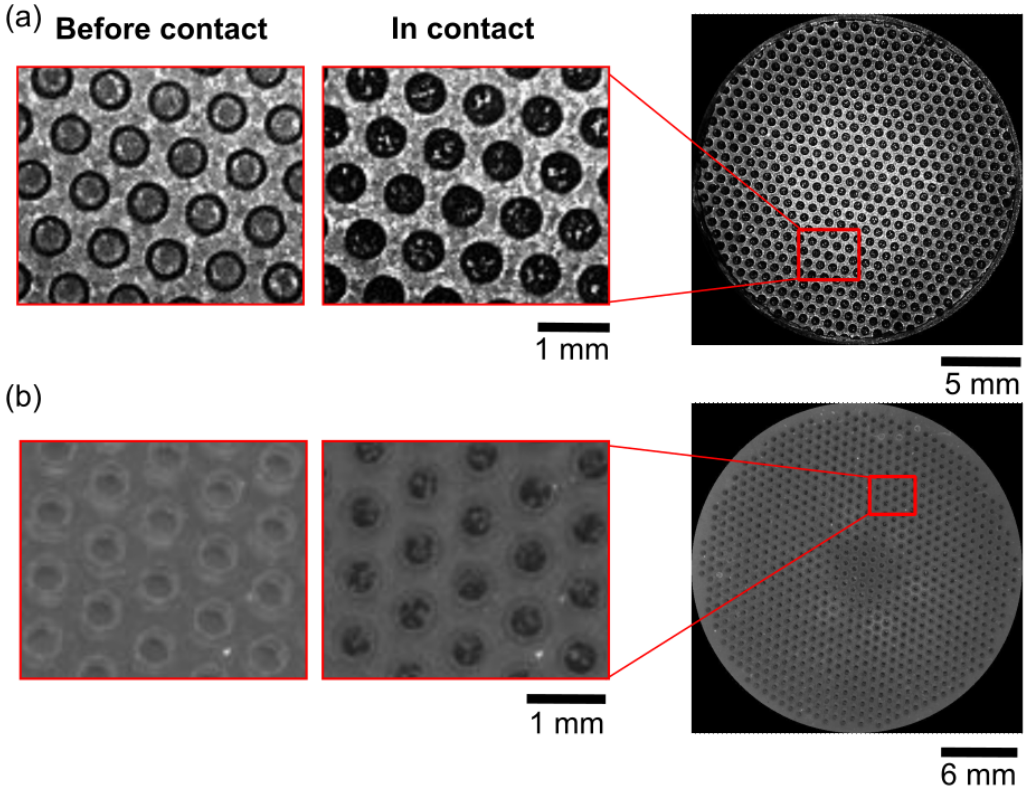

Figure C2: Original images before and in contact of the fibrillar array with a rough blue surface. The insets are zoomed in images of the selected area for **a)** setup 1 and **b)** setup 2. red illumination was used for these images.

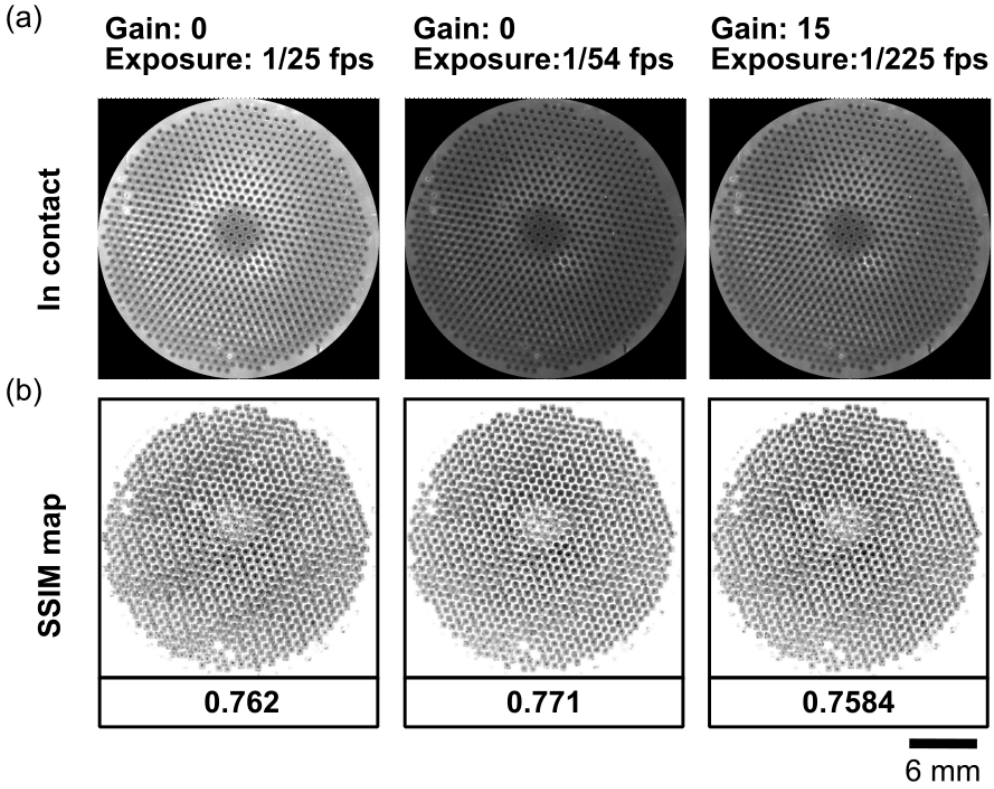

Figure C3: Camera setting variations in terms of the exposure time and the gain for setup 2. a) the original images and **b)** the SSIM map and SSIM global value. A red surface was used as a target surface with a green light and an intensity level 4.

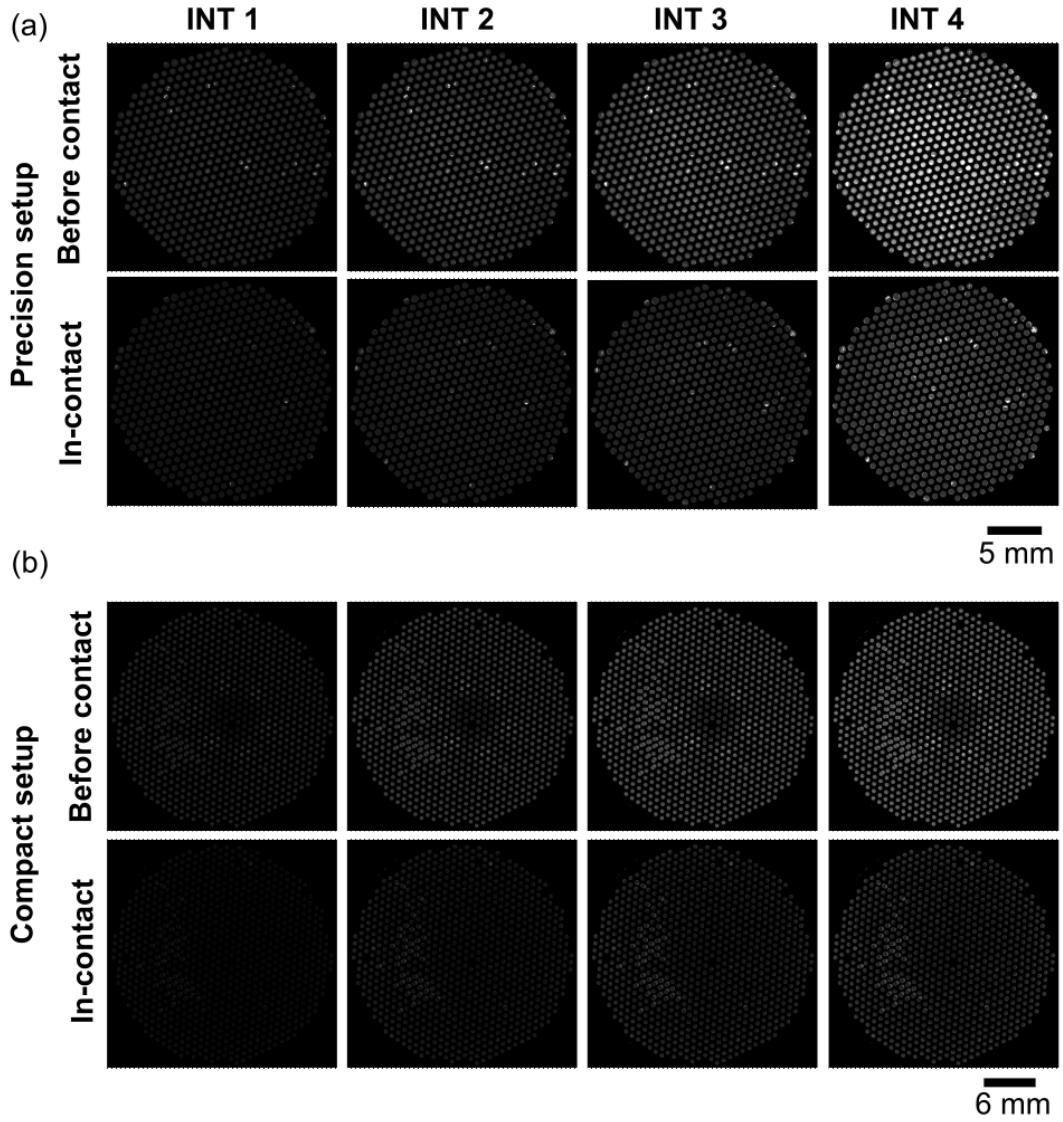

Figure C4: Original images with removed background before and in contact used to calculate SSIM values and SSIM map depending on the light intensity (in **Figure 5.7**) for **a)** the precision setup and **b)** the compact setup

Chapter 6

Adhesion hysteresis of a nominally flat punch with small-scale, single-wavelength roughness: A combined numerical and experimental study*

6.1 Abstract

Viscoelasticity is well known to cause a significant hysteresis of crack closure and opening when an elastomer is brought in and out of contact with a flat, rigid counterface. In contrast, the idea that adhesive hysteresis can also result under quasi-static driving due to small-scale, elastic multistability is relatively new. Here, we study a system in which both mechanisms act concurrently. Specifically, we compare the simulated and experimentally measured time evolution of the interfacial force and the real contact area between a soft elastomer and a rigid, flat punch, to which small-scale, single-sinusoidal roughness is added. To this end, we further the Green's function molecular dynamics method and extend recently developed imaging techniques to elucidate the rate- and preload-dependence of the pull-off process. Our results reveal that hysteresis is much enhanced when the saddle points of the topography come into contact, which, however, is impeded by viscoelastic forces. A similar interplay of viscous- and multistability effects is expected to occur in macroscopic polymer contacts and be relevant, e.g., for pressure-sensitive adhesives and modern adhesive gripping devices.

*This chapter is a planned publication.
Authors: Müller, C., Samri, M., Hensel, R., Arzt, E., & Müser, M.
See more information in the "Contribution of co-authors"

6.2 Introduction

Bringing two surfaces into contact and separating them again is generally associated with a net, rate-dependent energy loss. Several processes can cause this hysteresis, in particular, physicochemical interfacial aging [178, 179], such as chain interdigitation in polymer-polymer contacts [180], viscoelastic relaxation in the vicinity of and far from true contact [181–184], and the formation of capillaries [185–187], to name a few. Recently, elastic multistability [188] has also received increased attention as a potential adhesive dissipation mechanism occurring during the relative motion of nominally flat surfaces, i.e., the discontinuous jump of small-scale asperities in and out of contact [30, 189–193] during quasi-static motion, or the discontinuous motion of a contact line during approach and retraction resulting from chemical or structural surface heterogeneity [194].

Ascertaining what adhesion-hysteresis mechanism dominates under what circumstances is a difficult task, because analytical solutions for the rate- and/or the preload dependence of the pull-off force scarcely exist, even when only one relaxation process dominates. Moreover, it is certainly conceivable that competing mechanisms, e.g., contact aging and contact growth, lead to a similar, for example, logarithmic time dependence of waiting time on the pull-off force. The validity of models and theories, irrespective of whether they are solved analytically or numerically, should therefore be tested against information additional to load-displacement relations and their dependence on rate, waiting time, and preload. A central quantity to be known is the time evolution of true contact, including its size and shape.

While small-scale features of adhesive experimental and *in-silico* contacts have been successfully compared in the recent past, such as in the contact-mechanics challenge [195, 196] or to demonstrate the breakdown of Amontons' law at the small scale in soft-matter contacts [197], we are not aware of related studies involving time-dependent phenomena as they occur during adhesion hysteresis.

The central difficulty for simulators lies in the short-range nature of adhesion, whose range of interaction ρ critically affects not only the viscoelastic losses caused by propagating cracks [198] but also the energy hysteresis induced by elastic instabilities [30, 199]. Unfortunately, using realistically small values for ρ requires extremely fine discretization to be used so that lattice instabilities are avoided [30]. The latter would lead to Coulomb friction for propagating cracks rather than to the more realistic polynomial crack-speed dependence [200, 201]. As of now, it does not seem to be clear how to reproduce reliably realistic dynamics of viscoelastic adhesion theory with continuum-theory based simulations.

In this work, we study the contact between a viscoelastic film and a nominally

flat, cylindrical punch to which single-wavelength, small-scale roughness is added. Depending on the relative orientation of different wavevectors $\mathbf{q}$, which all have the same magnitude q, different patterns can be produced for which the local height maxima form either a hexagonal or a triangular lattice. The questions to be addressed in this study are manifold. Can simulations reproduce experimentally observed dependencies, such as the normal force as a function of time and the concomitant contact-area evolution? How does the unit of time, or retraction velocity, have to be renormalized for a successful comparison between simulation and experiment when it is computationally unfeasible to work with realistically small values of ρ? Is it possible to clearly discriminate between dissipation due to elastic instabilities and viscoelastic crack propagation? And last but not least, can visualizing the contact area aid the prediction of pull-off forces?

6.3 Models and methods

6.3.1 Reference model

In this work, we compare simulations and experiments mimicking an ideal (mathematical) reference model, which is sketched in **Figure 6.1**. It consists of a flat, cylindrical, perfectly rigid punch of radius a to which single-wavelength corrugation $z(x, y)$ is added. The punch is indented into a homogeneous, isotropic, and elastomeric film with linear viscoelasticity. Inspired by the experimental realization, we will call this material PDMS, although the theoretical model does not necessarily imply a specific polymer compound. It has a finite height h, infinite in-plane dimension with a frequency-dependent Young's modulus $E(\omega)$ and a constant Poisson's ratio ν. Film and punch interact through a cohesive-zone model, which is characterized by a surface energy per unit area γ and a small but finite interaction range ρ. Punch and elastomer are frictionless and cannot interpenetrate.

Numerical values of the reference model are $a = 375\,\mu\text{m}$, $h = 2\,\text{mm}$, $E(0) = 2\,\text{MPa}$, $E(\infty) = 2\,\text{GPa}$, $\nu = 0.495$, and $\gamma = 50\,\text{mJ/m}^2$, which are admittedly our best guesses for the values of the laboratory version of the reference model. The precise frequency dependence of $E(\omega)$ as well as the interaction range cannot be well matched between the laboratory and the *in-silico* realization of the reference model, which is why we abstain from defining reference values here. The experimental range of adhesion can certainly be classified as short-ranged, while that used in the simulations is merely as short-ranged as computationally feasible.

Two different height topographies are added to the punch, a triangular (tri) and a hexagonal (hex) one. Redefining prefactors compared to previous work [202],

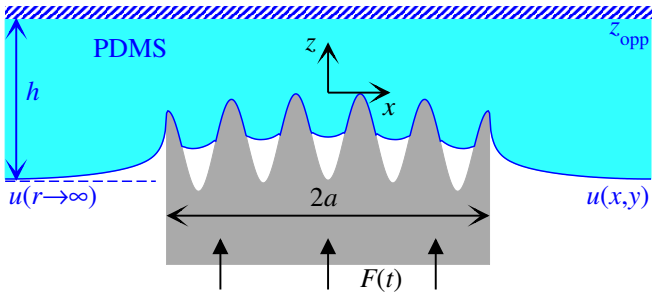

Figure 6.1: Illustration of the reference system. Dimensions are not to scale. However, $u(x, y)$ and the indenter shape represent data obtained from the simulation during compression and also the thermal shrinkage occurring after 3D printing.

they are given by

$$\frac{z_{\text{hex}}(x, y - \lambda/2)}{z_0(\text{hex})} = \frac{4}{9}\left\{\frac{3}{2} + 2\cos\left(\frac{\sqrt{3}}{2}qx\right)\cos\left(\frac{1}{2}qy\right) + \cos\left(qy\right)\right\} \tag{6.1a}$$

$$\frac{z_{\text{tri}}(x, y)}{z_0(\text{tri})} = 2 - \frac{z_{\text{hex}}(x, y)}{z_0(\text{hex})}, \tag{6.1b}$$

where $q = 2\pi/\lambda$ is the wave vector and $\lambda = 150\,\mu\text{m}$. The amplitude of the undulations—defined as half the difference between maximum and minimum—are set to $z_0(\text{hex}) = 9.2\,\mu\text{m}$ and $z_0(\text{tri}) = 4\,\mu\text{m}$.

Resulting punch profiles are shown in **Figure 6.2**. Different amplitudes were chosen, because the jump into contact of saddle points occurs much earlier for hexagonal than for triangular corrugations [202]. Moreover, the dimensionless surface energy $\tilde{\gamma} \equiv \gamma/v_{\text{ela}}^{\text{full}}$, where $v_{\text{ela}}^{\text{full}}$ is the areal elastic energy in full static contact, are approximately $\tilde{\gamma}(\text{tri}) \approx 0.32$ and $\tilde{\gamma}(\text{hex}) \approx 0.065$. These values are less than 1/2, which has been identified as the (approximate) dividing line between sticky and non-sticky for many surfaces with a symmetric height distribution [203].

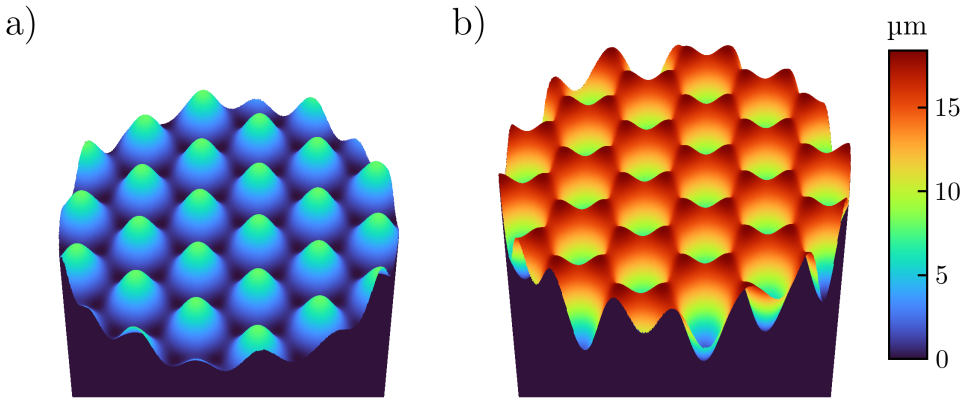

Figure 6.2: Top view of the flat indenter with **a)** triangular and **b)** hexagonal waviness.

The indenter is moved from non-contact at different constant velocities v_{ext} ranging from 0.5 to 25 µm s^{-1} into the elastomer until a target preload, F_{pl}, is reached. The velocity is then reverted quasi-instantaneously to initiate detachment. The preload is varied between 1 and 10 mN for the hexagonal and between 10 and 80 mN for the triangular surface.

A brief note on the choice of the frequency- and wavenumber-independent Poisson's ratio is in order. Real elastomers deviate from ideal incompressibility at high frequency much more than at low frequency, i.e., their Poisson's ratio falls from just below 0.5 at $\omega \to 0$ to typically around 0.3 for large ω [204, 205]. In the present study, we can ignore this effect, because the film thickness clearly exceeds the punch radius, which means that all relevant modes, other than the center-of-mass mode, can be treated as if the film was semi-infinite. In this case, the contact modulus, $E^*(\omega) = E(\omega)/\{1-\nu^2(\omega)\}$, which is not very sensitive to the frequency dependence of the Poisson's ratio, becomes the central elastic parameter determining the viscoelastic response.

6.3.2 Numerical model and methods

The solution of the dynamics defined implicitly in section **6.3.1** requires some idealizations to be given up, while other specifications can be perfectly realized, at least to numerical precision. The latter include linear elasticity, the topographies, velocities, loads, and any other specified number. Compromises are related to the numerical solution of the problem, which includes the necessity to discretize space and time as well as the use of periodic boundary conditions for reasons of efficiency.

6.3.2.1 Reproducing viscoelastic properties using GFMD

The time evolution of the elastic bottom layer can be cast as

$$\tilde{u}(\mathbf{q},t) = \int_{-\infty}^{t} \mathrm{d}t'\, \tilde{G}(q,t-t')\, \tilde{f}(\mathbf{q},t'), \tag{6.2}$$

where $\tilde{u}(q,t)$ is the spatial Fourier transform of the displacement field as a function of time t, $\tilde{f}(q,t)$ is the spatial Fourier transform of the external force per unit area acting on the elastomer, and $\tilde{G}(q,t-t')$ is the Green's function conveying the effect that this force, or stress, at time $t' \leq t$ has on the displacement at time

t. Formally, $\tilde{G}(q,t)$ is given by

$$\tilde{G}(q,t) = \frac{2}{q}\int_{-\infty}^{\infty} \mathrm{d}\omega \frac{1}{E^*(\omega)} e^{i\omega t}. \tag{6.3}$$

The time dependence of the Green's functions $\tilde{G}(q,t)$ or the response functions they produce can be represented via Prony series, which in turn can be realized through rheological models, as that depicted in **Figure 6.3**, where stiffness (k_n) and damping (η_n) terms are introduced. An appropriate choice of weights $\kappa_n = k_n/k_0$ and relaxation times $\tau_n = \eta_n/k_n$ allow the target frequency dependence $\kappa(\omega) = E(\omega)/E(0)$ to be approximated through

$$\kappa(\omega) = 1 + \sum_{n=1}^{N} \kappa_n \left\{ \frac{\omega^2\tau_n^2}{1+\omega^2\tau_n^2} + i\frac{\omega\tau_n}{1+\omega^2\tau_n^2} \right\}. \tag{6.4}$$

An example of a system producing such a target dependence is shown in **Figure 6.4 a**.

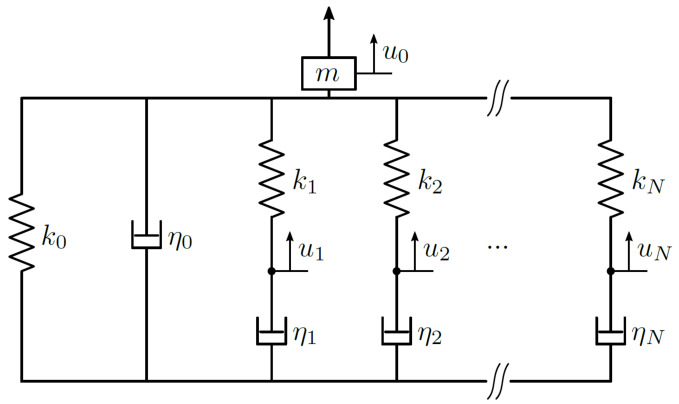

Figure 6.3: Illustration of the rheological model employed, which consists of one Kelvin-Voigt element (K_0,η_0) and N Maxwell elements (K_n,η_n) in parallel plus an inertial mass m. In GFMD, each mode $\tilde{u}(\mathbf{q})\widehat{=}u_0$ is represented with such a model.

An inertia m and damping η_0 were added to the rheological elements, which allowed us to implement the final rheological model into a Green's function molecular dynamics (GFMD) [94] based code. The two added elements alter the frequency dependence to

$$\kappa_{\mathrm{GMFD}}(\omega) = \kappa(\omega) - \omega^2\frac{m}{k_0} + i\omega\frac{\eta_0}{k_0}. \tag{6.5}$$

By replacing k_0 with $k_0(q) = qE^*/2$ for each $\tilde{u}(\mathbf{q},t)$, all k_n and η_n turn into $k_n(q)$ and $\eta_n(q)$, with the exception of $\eta_0(q)$, whose parametrization will be discussed separately.

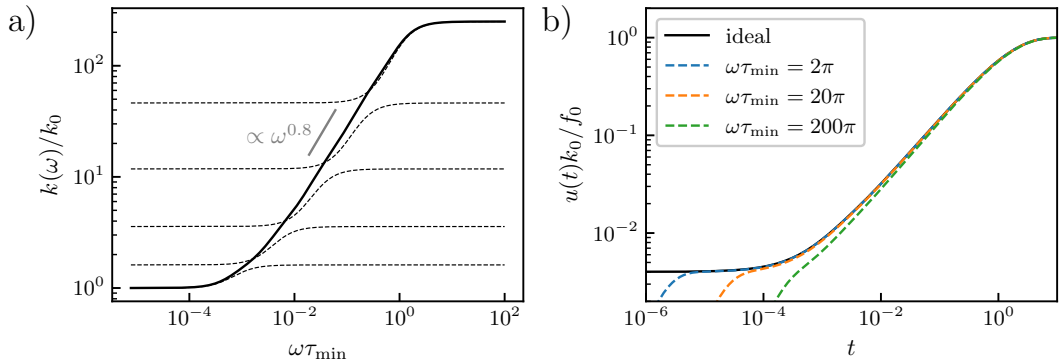

Figure 6.4: **a)** Frequency-dependent target stiffness $k(\omega)$ as a function of frequency ω using $k_{n+1} = 6^{0.8}k_n$, $\tau_{n+1} = \tau_n/6$, and $N = 5$. Dotted lines show the relaxation process of individual Maxwell elements and the gray line a $\omega^{0.8}$ power law. **b)** Associated response function $u(t)$ to a point force $f(t) = f_0\Theta(t)$ using different auxiliary masses leading to different eigenfrequencies $\omega_{\mathrm{GFMD}} = \sqrt{k_\infty/m}$. In each case, the auxiliary damping was chosen to satisfy the condition for critical damping $\eta_0 = 2\omega_{\mathrm{GFMD}}m$.

The resulting equations of motion for each mode and its associated extra degrees of freedom $u_n(\mathbf{q}, t)$ read:

$$m(q)\ddot{\tilde{u}}(\mathbf{q},t) + \eta_0(q)\dot{\tilde{u}}(\mathbf{q},t) + k_\infty(q)\tilde{u}(\mathbf{q},t) = \tilde{f}(\mathbf{q},t) + \sum_{n=1}^{N} k_n(q)u_n(\mathbf{q},t), \tag{6.6a}$$

$$\eta_n(q)\dot{u}_n(\mathbf{q},t) = k_n(q)\{\tilde{u}(\mathbf{q},t) - u_n(\mathbf{q},t)\}, \quad n \in 1...N, \tag{6.6b}$$

with $k_\infty(q) \equiv \sum_{n=0}^{N} k_n(q)$, which is nothing but $k_\infty(q) = E(\infty)k_0(q)/E(0)$, where only one of the two "arrays" $k_0(\mathbf{q})$ and $k_\infty(\mathbf{q})$ needs to be stored in memory. Even for a single Maxwell element, the solution of the equations of motion turned out simpler and more stable (but not necessarily faster) than our previous extension to GFMD [100], which was similar in spirit as that proposed by van Dokkum and Nicola [206] in that the first-order time derivatives of the external forces were needed. Our current approach rather resembles that pursued by Bugnicourt *et al.* [207], who used Zener instead of Maxwell models and a conjugate gradient (CG) minimization method for the solution of the instantaneous or high-frequency response instead of the auxiliary masses.

Before proceeding, a few additional notes of clarification might be in order. First, tildes on the $u_n(\mathbf{q}, t)$ are omitted, as they are not subjected to an inverse Fourier transform. Second, the equations of motion solved in conventional GFMD are recuperated by setting $N = 0$, while the standard linear solid is obtained when using $N = 1$ and (infinitesimally) small values for m and η_0. Third, the presented methodology is readily extended to more general situations, even if the above treatment merely targets the specialized problem defined in section **6.3**. For example, if the elastic properties were anisotropic in the xy-plane, as they would

be if the elastomer were prestrained in x but not in y direction, the coefficients $k_0(q)$ and thereby $k_n(q)$ and $\eta_n(q)$ would be functions of the vector $\mathbf{q}$ and not merely of its amplitude. Similarly, if the elastic properties changed with depth, as is the case when the crosslinking and thus the stiffness depends on the depth [208], but similarly when the elastomer is confined by a hard wall [95, 96], the term $k_0(q) = qE^*/2$ would have to be replaced or multiplied with an appropriate q-dependent function. Last but not least, using N Maxwell elements does not imply a single time step to take N times longer than a conventional GFMD time step, because the most demanding operation is the fast Fourier transform. For example, using $N = 5$ Maxwell elements per mode only increases the CPU time per time step by roughly 50%, compared to a regular GFMD time step for a discretization of $2,048 \times 2,048$. Relative costs on memory are clearly larger. The reason why we do not go beyond five Maxwell elements in this study is that almost four decades of relaxation times can be covered when choosing $\tau_{n+1} = \tau_n/6$, which requires the time step to be reduced dramatically assuming τ_1 to remain fixed. Going to even more decades would make us have to reduce the time step—as measured in real time.

While the values of $k_0(q)$ as well as of $k_n(q)$ and $\eta_n(q)$ for $n \geq 1$ are predetermined by κ_n, τ_n, and E^*, the remaining parameters $m(q)$ and $\eta_0(q)$ should be chosen such that they provide a compromise between accuracy and efficiency. The goal must be to find the high-frequency elastic response as quickly as possible, albeit without making it necessary to dramatically reduce the used time step Δt. Under the made assumption that $E(\omega)$ does not depend on q, each free surface mode must have the same response function. This implies $m(q) \propto k_0(q)$, which is the choice made in so-called mass-weighted GFMD [99]. The period associated with the resulting frequency $\omega_{\mathrm{GFMD}} = \sqrt{k_\infty(q)/m(q)}$ is best chosen such that it is not much less than $\tau_{\min} = \tau_N = \min(\tau_n)$. We found the "aggressive" choice of $\omega_{\mathrm{GFMD}}\tau_{\min} = 2\pi$ to be sufficient.

If, however, the pulling velocity is so large that the time step Δt is no longer limited by $\tau_{\min}$ but by a large pulling velocity, e.g., by the ratio of a characteristic height amplitude and the pulling velocity, we recommend to set m such that $\omega_{\mathrm{GFMD}}\Delta t \approx \pi/10$ as to achieve a numerically stable but fast relaxation of the high-frequency response to its exact solution. After realizing that the left-hand side of **Eq.6.6a** represents a damped harmonic oscillator, $\eta_0(q)$ is set to satisfy the condition for critical damping, i.e., $\eta_0(q) = 2\omega_{\mathrm{GFMD}}m(q)$.

As a consequence of the just-made choices, the target visco-elastic response, for example, to an indenter, exerting a force on a single (grid) point starting at time t_0, is mimicked quite accurately at times satisfying $t > t_0 + \tau_{\min}$, which can be achieved within one or two dozen time steps. The validity of this claim is

demonstrated in **Figure 6.4 b** for our default $N = 5$ Maxwell models containing default model. It can be seen that even $\omega_{\mathrm{GFMD}}\tau_{\min} = 2\pi$ leads to quite satisfactory results, although the time step, Δt was set by default to $\Delta t = \tau_{\min}/20$.

A final note related to the modeling of viscoelastic properties pertains to our simulations based on $N = 5$ Maxwell elements, which are shown in **Figure 6.4 b**. The rationale for why the ratio k_∞/k_0 was reduced from its reference value of 1,000 to 250 will be detailed in the results section. At this point it shall suffice to say that five Maxwell elements, in addition to the k_0 spring, can produce a response function $E'(\omega)$ that roughly scales proportional to ω^β with $\beta \approx 0.8$ at an intermediate frequency ω_{int} defined through $E'(\omega_{\mathrm{int}}) = \sqrt{E'(0)E'(\infty)}$, where $E'(\omega)$ is the storage modulus, i.e., the real part of the complex function $E(\omega)$. A single element yields $\beta \approx 2$, while experimental systems are close to $\beta \approx 0.5$.

6.3.2.2 Modeling adhesion

The adhesive and repulsive interaction between elastomer and indenter is modeled by the cohesive zone model (CZM) proposed in Ref. [30]. Assuming their two surfaces with nominal surface energy γ to have a gap $g(x, y)$, the interaction potential $\Gamma(g)$ is given by

$$\Gamma(g) = -\gamma \cdot \begin{cases} \{1 + \cos(\pi g/\rho)\}/2 & \text{for } 0 \le g < \rho \\ \{1 - (\pi g/\rho)^2/4\} & \text{for } g < 0 \\ 0 & \text{else} \end{cases}, \tag{6.7}$$

where ρ is the range of adhesion.

Our CZM allows two surfaces to overlap marginally but penalizes the overlap with a harmonic function. Enforcing a strict non-overlap constraint might be possible, albeit, only at a much enhanced numerical cost, since this would certainly require all internal modes $u_n(\mathbf{q})$ to be Fourier transformed. Moreover, the quadratic dependence of the potentials implies an upper bound for the stiffness of the equation to be solved, thereby ensuring stable integration with an appropriately chosen time step. The maximum adhesive stress $\sigma_{\mathrm{th}} = \max(\mathrm{d}\Gamma/\mathrm{d}g)$ that can locally occur using this model is $\gamma\pi/2\rho$.

The range of adhesion is generally chosen such that it is as small as possible for a given discretization but not so small that lattice pinning and subsequent instabilities of the grid points near a propagating crack would occur. This can be achieved when the maximum curvature of the potential is set to approximately $0.2 q_{\mathrm{ref}} E^*$, where $q_{\mathrm{ref}} \equiv 2\pi n/L$, n being the number of discretization points parallel to one spatial direction and L the linear dimension of the periodically repeated simulation cell [30]. Given a default choice of $L = 1.5\,\mathrm{mm}$ and discretizations of

the elastomer surface into grid points whose number ranged from $2,048 \times 2,048$ to $4,096 \times 4,096$, ρ turned out to lie in between 0.187 to 0.264 µm, which is not only much more than typical Lennard-Jones interaction ranges of 3 Å but also exceeds recent estimates [209], which were obtained from experimentally measured pull-off forces between ruby and diamond, by a little more than a factor of ten.

To meaningfully compare simulations and experiments, it is necessary to assess whether the adhesive interactions used in the model are short- or long-ranged. This can be done using a (generalized) Tabor parameter, which is defined as the ratio $\mu_\mathrm{T} = \rho_\mathrm{c}/\rho$, where ρ_c is a characteristic interaction range at which the cross-over from short- to long-ranged adhesion takes place. Assuming that γ/E^* and a characteristic radius R_c are the only two independent length scales that can be constructed from the model, the only possible dependence of μ_T on the two length scales is

$$\mu_\mathrm{T} = \frac{1}{\rho} R_\mathrm{c}^\beta \left(\frac{\gamma}{E^*}\right)^{1-\beta}, \tag{6.8}$$

assuming either a flat punch with radius R_c or an indenter whose shape is a power law in the radius, i.e., $h(r) = R_\mathrm{c}(r/R_\mathrm{c})^n/n$. It will be shown in a separate work that the exponent β turns out to be $\beta = (n-1)/(2n-1)$ so that $\beta = 1/3$ for a parabolic ($n = 2$) and $\beta = 1/2$ a flat-punch ($n \to \infty$) indenter. These two limiting cases agree with the definition of the conventional Tabor parameter for a parabolic indenter [210] and for the parameter allowing one to assess if the high-velocity retraction of a flat-punch indenter fails through crack propagation or through uniform bond breaking. They happen in the limits of $\mu_\mathrm{T} \gg 1$ and $\mu_\mathrm{T} \ll 1$, where the high-frequency rather than the small-frequency modulus is used in the calculation of the Tabor parameter [211].

The numerical Tabor parameters at the scale of local parameters turns out to be $\mu_\mathrm{T} \approx 1.55$ for either profile when using the default discretization of $4,096 \times 4,096$ and thus $\rho = 0.187$ to 0.264 µm, because the peaks in the (ideal) profile have a local radius of curvature of $R = 190 \pm 20$ µm. The range of values originates from different curvatures in x and y direction rather than from differences between hexagonal and triangular patterns. Thus, while $\mu_\mathrm{T} \approx 1.55$ produces (quasi-static) load-displacement curves similar to short-range adhesion [212], it must be considered long-ranged on approach [199]. Consequently, a perfect match between simulations and experiment cannot be expected to reproduce experimental results with close-to-perfect precision, at least not using currently available methods and computers. If surfaces were not corrugated, the generalized Tabor parameter for the flat punch would be reasonably large, i.e., $\mu_\mathrm{T} \approx 10$ for the $2,048 \times 2,048$ resolution and $\mu_\mathrm{T} \approx 14$ for $4,096 \times 4,096$.

6.3.2.3 Refinements and corrections

A few adjustments were made to the numerical model in order to facilitate the comparison between simulations and experiments. Firstly, the velocity inversion was not abrupt but happened over a few but sufficiently many time steps to yield a smooth force-distance relation. Secondly, the 3D printing process introduces deviations from the ideal reference model, most notably an undesired macroscopic curvature induced by thermal shrinkage, which was reflected in the numerical model. In selected simulations, we also accounted for the quasi-discrete height steps of $\Delta z = 0.2\,\mu\text{m}$, which result from the layer-by-layer nature of the printing process. Final results were only marginally affected by this since Δz is of similar order of magnitude as our interaction ranges $\rho = 0.187$ to $0.264\,\mu\text{m}$ and the steps in the topography are not very sharp.

A final technical aspect deserves mentioning. For reasons of computational efficiency, the buffer between the indenter and its periodic image should be made as small as possible but large enough so that the stress field on the indenter is not significantly affected by periodic images. This is achieved quite well with our choice of $L = 4a$. However, the center-of-mass $\tilde{u}(q = 0)$ of a periodically repeated surface deviates from $u_\infty = u(r \gg a)$ that would be obtained in a real system without periodic boundary conditions (PBC). An example of this difference is depicted in the form of the dashed and solid red lines in **Figure 6.5 a**. Given that $a/h = 5$ yields a contact stiffness 20% in excess of the semi-infinite case [213,214], the system can be approximately treated as semi-infinite so that the correction

$$u_\infty \approx 6u(L_x/2, L_y/2) - 5u(L_x/2, 0) \tag{6.9}$$

can be used, which was originally identified for sharp indenters in square simulation cells [212]. The described adjustment can also be thought of as a correction

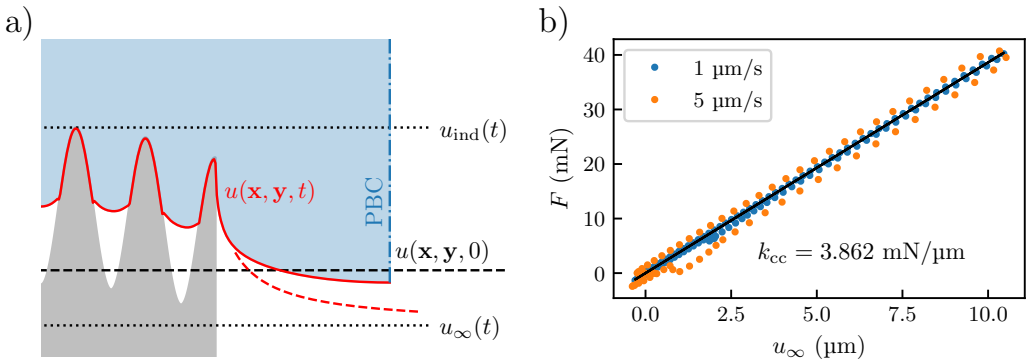

Figure 6.5: a) Illustration of the different displacements considered for compliance correction. **b)** Linear fit of u_∞ for stiffness evaluation.

of unwanted compliance in the system, which does not always require a change of

the experimental/numerical procedure. If the mismatch between ideal and measured displacement is caused by a quasi-static elastic stiffness k_{cc}, it can usually be accounted for by either adding or subtracting its contribution via post-processing of the data:

$$u_{\mathrm{ideal}}(t) \approx u_{\mathrm{ind}}(t) \pm F(t)/k_{\mathrm{cc}}. \tag{6.10}$$

One thing to keep in mind with this method is that the occurrence of local instabilities, e.g. pull-off events, generally depends on the mechanical stability of the system. The effect of k_{cc} on these phenomena cannot be eliminated afterward. For a viscoelastic system, it may also be detrimental that a measurement performed at constant speed $u_{\mathrm{ind}} = v_{\mathrm{ext}}t$ implies that $\mathrm{d}u_{\mathrm{ideal}}(t)/\mathrm{d}t$ varies over time as $(1/k_{\mathrm{cc}})\mathrm{d}F(t)/\mathrm{d}t$. Consequently, this alternative compliance correction can be useful to approximately extract the correct slope $\mathrm{d}F(t)/\mathrm{d}u_{\mathrm{ideal}}(t)$ from both experimental and numerical data, but leaves other systematic errors in the curve unaltered.

Strictly speaking, the difference between u_∞ and $\tilde{u}(q = 0)$ in simulations is of viscoelastic rather than quasi-static nature. However, especially for a small driving velocity, the macroscopic displacement changes very slowly compared to local displacements, so that it can be approximated as quasi-static and we can determine the associated stiffness k_{cc} from a linear fit. From **Figure 6.5 b**, we find that

$$u_{\mathrm{ideal}}(t) - u_{\mathrm{ind}}(t) = u_\infty(t) = \pm F(t)/k_{\mathrm{cc}} \tag{6.11}$$

is almost perfectly fulfilled across the whole load-displacement curve for $v_{\mathrm{ext}} = 1\,\mu\mathrm{m\,s^{-1}}$ with $k_{\mathrm{cc}} = 3.862\,\mathrm{mN\,\mu m^{-1}}$. For larger values of v_{ext}, viscoelastic effects become non-negligible and the data points extracted from simulations form a hysteresis around the linear fit.

6.3.3 Experimental methods

The computer-generated topographies shown in **Figure 6.2** were converted to STL file format and 3D printed using a two-photon lithography direct laser writing device (Photonic Professional GT2, Nanoscribe, Karlsruhe, Germany). The resulting 3D model was vertically sliced into slabs with a thickness of 0.2 to 1.0 µm and laterally hatched with a fixed width of 0.5 µm.

During the vertical slicing, an adaptive option was enabled to achieve better accuracy in the complex curved shapes near the surface. For the printing process, a commercial photoresist (Nanoscribe, Karlsruhe, Germany) IP-S with an elastic modulus, $E_{\mathrm{IP\text{-}S}} = 1.34\,\mathrm{GPa}$, was used in dip-in mode. A 25x objective, writing speed of $100\,\mathrm{mm\,s^{-1}}$, and a laser power of 40 mW were adopted. The surface

topography of the indenters was measured using a confocal microscope (MarSurf CM expert, Mahr, Göttingen, Germany).

The substrate was fabricated from PDMS (Sylgard 184, Dow, Midland, MI, USA) by mixing the base and the curing agent in a ratio of 10:1. The prepolymer was mixed and degassed using a Speed-Mixer (DAC600.2 VAC-P, Hauschild Engineering, Hamm, Germany) with 2350 rpm at 1 mbar for 3 min and then cured at 95 °C for 1 h. Tack tests were performed using a custom-made ten-

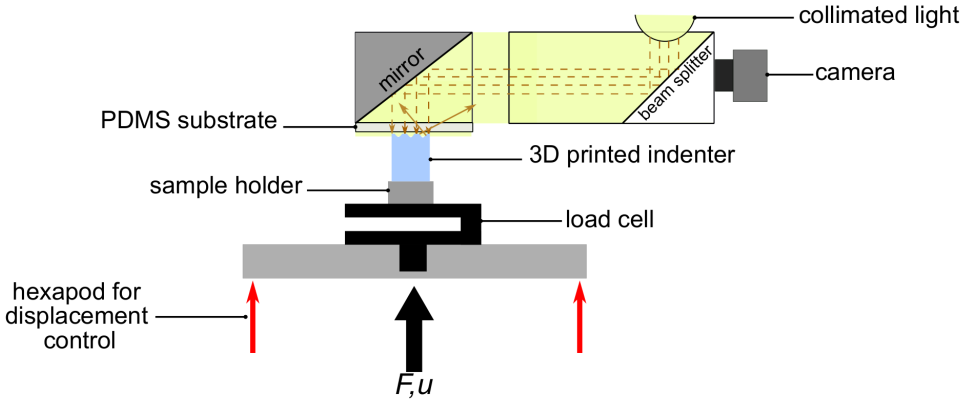

Figure 6.6: Schematic representation of the experimental setup. It consists of a "coaxial illumination" based optical setup for contact observation, a hexapod for displacement control, and a load cell for force measurement.

sile tester equipped with a 2 N load cell as illustrated in **Figure 6.6**. The testing setup in this configuration was measured to have an effective machine stiffness of $k_{\mathrm{M}} = 38.1\,\mathrm{kN\,m^{-1}}$. A hexapod (SMARPOD) and a modular positioning system with six degrees of freedom (SmarAct, Oldenbug Germany) were used for high-resolution displacement and alignment. The PDMS substrate was fixed on the modular positioning system using a holder equipped with a mirror.

The development of optical observation techniques has benefited a wide range of applications, notably for assessing the true contact area between solids. Frustrated total internal reflection started to be applied to image the contact in the 1960s [105, 106]. Similar set-ups are routinely employed nowadays to measure stress distributions [107], contact area of rough surfaces [215], or to visualize the contact formation and separation of fibrillar microstructures [48,62,157,171,175]. Despite the successful use of this technique to determine multiple contact properties, obtaining high contrasts is limited to observing the contact of an opaque specimen through a transparent target surface. Another technique that was employed for contact measurement is the optical interference observed as Newton's rings [106, 216, 217]. The relevance of this technique in contact mechanics and tribology was boosted after Krick *et al.* [108] employed it to develop an *in-situ* optical micro tribometer, which allowed them to visualize the intimate contact

between solids during loading and sliding experiments. In this work we present a new approach for contact observation based on the coaxial lighting principle. Through this approach, we enhanced the contrast between the contact and non-contact areas. Using light from a collimated light source (collimated LED, Thorlabs, New Jersey, USA), a parallel light beam was created for homogenous lighting. The parallel beam scatters at the contact points between the indenter and the substrate which appears darker in the camera.

Videos of the contact were recorded at 50 frames per second using a digital camera (DFK 33UX273, Imaging Source Europe GmbH, Bremen, Germany). Two extra side views cameras were used to help with the alignment. For the adhesion measurement the indenter was brought into contact with the substrate until reaching the defined compressive preload.

All experiments were performed in a laboratory with regulated temperature of $21.0 \pm 0.2\,°C$ and relative humidity at $50 \pm 5\,\%$.

6.4 Results

6.4.1 3D printing

We first analyze optical images of the experimental topographies obtained by the 3D printing process. **Figure 6.7 a** shows the difference between targeted and measured height profiles exemplarily for the triangular surface. Artifacts from the optical measurements were corrected during numerical post-processing and validated against selected tactile line scans. The main deviation between ideal and real topographies is a mean curvature, which is supposedly due to thermal shrinkage of the resin after deposition.

Curvature effects were included in the topographies used in the simulations. Differences between the ideal and simulated height profiles are depicted in **Figure 6.7 b**. We note in passing that ignoring the curvature effects substantially reduces the agreement between simulations and experiment, the most important post-correction being the reduction of height near the rim of the indenter, where the flat-punch solution produces stress singularities.

6.4.2 Tack tests for the triangular surface

Figure 6.8 shows the measured and simulated load-displacement curves obtained for the triangular surface. For tidiness, only the detachment parts of the curves are highlighted in color, since the loading process, shown in a gray dashed line, is smooth and rather insensitive to the approach velocity. Experiments and

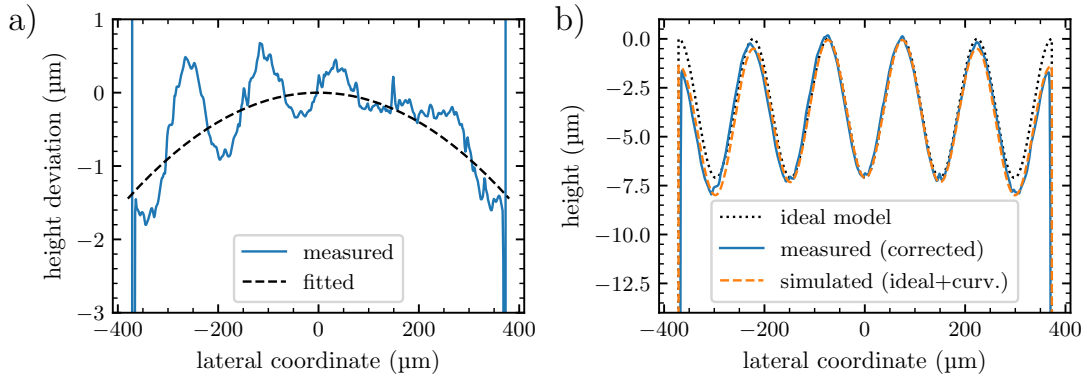

Figure 6.7: Line profiles extracted from a 2D confocal microscope image for **a)** the triangular and **b)** the hexagonal surface compared to the digital model.

simulations show similar trends: Two bulges occur at small velocity v_{ext} and small preload F_{pl}. A bulge located at slightly compressive force is related to the detachment of saddle points—as revealed in more detail further below—while the bulge at tensile force relates to the final pull-off process. Their locations approach each other when either v_{ext} and/or F_{pl} is increased. Ultimately, they merge into a single minimum, whose value corresponds to the (negative) pull-off force. Although experimental and simulated curves agree only semi-quantitatively, the tensile pull-off force is increased from about $F_{\text{p}} = 2.5 \pm 0.5\,\text{mN}$ for a preload force of $F = 40\,\text{mN}$ to $F_{\text{p}} = 14 \pm 1\,\text{mN}$ for $F = 80\,\text{mN}$ in both simulations and experiments.

To match the pull-off force satisfactorily not only for the preloads $F = 40\,\text{mN}$ and $F = 80\,\text{mN}$ but also for $F = 60\,\text{mN}$, the relaxation time for the intermediate preload was adjusted from $\tau = 3.16\,\text{ms}$ to $\tau = 1.26\,\text{ms}$, while keeping $E_\infty/E_0 = 250$ constant. The need for different relaxation times for the three preloads—in fact, the numerically produced $F = 40\,\text{mN}$ and $80\,\text{mN}$ unloading curves could have been further improved by choosing individual relaxation times for them—indicates that the numerical approach to the viscoelasticity is not yet ideal. We believe the two main deficiencies to be the relatively large range of adhesion used in the simulations, see also the discussion at the end of section **6.3.2.2**, and the approximation of a quite complex Prony series representing the frequency-dependent viscoelastic modulus with a single Maxwell element. We were thus surprised that minor tweaking of one parameter for one preload and one pattern was sufficient to achieve the given level of semi-quantitative agreement, the more so as minor changes to the viscoelastic properties of the indenter turn out to have large effects.

The sensitivity of the load-displacement curves w.r.t. range of adhesion and the viscoelastic model will be scrutinized, after establishing that the semi-

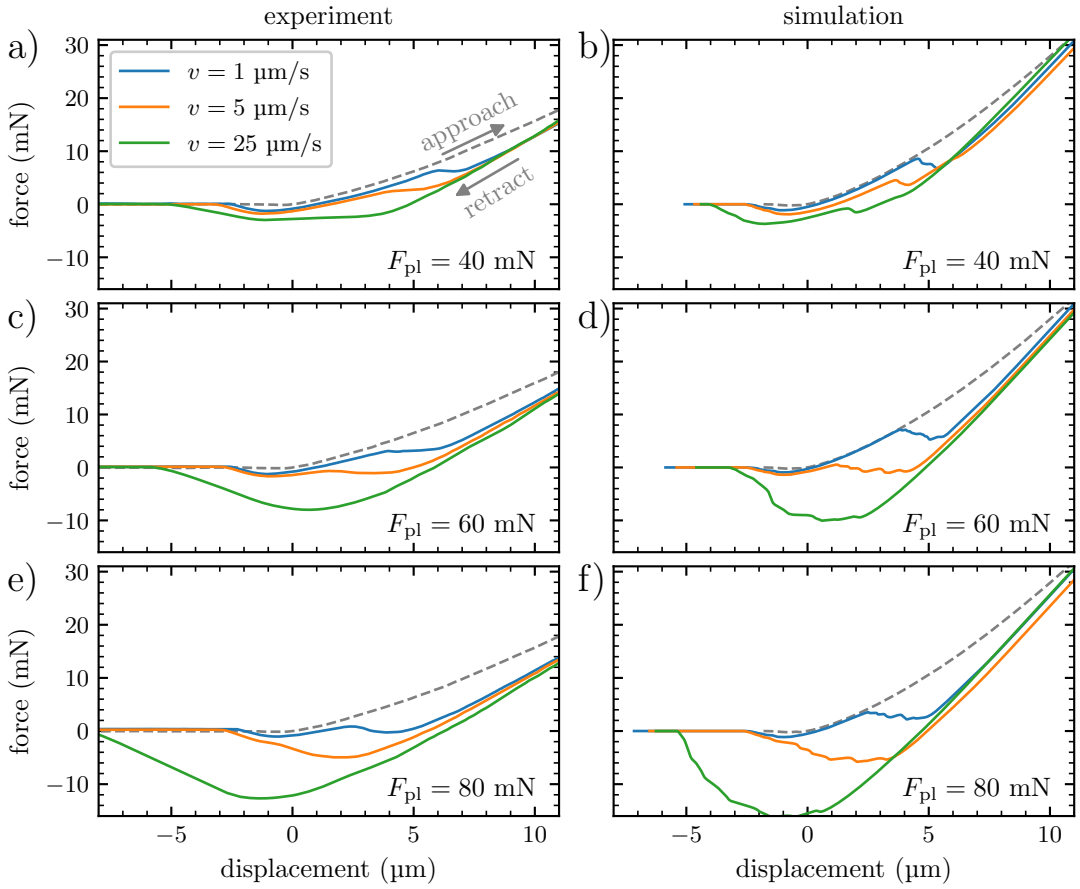

Figure 6.8: Load-displacement curves recorded during the detachment of the Tri surface at different velocities. The left column (**a**, **c**, and **e**) always shows experimental results, while the right column (**b**, **d**, and **f**) shows single-relaxation time simulations. From the first to the last row, the preload is increased from 40 to 60 and then 80 mN. The compliance has been adjusted using k_{cc} as explained in section **6.3.2.3**.

quantitative agreement between experimental and simulated load-displacement curves is not fortuitous: experimental and simulated contact topographies evolve in concert, as is revealed exemplarily in **Figure 6.9** for the preload of $F = 40\,\mathrm{mN}$ and the retraction velocity of $v_{\mathrm{ext}} = 1\,\mu\mathrm{m\,s^{-1}}$. However, before getting to these two points in more detail, we first explain the used gray scales: in the simulations representing two differently parametrized single-relaxation time models, dark gray means contact (negative gap), medium gray adhesive contact ($0 \leq g < \rho$), while light gray is non-contact and very light gray the background color. The gray shades in the real-laboratory, optical images do not allow us to determine the true interfacial separation to a high precision. Yet, very dark pixels indicate contact, while less dark and bright pixels indicate non-contact. Given that the range of adhesion used in the simulations is about a factor two to four smaller than the wavelength of light, we expect that the simulated "adhesive non-contact" probably still appear quite dark in the optical images. Thus, the somewhat darker nature of the experimental images is in part due to color coding. Improving this would have been possible, but it would have taken us the possibility to visualize the non-contact zones of high adhesion. Experiments and simulations have similar characteristics.

At the point of maximum preload, contact occurs in all peaks but only if saddle points if they are close to the outer rim, despite the curvature correction. The detachment process evolves first most notably near the saddle points (from the inner to the outer parts of the contact) and contact exists only in the peak of asperities at a load, at which the load-displacement relation is between the two bulges upon separation. Similar qualitative agreement was found between real-laboratory and *in-silico* movies for all load-displacement curves shown in this study. For the given "movie", we could establish that the bulge in the force-displacement curve near 6 µm is due to saddle-point detachment at the outer rim of the corrugated punch.

Despite qualitative agreement, quantitative differences can be observed between experiments and simulations. While the initial experimental and simulated frames at the maximum preload in the left column of **Figure 6.9** look astoundingly similar, given that the simulations must be seen as long-range adhesion on approach, the experimental contact barely changes to the next shown image. In contrast, the *in-silico* contact reveals a noticeable retardation or aftereffect from the moments of high compression during the initial decompression in that the contact keeps growing slightly. We attribute this to the necessity of large viscoelastic relaxation times for a proper reproduction of the dissipation caused by moving cracks. This makes the response to simple indentation be too sluggish so that aftereffects of the compression branch are noticeable shortly after inverting

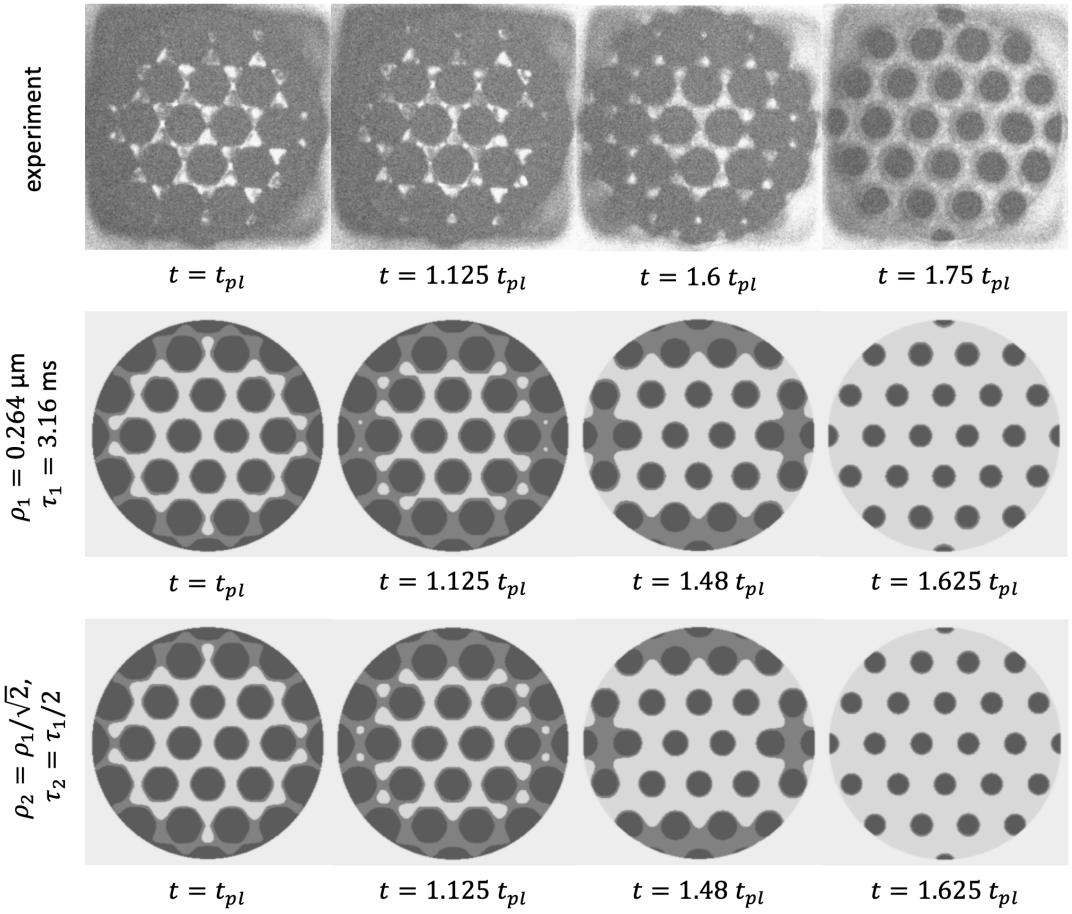

Figure 6.9: Contact observation during a tack test of the Tri surface at $1\,\mu\mathrm{m\,s^{-1}}$ and a maximum compressive load of 40 mN. The upper row shows experimental data, while the bottom two rows represent simulations using different relaxation time τ and range of adhesion ρ. The darker areas represent contact, while the lighter areas represent non-contact. For simulations, medium and dark gray indicate attractive and repulsive contact, respectively. t_{pl} denotes the time between first contact and preload for the respective row. The times for the last two columns are located just before and past the bulge in the force-displacement curve on the compressive part of the unloading curve. Similar features are observed in all cases, e.g., the loss of contacts in the saddle points starts from the center and moves outward and contact exists in all asperities but in no saddle point before the maximum tensile force is reached upon detachment, i.e., at a displacement near 2 µm.

the direction of motion. Upon further decompression, the trend reverses and the contact evolves slightly more slowly in the experiments than in the simulations: the destruction of contact at the saddle points, which occurs between the last two columns of **Figure 6.9** and which correlates with a shallow minimum in the (compressive) force on retraction, happens earlier in the simulations than in the experiments.

To elucidate the role of the range of adhesion on the dynamics, we contrast the contact formation obtained in two simulations based on slightly different models, which both assume a single relaxation time and the same E_∞/E_0 ratio. The second model uses a range of adhesion that is reduced by a factor of $1/\sqrt{2}$ w.r.t. the first model while the relaxation time was halved to achieve close agreement between the dynamics of the two models. A slightly different redefinition of the relaxation time might have led to even better agreement. However, even with the made choice, the second and the third row of **Figure 6.9**, representing the first and second single-relaxation time model, respectively, barely allows the naked eye to distinguish the contact break-up between the two models. Only the second contact images, taken at a time 1.125 t_{pl}, where t_{pl} is the time elapsed between initial contact and maximum compressive load, differ slightly: the simulation with a larger range of adhesion generally produces larger zones of noticeable adhesive tension indicated by medium gray.

The reason why changing the viscoelastic relaxation time can be "compensated" by a change in the range of adhesion ρ during the retraction process is an interplay between the range of adhesion and the viscoelastic properties of the elastomer [198, 200]. The dissipation caused by the propagating opening cracks must be reproduced in simulations in order to yield accurate load-displacement curves. Since steeper slopes at the contact edge imply larger (relative) velocities in a moving crack and thus enhanced dissipation, a shorter range of adhesion leading to steeper slopes can be compensated by shorter relaxation times used in the viscoelastic model.

To elucidate the role of viscoelasticity, three different viscoelastic models were considered in addition to the purely elastic model reflecting the quasi-static limit. Their frequency-dependent contact moduli are depicted in **Figure 6.10 a** with model 1 having a single relaxation time of $\tau = 6.32\,\mathrm{ms}$ and $E_\infty/E_0 = 250$, while model 2 and 3 contain five relaxation times—with ratios and weight chosen as described in section **6.3.2** and $\tau_{\mathrm{min}} = 0.6\,\mathrm{ms}$. Moreover, $E_\infty/E_0 = 8$ in model 2 and $E_\infty/E_0 = 250$ in model 3. Panels b through d of **Figure 6.10** reveal that all three viscoelastic models increase the adhesion hysteresis with respect to the quasi-static model, which is the only one to show no preload dependence of the pull-off force. While the effect is relatively minor for model 2 with its relatively

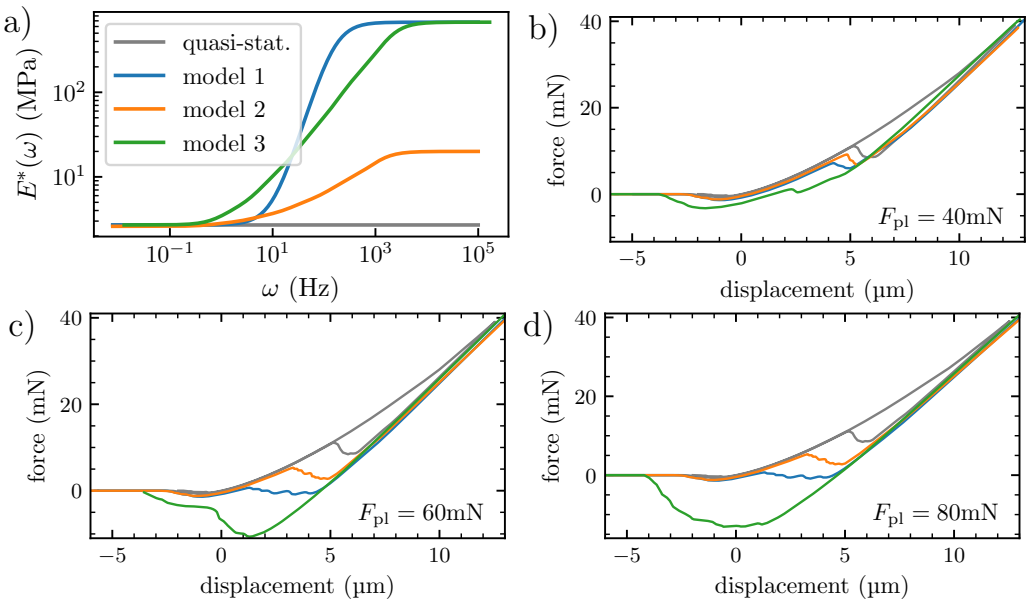

Figure 6.10: a) Frequency-dependent contact moduli for different rheological models. **b**, **c**, and **d**) load-displacement curves obtained for a preload of **b)** 40 mN, **c)** 60 mN and **d)** 80 mN using the different rheological models. The detachment speed is $1\,\mu\mathrm{m\,s^{-1}}$ in all cases.

small E_∞/E_0 ratio, the preload sensitivity is largest for model 3 with a large E_∞/E_0 ratio and a tail of the "excess"-$E(\omega)$ extending to small frequencies. For the intermediate preload of 60 mN, the minimum force and thus maximum tensile force even occurs at negative displacement and is thus clearly associated with the detachment of saddle points rather than with that of asperity peaks.

6.4.3 Tack tests for the hexagonal surface

The tack tests on the hexagonal surface were carried out in an analogous fashion to the triangular surface, except with smaller preloads than before. The resulting load-displacement curves are shown in **Figure 6.11**, this time, for only two different velocities but including the loading part. The $v_{\mathrm{ext}} = 1\,\mu\mathrm{m\,s^{-1}}$ contact evolution is depicted in **Figure 6.12** with an emphasis on the loading rather than the detachment process.

The force-displacement curves contain only one minimum at all velocities for the hexagonal surface. The bulge related to the saddle-point detachment in the triangular surface has disappeared for the hexagonal pattern because their detachment coincided in all investigated cases with that of the asperity peaks. This is because saddle points are almost as high as the peaks in the hexagonal lattice. In fact, they are so high that contact formation of saddle points between two asperities is instantaneous in the quasi-static limit, which in turn is due to the fact that the height of contact line of a zero-load isolated asperity (in the Hertzian,

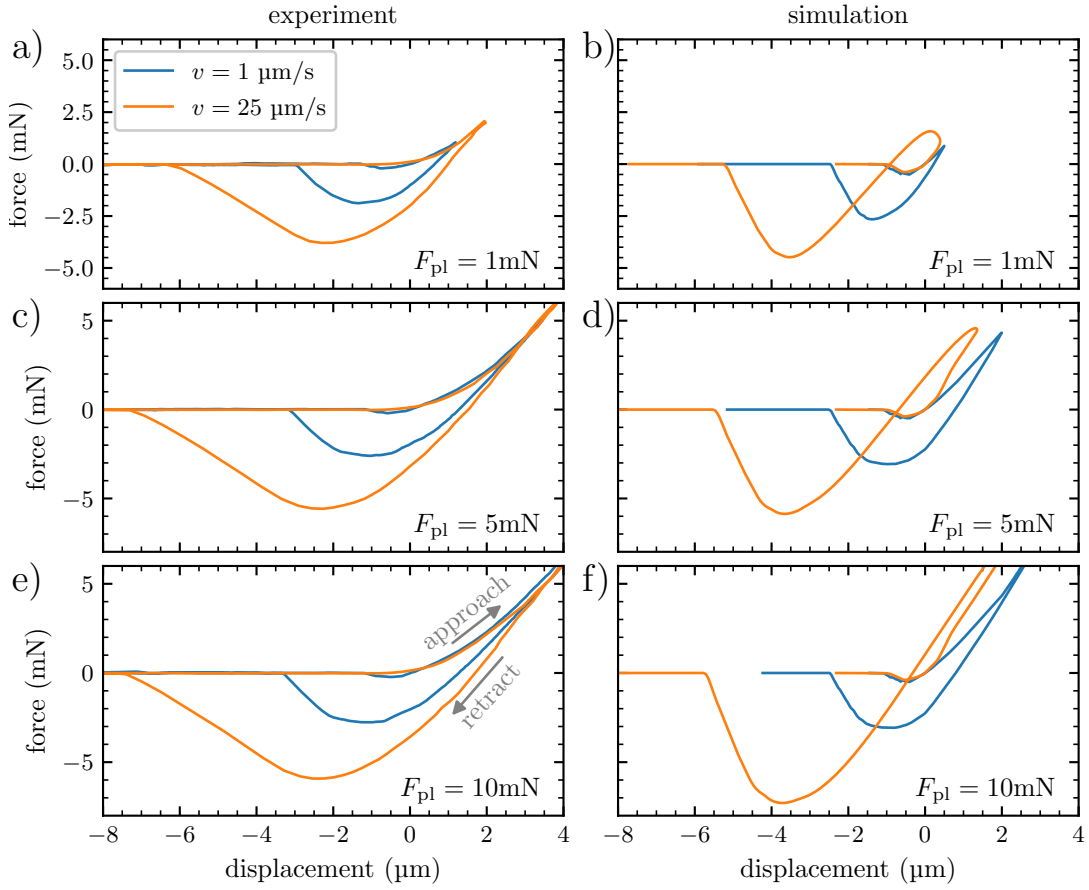

Figure 6.11: Load-displacement curves obtained during detachment of the Hex surface at different velocities. The left column (**a**, **c**, and **e**) shows experimental results, while the right (**b**, **d**, and **f**) column shows single-relaxation time simulations. From the first to the last row, the preload is increased from 1 to 5 and then 10 mN. The compliance has been adjusted using k_{cc} as explained in section **6.3.2.3**.

i.e., parabolic approximation) extends down to a height where the corrugated profile crosses over from convex to concave. Due to the large dissipation of a propagating closing crack, viscoelastic saddle-point contact formation is far from being instantaneous.

While the detachment curve shows more features for the triangular than for the hexagonal pattern, the opposite is true for the contact formation, at least as far as the *in-silico* realization of the default model is concerned. First, strong aftereffects occur in the simulations for small preloads right after velocity inversion for $v_{\mathrm{ext}} = 25\,\mu\mathrm{m\,s}^{-1}$. They result in what could be called an "anti-hysteresis"—though the ordinary hysteresis that occurs during the later portion of the detachment process will always ensure that a closed loop dissipates and does not produce energy. We thus abstain from postulating that design principles for energy-harvesting nano-scale machines could be deduced, just because "negative friction" appears to show up for a brief moment of time. Instead, we relate the

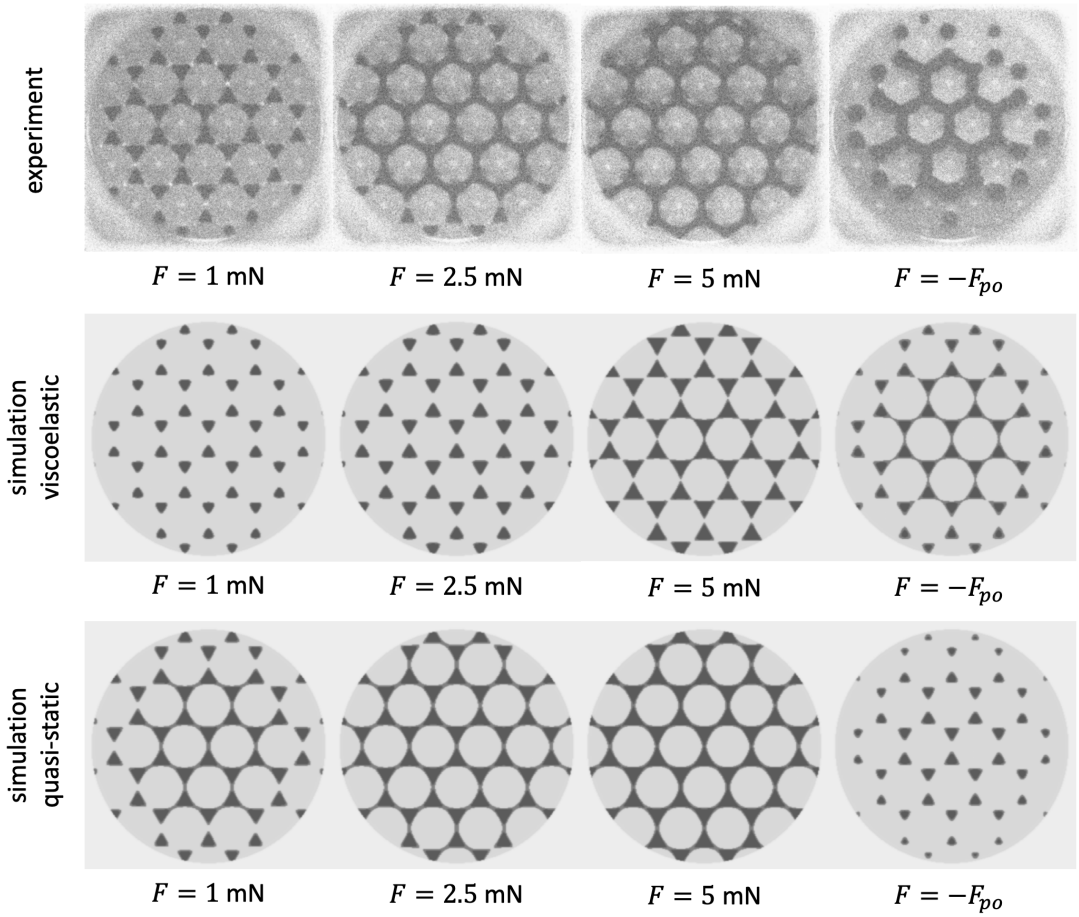

Figure 6.12: Contact observation during a tack test of the Hex surface at $1\,\mu\mathrm{m\,s^{-1}}$ and a maximum compressive load of 10 mN. The upper row is taken from the experiment, the middle row from a simulation with a single relaxation time ($\tau = 3.16\,\mathrm{ms}$ and $\rho = 2.642\,\mu\mathrm{m}$) and the bottom row from a quasi-static simulation with the same range of adhesion ρ. Gray scales as in **Figure 6.9**. Frames are taken from the approach part of the tack test, except for the last one at the point of maximum tensile force. In real-laboratory and *in-silico* contacts, all maxima are always in contact while saddle points close to the rim only come into contact with increasing load. The attachment of saddle points and asperities is clearly separated on approach, but their detachment occurs quasi-simultaneously.

strong retardation effects during compression once more to the large relaxation times, which are needed to better match the dissipation of propagating cracks in the experiments. Second, once the saddle points have made contact, the interfacial stiffness, defined as the slope of the force-displacement curve, is much enhanced once the saddle points have made contact. This is best revealed in the $v_{\mathrm{ext}} = 1\,\mu\mathrm{m\,s^{-1}}$ curve of the largest investigated preload in panel f of **Figure 6.11** near a compressive load of $F = 5\,\mathrm{mN}$. In fact, the contact image reveals saddle-point formation in the lower row of **Figure 6.12** near that load.

Increasing the preload past the point of saddle point formation changes the load-displacement relation for the hexagonal pattern only moderately, particu-

larly little between panels **c** and **e** of **Figure 6.11**, revealing that the experimental unloading curve are virtually identical for $F = 5$ and 10 mN. This can be rationalized by the contact image obtained at the maximum tensile force in the last column of **Figure 6.12**, where most saddle points are still in contact. Those panels also corroborate the statement made at the beginning of the results section that correcting for the "macroscopic" surface curvature induced during cooling of the printing process was needed to achieve reasonable or, depending on viewpoint, good agreement between the laboratory and *in-silico* samples: the contact area close to the rim of the punch is noticeably reduced by the "macroscopic" curvature correction, which became necessary after the resin had cooled off.

6.5 Discussion and conclusions

This work addressed the competition between viscoelastic hysteresis in contact mechanics and the hysteresis due to elastic multistability being responsible for the quasi-discontinuous snap-in and snap-out-of individual contact patches. To this end, we studied numerically and experimentally a flat punch to which small-scale corrugation—in the form of either a hexagonal or a triangular height profile—was added. The two height spectra are identical although the profiles are their mutual inverses, i.e., the phases of the height Fourier coefficients are shifted by π. This makes the saddle points, which are located between two maxima and which turn out crucial for the contact mechanics, be higher for the hexagonal than for the triangular lattice.

Contact of an *ideal* flat punch forms quasi-instantaneously so that both viscoelastic losses due to closing cracks and multi-stability effects are negligible on approach. Consequently, preload effects of ideal-punch detachment are minor. However, the detachment requires a crack to propagate from the rim to the center, which leads to a viscoelasticity-enhanced work of separation at intermediate pull-off velocities [198,218]. (The work of separation approches $2\gamma A$ at very small and very large velocities, assuming well-defined, finite high- and low-frequency contact moduli.)

After small-scale roughness was added to the flat punch, the wavelength of the pattern being one fifth of the punch diameter, strong preload effects occurred at intermediate operating velocities but not under quasi-static driving. Thus, preload and multi-stability effects are intertwined in our corrugated punch. The preload effects were distinctly larger for the triangular than for the hexagonal pattern.

Specifically, the pull-off force for the hexagonal lattice saturated at roughly

6 (experiment) and 7 mN (simulation) once the preload had reached 5 to 10 mN at an operating velocity of $25\,\mu m\,s^{-1}$, while these two forces where roughly twice and ten times larger, respectively, for the used triangular pattern. Despite these quantitative differences, pull-off forces saturated in both cases once the preload had been large enough to induce contact at the saddle points and retraction was fast enough so that saddle points were still in contact at the point of maximum tensile force. Since the saddle-point heights are rather close to (far from) the height maxima in the hexagonal (triangular) lattice, preload effects saturated earlier in the hexagonal than in the triangular system, although the hexagonal amplitude was chosen more than twice that of the triangular corrugation.

A purely spectral approach to our system, assuming random phases as done in Persson's contact mechanics theory, would not be in a position to reproduce or to predict these trends, which persist if both patterns have identical height amplitudes and thus identical height spectra. However, phase-correlation effects can be included into the theory so that approaches in the spirit of Persson theory might still be applicable. For the investigated set-up, a naive interpretation of Persson's theory would at least predict correctly the trend that the pull-off force is smaller for the punch with the larger spectral density, i.e., for the hexagonal lattice.

Can our results be rationalized with bearing-area models (BAMs), such as the popular approach by Fuller and Tabor [88] for nominally flat, adhesive contacts? BAMs assume the highest asperity to come into contact first and out of contact last, the second-highest peak to come into contact second and out of contact second last, and so on and so forth. The load-displacement laws of the individual peaks, whose shapes are approximated as paraboloids, are then added up to yield a global load-displacement curve. While BAMs are commonly done for quasi-static contact loading, generalization to dynamics seems to be straightforward, e.g., by "feeding" the time-dependent force-displacement relation of an isolated asperity contact at the given operating velocity into the model. For our system, the radii of curvature of the hexagonal and the triangular lattice were virtually identical, because different amplitudes had been used for both profiles making isolated asperities similar. (The minor curvature correction w.r.t. the ideal model changes things quantitatively but not qualitatively.) Thus, the depinning force of a corrugated (ideal) punch would be expected to scale linearly with the number of maxima given fixed heights and fixed radii of curvature. Since the number density of maxima in the hexagonal lattice is twice that of the triangular lattice, BAMs predict roughly twice the adhesion force for our hexagonal than for our triangular patterned punch. Finite-size effects and cut-off asperities at the rim of the punch renormalize that ratio but do not affect the trend. Unfortunately,

things turn out the other way around, i.e., the triangular surface with fewer peaks has clearly greater (viscoelastic) pull-off forces, due to the pivotal role of saddle points. Obviously, BAMs approximating each peak as parabolic intrinsically fail to account for saddle points, which is why we are beyond skeptical of studies reporting models in the spirit of Fuller and Tabor to be quantitative for nominally flat contacts, even if agreement can be fudged during the post-diction of experimental data.

This leaves numerical approaches, such as the here-reported number-crunching exercise, as the least problematic non-experimental tool to tackle adhesive problems similar to that investigated here. Nonetheless, number-crunching is not entirely unproblematic either. We also gauged the model parameters on the experiments that were reproduced, even if the few adjustable parameters were kept constant and not readjusted when preloads, patterns, and operating velocities were changed—except for one set of experiments, specifically those using a 60 mN preload on the triangular pattern, for which the relaxation time was changed by a factor of 2.5. One challenge in the attempt to make quantitative description is the multi-scale nature of the dissipation during viscoelastic crack propagation. The range of adhesion critically affects the dissipation of moving cracks, which must be reproduced correctly, to model the formation and the failure of adhesive contacts reliably. This means that the vicinity of the crack must be resolved with a computationally unfeasible large resolution or the viscoelastic properties of the elastomer relaxation times must be rescaled, which, however, implies that the time-dependent response of the elastomer to a point indenter would no longer be correct.

Despite all difficulties related to the numerical modeling, we would argue that the simulations matched the experiments not only qualitatively but almost quantitatively and that this was not for fortuitous reasons but because the simulations captured the essence of the experiments. We come to this conclusion because the comparison between simulation and experiment went beyond that of contrasting force-displacement curves and included the *in-situ* visualization of the contact dynamics. For this reason, we are confident that any (qualitative) conclusion drawn in this work is on solid grounds. This makes us hopeful that simulations like the ones presented here will soon be in a position to address systems beyond the demonstrator model considered here, such as pressure-sensitive adhesives or hydraulic seals in contact with surfaces having complex and not only single-sinusoidal micro-scale roughness.

Chapter 7

Conclusion

Gecko-inspired structures can be used in a wide range of emerging applications, providing a strong, switchable, and residue-free adhesion. Over the last few years, several key advantages have stirred the interest of many industries in these structures particularly as gripping systems for object handling (see section 2.1.5). However, despite considerable progress in the understanding of the physics behind fibrillar microstructures and the countless efforts for optimizing their design and quality, there are still questions about their reliability as gripping systems. In this regard, we address in the present work this problem from various directions. The approaches presented in this thesis allow the creation of in-line monitoring systems by detecting the contact signature of the fibrillar structures and the prediction of adhesion properties. This research will contribute to the improvement of bio-inspired handling systems. Moreover, it can pave the way for automatic monitoring of the gripping quality, which can ensure reliable use of these structures.

7.1 Summary

The main aspects of this work are summarized in the following:

In **Chapter 3**, supervised learning algorithms and FTIR for *in-situ* observation have been combined for the first time to predict the adhesion performance of fibrillar microstructures. Depending on multiple variations in the possible contact imperfections (such as misalignment and off-center gripping), data was collected in terms of visual features at preload. Three different supervised regression models were trained and compared to a linear mathematical model and an existing analytical model [54]. The comparison revealed that supervised learning could be a fast substitute for expensive models. In contrast to the existing analytical model, supervised machine learning especially SVR and BT, could provide direct predictions of new specimens' adhesion force without the prior knowledge of its

maximum pull-off force, nor the exact values of the misalignment angles. It can also capture deterioration of the quality of the specimens in case of missing or deformed fibrils. Moreover, the analytical model only presented a limiting case, where the back layer of the adhesive is stiff, which is rarely the case in real applications. On the other hand, the linearity of the mathematical model or the linear regression was not able to capture the outliers in the data. Thus, the SVR and BT overcame the limited accuracy of the mathematical and analytical model and proved that it can facilitate near real-time predictions.

However, the data collected in this chapter was in form of a displacement-controlled pull-off test. Transferring these trained models to a force-controlled pick and place application would introduce other variations and reduce the accuracy of the models.

In order to minimize this mismatch between laboratory experiments and real handling applications, **Chapter 4** presents a classification approach to predict the gripping performance from data collected directly using a pick and place robot. In this section, classification models were combined with FTIR and image processing to predict the successful and unsuccessful gripping of a glass object. 3 classifiers were trained depending on the object mass. The tested models for the different classifiers showed high scores of more than 90 %. Including more visual features at a lifting position increased this accuracy as it captured the rotation of the object in the case of off-center gripping, i.e., the object either goes back into contact or a peeling moment is created depending on the direction of the misalignment.

The FTIR technique employed in these two chapters enabled the distinction of fibrils in contact from those that are not. It also showed sufficient contrast for observing array scale defects such as misalignment, missing pillars, and relatively significant defects at the fibrils scale. However, this technique can only be used when the target object is transparent and smooth. The limitation to using this optical technique with opaque and rough surfaces would constrain the integration of the predictive system in the pick-and-place application. Hence the need for a new approach to expand the possibilities of observing contact with different types of objects.

Toward this end, two new optical systems were developed in **Chapter 5**. The optical devices look through the fibrils, into contact with the target surface from the back side of the fibrillar microstructures. The first device a "precision setup" produced images with high contrast to detect the contact signature of the fibrils. It also allowed the detection of contact imperfections such as misalignment, defected fibrils, and the presence of roughness. There are, however, some disadvantages of this device, including its size, expensive optics, and dependency

on light intensity. A second approach was taken to develop the second device which is a "compact setup". This setup is inexpensive and much smaller. It produced however an inhomogeneous light distribution and reflections that are tough to avoid. Despite this, the device is able to detect the contact signature of the structured pad and the contact imperfections with high contrast. Although both devices are able to detect the presence of roughness in the contact signature of the fibrillar structures – which is a first for an *in-situ* observation technique – it does not capture the small-scale roughness and it is difficult to extract real contact area from the images.

In an attempt to capture the contact signature of rough surfaces, **Chapter 6** of this thesis presents a quantitative comparison between experimental and simulated contact signature and force measurement. Contact signature of fibrillar structures in contact with real multiscale roughness is very hard to obtain with high details using optical systems. Nevertheless, a first approximation could allow us to understand adhesion dependencies and bring us a step closer to predicting adhesion in various scenarios. Therefore, in this project two single wavelength patterns (roughness-like surfaces) were generated and 3D printed as stiff cylindrical indenters. The contact signature of the indenter with a PDMS film was then obtained (instead of fibrillar structures) using coaxial illumination technique to enhance the contrast of the asperities in and out of contact. Using GFMD, we were able to replicate experimentally obtained contact signatures, and provide new insight into the effect of the viscoelastic properties of PDMS, preload and retraction rate on the pull-off force and the microscopic detachment mechanism.

In fact, the dissipation of the viscoelastic energy –when the preload or the retraction velocity is high, or when the topographical saddle points are shallow– leads to an increase in the force needed to separate the surfaces. This can be observed when detachment of the saddle points and asperities of the indenter occurs simultaneously. In contrast, when the velocity is lower than the characteristic viscoelastic relaxation times, and the asperities significantly surpass the saddle points, the saddle points detach before the asperities and the pull-off force is not affected. This case only approximates the behavior of the quasi-static elastic model which is commonly used in literature.

7.2 Outlook

In this work, we have shown different approaches to detect the contact signature, and predict the adhesion performance of micropatterned structures. There are considerable opportunities for further research in this area. This thesis consists of three main parts and therefore opens three different research paths:

Including machine learning to monitor the gripping performance of the bioinspired structures from the contact signature has proved to be efficient. The ability to achieve high accuracy with artificial intelligence can reduce human error and increases the chances of reliable handling. However, it is critical that all the real-world variations are reflected in the data collected for training and testing these models. While some major problems –such as misalignment and off-center gripping– were taken into consideration in this study, more variation of the data would increase the accuracy under different circumstances. In fact, the acceleration and velocity of the robotic arm and the holding times between the different attachments/detachments could alter the behavior of the fibrillar structure and therefore the accuracy of the prediction. It is also possible to extend the use of ML and *in-situ* observation to correct these possible variations, notably misalignment and off-center gripping. Since these two problems can cancel each other as can be seen in **Figure 4.5**, programming the robot to use one to correct the other could be possible if they are predicted before detachment without the need for human intervention. Likewise, it can be used for quality control and suggesting the replacement of damaged adhesive pads.

Integrating the newly developed optical systems and combining them with ML could also open up more possibilities for monitoring the correct grasping of various opaque and rough objects. These devices can also pave the way to other applications such as the detection of defected objects or the observation of the object environment. However, towards more scientific-oriented applications, further improvement of the two setups is still needed.

Simulating macroscopic systems accurately would need an exact definition of the range of adhesion and the different experimental challenges in more detail. Moreover, the need for extremely precise surface topographies complicate the use of simulation to predict real-world conditions. In fact, it is still difficult to detect very small features on natural rough surfaces using optical techniques or macroscopic simulations. Improvements in these areas will bring us closer to address systems exceeding the considered model.

In the long run, detecting the contact signature and predicting adhesion performance in-line will promote the integration of fibrillar microstructures not only as reliable gripping devices but could also set the stage for other smart and controlled applications.

List of Figures

List of Tables

Bibliography

[1] E. Arzt, H. Quan, R. M. McMeeking, and R. Hensel, "Functional surface microstructures inspired by nature – from adhesion and wetting principles to sustainable new devices," *Progress in Materials Science*, vol. 120, p. 100823, 7 2021.

[2] J. M. Benyus, "Biomimicry: Innovation inspired by nature," 1997.

[3] K. Koch, B. Bhushan, and W. Barthlott, "Multifunctional surface structures of plants: An inspiration for biomimetics," *Progress in Materials Science*, vol. 54, pp. 137–178, 2 2009.

[4] T. B. Schroeder, J. Houghtaling, B. D. Wilts, and M. Mayer, "It's not a bug, it's a feature: functional materials in insects," *Advanced Materials*, vol. 30, no. 19, p. 1705322, 2018.

[5] K. Autumn and J. Puthoff, "Properties, principles, and parameters of the gecko adhesive system," *Biological Adhesives*, pp. 245–280, 2016.

[6] R. Hensel, K. Moh, and E. Arzt, "Engineering micropatterned dry adhesives: From contact theory to handling applications," *Advanced Functional Materials*, vol. 28, p. 1800865, 7 2018.

[7] H. Gao, X. Wang, H. Yao, S. Gorb, and E. Arzt, "Mechanics of hierarchical adhesion structures of geckos," *Mechanics of materials*, vol. 37, no. 2-3, pp. 275–285, 2005.

[8] K. Autumn, Y. A. Liang, S. T. Hsieh, W. Zesch, W. P. Chan, T. W. Kenny, R. Fearing, and R. J. Full, "Adhesive force of a single gecko foot-hair," *Nature*, vol. 405, pp. 681–685, 6 2000.

[9] K. Autumn, M. Sitti, Y. A. Liang, A. M. Peattie, W. R. Hansen, S. Sponberg, T. W. Kenny, R. Fearing, J. N. Israelachvili, and R. J. Full, "Evidence for van der waals adhesion in gecko setae," *Proceedings of the National Academy of Sciences*, vol. 99, pp. 12252–12256, 9 2002.

[10] E. Arzt, S. Gorb, and R. Spolenak, "From micro to nano contacts in biological attachment devices," *Proceedings of the National Academy of Sciences*, vol. 100, pp. 10603–10606, 9 2003.

[11] K. Autumn, "How gecko toes stick," *American Scientist*, vol. 94, p. 124, 2006.

[12] C. Y. Hui, N. J. Glassmaker, T. Tang, and A. Jagota, "Design of biomimetic fibrillar interfaces: 2. mechanics of enhanced adhesion," *Journal of the Royal Society Interface*, 2004.

[13] A. Jagota, "Mechanics of adhesion through a fibrillar microstructure," *Integrative and Comparative Biology*, vol. 42, pp. 1140–1145, 12 2002.

[14] H. Lee, B. P. Lee, and P. B. Messersmith, "A reversible wet/dry adhesive inspired by mussels and geckos," *Nature*, 2007.

[15] A. del Campo, C. Greiner, and E. Arzt, "Contact shape controls adhesion of bioinspired fibrillar surfaces," *Langmuir*, vol. 23, pp. 10235–10243, 9 2007.

[16] R. Spolenak, S. Gorb, and E. Arzt, "Adhesion design maps for bio-inspired attachment systems," *Acta Biomaterialia*, vol. 1, pp. 5–13, 1 2005.

[17] A. V. Spuskanyuk, R. M. McMeeking, V. S. Deshpande, and E. Arzt, "The effect of shape on the adhesion of fibrillar surfaces," *Acta Biomaterialia*, vol. 4, pp. 1669–1676, 11 2008.

[18] K. Kendall, "The adhesion and surface energy of elastic solids," *Journal of Physics D: Applied Physics*, vol. 4, p. 320, 8 1971.

[19] W. Brockmann, P. L. Geiß, J. Klingen, and K. B. Schröder, *Adhesive bonding: materials, applications and technology*. John Wiley & Sons, 2008.

[20] B. N. J. Persson, O. Albohr, U. Tartaglino, A. I. Volokitin, and E. Tosatti, "On the nature of surface roughness with application to contact mechanics, sealing, rubber friction and adhesion," *Journal of Physics: Condensed Matter*, vol. 17, pp. R1–R62, 1 2005.

[21] L. Heepe and S. N. Gorb, "Biologically inspired mushroom-shaped adhesive microstructures," *Annual Review of Materials Research*, vol. 44, pp. 173–203, 7 2014.

[22] D. M. Slater, M. J. Vogel, A. M. Macner, and P. H. Steen, "Beetle-inspired adhesion by capillary-bridge arrays: pull-off detachment," *Journal of Adhesion Science and Technology*, vol. 28, pp. 273–289, 2 2014.

[23] M. J. Vogel and P. H. Steen, "Capillarity-based switchable adhesion," *Proceedings of the National Academy of Sciences*, vol. 107, pp. 3377–3381, 2 2010.

[24] A. M. SMITH, "Negative pressure generated by octopus suckers: A study of the tensile strength of water in nature," *Journal of Experimental Biology*, vol. 157, pp. 257–271, 5 1991.

[25] F. Tramacere, A. Kovalev, T. Kleinteich, S. N. Gorb, and B. Mazzolai, "Structure and mechanical properties of octopus vulgaris suckers," *Journal of the Royal Society Interface*, vol. 11, 2 2014.

[26] F. W. Grasso, "Octopus sucker-arm coordination in grasping and manipulation*," *American Malacological Bulletin*, vol. 24, pp. 13–23, 3 2008.

[27] L. Briones, P. Bustamante, and M. A. Serna, "Wall-climbing robot for inspection in nuclear power plants," in *Proceedings of the 1994 IEEE International Conference on Robotics and Automation*, pp. 1409–1414, IEEE, 1994.

[28] Y.-C. Chen and H. Yang, "Octopus-inspired assembly of nanosucker arrays for dry/wet adhesion," *ACS Nano*, vol. 11, pp. 5332–5338, 6 2017.

[29] F. Tramacere, L. Beccai, E. Sinibaldi, C. Laschi, and B. Mazzolai, "Adhesion mechanisms inspired by octopus suckers.," in *FET*, pp. 192–193, 2011.

[30] A. Wang, Y. Zhou, and M. H. Müser, "Modeling adhesive hysteresis," *Lubricants*, vol. 9, pp. 1–30, 2 2021.

[31] H. Cho, G. Wu, J. C. Jolly, N. Fortoul, Z. He, Y. Gao, A. Jagota, and S. Yang, "Intrinsically reversible superglues via shape adaptation inspired by snail epiphragm," *Proceedings of the National Academy of Sciences of the United States of America*, vol. 116, pp. 13774–13779, 2019.

[32] J. N. Israelachvili, "Van der waals forces in biological systems," *Quarterly Reviews of Biophysics*, vol. 6, pp. 341–387, 11 1973.

[33] R. Ruibal and V. Ernst, "The structure of the digital setae of lizards," *Journal of Morphology*, vol. 117, no. 3, pp. 271–293, 1965.

[34] N. E. STORK, "Experimental analysis of adhesion of chrysolina polita (chrysomelidae: Coleoptera) on a variety of surfaces," *Journal of Experimental Biology*, vol. 88, pp. 91–108, 10 1980.

[35] G. Huber, H. Mantz, R. Spolenak, K. Mecke, K. Jacobs, S. N. Gorb, and E. Arzt, "Evidence for capillarity contributions to gecko adhesion from single spatula nanomechanical measurements," *Proceedings of the National Academy of Sciences*, vol. 102, no. 45, pp. 16293–16296, 2005.

[36] L. Heepe, A. Kovalev, M. Varenberg, J. Tuma, and S. Gorb, "First mushroom-shaped adhesive microstructure: A review," *Theoretical and Applied Mechanics Letters*, vol. 2, p. 014008, 1 2012.

[37] E. Kroner and E. Arzt, "Single macropillars as model systems for tilt angle dependent adhesion measurements," *International Journal of Adhesion and Adhesives*, vol. 36, pp. 32–38, 7 2012.

[38] R. Balijepalli, M. Begley, N. Fleck, R. McMeeking, and E. Arzt, "Numerical simulation of the edge stress singularity and the adhesion strength for compliant mushroom fibrils adhered to rigid substrates," *International Journal of Solids and Structures*, vol. 85, pp. 160–171, 2 2016.

[39] G. Carbone and E. Pierro, "A review of adhesion mechanisms of mushroom-shaped microstructured adhesives," *Meccanica*, vol. 48, no. 8, pp. 1819–1833, 2013.

[40] B. Aksak, C.-Y. Hui, and M. Sitti, "The effect of aspect ratio on adhesion and stiffness for soft elastic fibres," *Journal of The Royal Society Interface*, vol. 8, no. 61, pp. 1166–1175, 2011.

[41] C.-Y. Hui, A. Jagota, L. Shen, A. Rajan, N. Glassmaker, and T. Tang, "Design of bio-inspired fibrillar interfaces for contact and adhesion—theory and experiments," *Journal of adhesion science and technology*, vol. 21, no. 12-13, pp. 1259–1280, 2007.

[42] M. D. Bartlett, A. B. Croll, D. R. King, B. M. Paret, D. J. Irschick, and A. J. Crosby, "Looking beyond fibrillar features to scale gecko-like adhesion," *Advanced Materials*, 2012.

[43] R. G. Balijepalli, S. C. Fischer, R. Hensel, R. M. McMeeking, and E. Arzt, "Numerical study of adhesion enhancement by composite fibrils with soft tip layers," *Journal of the Mechanics and Physics of Solids*, vol. 99, pp. 357–378, 2017.

[44] S. C. L. Fischer, E. Arzt, and R. Hensel, "Composite pillars with a tunable interface for adhesion to rough substrates," *ACS Applied Materials and Interfaces*, vol. 9, pp. 1036–1044, 1 2017.

[45] S. Gorumlu and B. Aksak, "Sticking to rough surfaces using functionally graded bio-inspired microfibres," *Royal Society open science*, vol. 4, no. 6, p. 161105, 2017.

[46] C. Greiner, R. Spolenak, and E. Arzt, "Adhesion design maps for fibrillar adhesives: The effect of shape," *Acta Biomaterialia*, vol. 5, pp. 597–606, 2 2009.

[47] X. Zhang, Y. Wang, R. Hensel, and E. Arzt, "A design strategy for mushroom-shaped microfibrils with optimized dry adhesion: Experiments and finite element analyses," *Journal of Applied Mechanics*, vol. 88, 3 2021.

[48] J. A. Booth and R. Hensel, "Perspective on statistical effects in the adhesion of micropatterned surfaces," *Applied Physics Letters*, vol. 119, p. 230502, 12 2021.

[49] S. Alvo, *Etude, modélisation et mesure des forces d'adhésion à l'échelle microscopique*. PhD thesis, Paris 6, 2012.

[50] X. Jin, L. Heepe, J. Strueben, R. Adelung, S. N. Gorb, and A. Staubitz, "Challenges and solutions for joining polymer materials," *Macromolecular Rapid Communications*, vol. 35, pp. 1551–1570, 9 2014.

[51] R. M. McMeeking, E. Arzt, and A. G. Evans, "Defect dependent adhesion of fibrillar surfaces," *The Journal of Adhesion*, vol. 84, pp. 675–681, 8 2008.

[52] H. Yao and H. Gao, "Gibson-soil-like materials achieve flaw-tolerant adhesion," *Journal of Computational and Theoretical Nanoscience*, vol. 7, pp. 1299–1305, 7 2010.

[53] M. Bacca, J. A. Booth, K. L. Turner, and R. M. McMeeking, "Load sharing in bioinspired fibrillar adhesives with backing layer interactions and interfacial misalignment," *Journal of the Mechanics and Physics of Solids*, 2016.

[54] J. A. Booth, M. Bacca, R. M. McMeeking, and K. L. Foster, "Benefit of backing-layer compliance in fibrillar adhesive patches—resistance to peel propagation in the presence of interfacial misalignment," *Advanced Materials Interfaces*, vol. 5, 8 2018.

[55] H. Khungura and M. Bacca, "Optimal load sharing in bioinspired fibrillar adhesives: Asymptotic solution," *Journal of Applied Mechanics*, vol. 88, 3 2021.

[56] V. Barreau, R. Hensel, N. K. Guimard, A. Ghatak, R. M. McMeeking, and E. Arzt, "Fibrillar elastomeric micropatterns create tunable adhesion even to rough surfaces," *Advanced Functional Materials*, vol. 26, pp. 4687–4694, 2016.

[57] N. Cadirov, J. A. Booth, K. L. Turner, and J. N. Israelachvili, "Influence of humidity on grip and release adhesion mechanisms for gecko-inspired microfibrillar surfaces," *ACS applied materials & interfaces*, vol. 9, no. 16, pp. 14497–14505, 2017.

[58] D. Sameoto and C. Menon, "Recent advances in the fabrication and adhesion testing of biomimetic dry adhesives," *Smart Materials and Structures*, vol. 19, p. 103001, 10 2010.

[59] S. A. Suresh, A. Hajj-Ahmad, E. W. Hawkes, and M. R. Cutkosky, "Forcing the issue: Testing gecko-inspired adhesives: Forcing the issue: Testing gecko-inspired adhesives," *Journal of the Royal Society Interface*, vol. 18, 1 2021.

[60] P. K. Porwal and C. Y. Hui, "Strength statistics of adhesive contact between a fibrillar structure and a rough substrate," *Journal of the Royal Society Interface*, vol. 5, pp. 441–448, 4 2008.

[61] W. Weibull, "A statistical theory of the strength of materials. generalstabens litografiska anstalts förlag, stockholm," *Gen. Litogr. Anst. Förlag*, vol. 151, pp. 189–206, 1939.

[62] V. Tinnemann, L. Hernández, S. C. L. Fischer, E. Arzt, R. Bennewitz, and R. Hensel, "In situ observation reveals local detachment mechanisms and suction effects in micropatterned adhesives," *Advanced Functional Materials*, vol. 29, p. 1807713, 4 2019.

[63] J. A. Booth, V. Tinnemann, R. Hensel, E. Arzt, R. M. McMeeking, and K. L. Foster, "Statistical properties of defect-dependent detachment strength in bioinspired dry adhesives," *Journal of the Royal Society Interface*, vol. 16, 2019.

[64] R. Hensel, J. Thiemecke, and J. A. Booth, "Preventing catastrophic failure of microfibrillar adhesives in compliant systems based on statistical analysis of adhesive strength," *ACS Applied Materials and Interfaces*, vol. 13, pp. 19422–19429, 4 2021.

[65] S. Kim, M. Spenko, S. Trujillo, B. Heyneman, D. Santos, and M. R. Cutkoskly, "Smooth vertical surface climbing with directional adhesion," *IEEE Transactions on Robotics*, vol. 24, pp. 65–74, 2 2008.

[66] S. Song, D. M. Drotlef, C. Majidi, and M. Sitti, "Controllable load sharing for soft adhesive interfaces on three-dimensional surfaces," *Proceedings of the National Academy of Sciences of the United States of America*, vol. 114, pp. E4344–E4353, 5 2017.

[67] G. Moreira Lana, K. Sorg, G. I. Wenzel, D. Hecker, R. Hensel, B. Schick, K. Kruttwig, and E. Arzt, "Self-adhesive silicone microstructures for the treatment of tympanic membrane perforations," *Advanced NanoBiomed Research*, vol. 1, p. 2100057, 10 2021.

[68] H. Jiang, E. W. Hawkes, V. Arutyunov, J. Tims, C. Fuller, J. P. King, C. Seubert, H. L. Chang, A. Parness, and M. R. Cutkosky, "Scaling controllable adhesives to grapple floating objects in space," *2015 IEEE International Conference on Robotics and Automation (ICRA)*, pp. 2828–2835, 5 2015.

[69] C. Menon, M. Murphy, and M. Sitti, "Gecko inspired surface climbing robots," in *2004 IEEE International Conference on Robotics and Biomimetics*, pp. 431–436, IEEE, 2004.

[70] C. Menon and M. Sitti, "A biomimetic climbing robot based on the gecko," *Journal of Bionic Engineering*, vol. 3, pp. 115–125, 9 2006.

[71] P. Glick, S. A. Suresh, D. Ruffatto, M. Cutkosky, M. T. Tolley, and A. Parness, "A soft robotic gripper with gecko-inspired adhesive," *IEEE Robotics and Automation Letters*, vol. 3, pp. 903–910, 4 2018.

[72] A. Parness, T. Hilgendorf, P. Daniel, M. Frost, V. White, and B. Kennedy, "Controllable on-off adhesion for earth orbit grappling applications," *2013 IEEE Aerospace Conference*, pp. 1–11, 3 2013.

[73] K. A. Daltorio, S. Gorb, A. Peressadko, A. D. Horchler, R. E. Ritzmann, and R. D. Quinn, "A robot that climbs walls using micro-structured polymer feet," *Climbing and Walking Robots*, pp. 131–138, 2006.

[74] H. Jiang, E. W. Hawkes, C. Fuller, M. A. Estrada, S. A. Suresh, N. Abcouwer, A. K. Han, S. Wang, C. J. Ploch, A. Parness, and M. R. Cutkosky, "A robotic device using gecko-inspired adhesives can grasp and manipulate large objects in microgravity," *Sci. Robot*, vol. 2, p. 28, 2017.

[75] D. Sameoto, H. Khungura, F. H. Benvidi, A. Asad, T. Liang, and M. Bacca, "Space applications for gecko-inspired adhesives," *Biomimicry for Aerospace*, pp. 423–458, 2022.

[76] M. K. Kwak, H. E. Jeong, and K. Y. Suh, "Rational design and enhanced biocompatibility of a dry adhesive medical skin patch," *Advanced Materials*, vol. 23, pp. 3949–3953, 9 2011.

[77] S. Baik, H. J. Lee, D. W. Kim, J. W. Kim, Y. Lee, and C. Pang, "Bioinspired adhesive architectures: From skin patch to integrated bioelectronics," *Advanced Materials*, vol. 31, 8 2019.

[78] J. Purtov, M. Frensemeier, and E. Kroner, "Switchable adhesion in vacuum using bio-inspired dry adhesives," *ACS Applied Materials and Interfaces*, vol. 7, pp. 24127–24135, 2015.

[79] H. K. Minsky and K. T. Turner, "Composite microposts with high dry adhesion strength," *ACS Applied Materials and Interfaces*, vol. 9, pp. 18322–18327, 5 2017.

[80] J. Jeong, J. Kim, K. Song, K. Autumn, and J. Lee, "Geckoprinting: assembly of microelectronic devices on unconventional surfaces by transfer printing with isolated gecko setal arrays," *Journal of The Royal Society Interface*, vol. 11, p. 20140627, 10 2014.

[81] D. Paretkar, M. Kamperman, D. Martina, J. Zhao, C. Creton, A. Lindner, A. Jagota, R. McMeeking, and E. Arzt, "Preload-responsive adhesion: effects of aspect ratio, tip shape and alignment," *Journal of The Royal Society Interface*, vol. 10, p. 20130171, 6 2013.

[82] S. Stark, M. R. Begley, and R. M. McMeeking, "The buckling and postbuckling of fibrils adhering to a rigid surface," *Journal of Applied Mechanics, Transactions ASME*, vol. 80, 2013.

[83] M. Varenberg and S. Gorb, "Close-up of mushroom-shaped fibrillar adhesive microstructure: Contact element behaviour," *Journal of the Royal Society Interface*, vol. 5, pp. 785–789, 7 2008.

[84] M. Frensemeier, J. S. Kaiser, C. P. Frick, A. S. Schneider, E. Arzt, R. S. Fertig, and E. Kroner, "Temperature-induced switchable adhesion using nickel-titanium-polydimethylsiloxane hybrid surfaces," *Advanced Functional Materials*, vol. 25, pp. 3013–3021, 5 2015.

[85] E. Kizilkan, J. Strueben, A. Staubitz, and S. N. Gorb, "Bioinspired photocontrollable microstructured transport device," *Science Robotics*, vol. 2, 1 2017.

[86] J. D. Eisenhaure, T. Xie, S. Varghese, and S. Kim, "Microstructured shape memory polymer surfaces with reversible dry adhesion," *ACS Applied Materials and Interfaces*, vol. 5, pp. 7714–7717, 8 2013.

[87] D. M. Drotlef, P. Blümler, and A. D. Campo, "Magnetically actuated patterns for bioinspired reversible adhesion (dry and wet)," *Advanced Materials*, vol. 26, pp. 775–779, 2 2014.

[88] K. Fuller and D. Tabor, "The effect of surface roughness on the adhesion of elastic solids," *Proceedings of the Royal Society of London. A. Mathematical and Physical Sciences*, vol. 345, pp. 327–342, 9 1975.

[89] B. N. Persson, "Theory of rubber friction and contact mechanics," *J. Chem. Phys.*, vol. 115, no. 8, pp. 3840–3861, 2001.

[90] B. N. Persson, "Adhesion between an elastic body and a randomly rough hard surface," *European Physical Journal E*, vol. 8, pp. 385–401, 2002.

[91] B. N. Persson and S. Gorb, "The effect of surface roughness on the adhesion of elastic plates with application to biological systems," *Journal of Chemical Physics*, vol. 119, pp. 11437–11444, 12 2003.

[92] B. N. Persson, "Contact mechanics for randomly rough surfaces," *Surface Science Reports*, vol. 61, pp. 201–227, 6 2006.

[93] M. H. Müser, W. B. Dapp, R. Bugnicourt, P. Sainsot, N. Lesaffre, T. A. Lubrecht, B. N. J. Persson, K. Harris, A. Bennett, K. Schulze, S. Rohde, P. Ifju, W. G. Sawyer, T. Angelini, H. A. Esfahani, M. Kadkhodaei, S. Akbarzadeh, J.-J. Wu, G. Vorlaufer, A. Vernes, S. Solhjoo, A. I. Vakis, R. L. Jackson, Y. Xu, J. Streator, A. Rostami, D. Dini, S. Medina, G. Carbone, F. Bottiglione, L. Afferrante, J. Monti, L. Pastewka, M. O. Robbins, and J. A. Greenwood, "Meeting the contact-mechanics challenge," *Tribology Letters*, vol. 65, aug 2017.

[94] C. Campañá and M. H. Müser, "Practical Green's function approach to the simulation of elastic semi-infinite solids," *Phys. Rev. B - Condens. Matter Mater. Phys.*, vol. 74, no. 7, pp. 1–15, 2006.

[95] G. Carbone and L. Mangialardi, "Analysis of the adhesive contact of confined layers by using a Green's function approach," *J. Mech. Phys. Solids*, vol. 56, no. 2, pp. 684–706, 2008.

[96] G. Carbone, B. Lorenz, B. N. Persson, and A. Wohlers, "Contact mechanics and rubber friction for randomly rough surfaces with anisotropic statistical properties," *Eur. Phys. J. E*, vol. 29, no. 3, pp. 275–284, 2009.

[97] C. Putignano, W. Dapp, and M. Müser, "A green's function molecular dynamics approach to the mechanical contact between thin elastic sheets and randomly rough surfaces," *Biomimetics*, vol. 1, p. 7, 10 2016.

[98] S. P. Venugopalan, L. Nicola, and M. H. Müser, "Green's function molecular dynamics: including finite heights, shear, and body fields," *Modelling and Simulation in Materials Science and Engineering*, vol. 25, p. 034001, 4 2017.

[99] Y. Zhou, M. Moseler, and M. H. Müser, "Solution of boundary-element problems using the fast-inertial-relaxation-engine method," *Phys. Rev. B*, vol. 99, no. 14, pp. 1–8, 2019.

[100] S. Sukhomlinov and M. H. Müser, "On the viscous dissipation caused by randomly rough indenters in smooth sliding motion," *Appl. Surf. Sci. Adv.*, vol. 6, p. 100182, 2021.

[101] S. N. Gorb and M. Varenberg, "Mushroom-shaped geometry of contact elements in biological adhesive systems," *Journal of Adhesion Science and Technology*, vol. 21, pp. 1175–1183, 10 2007.

[102] S. Maegawa, F. Itoigawa, and T. Nakamura, "Effect of normal load on friction coefficient for sliding contact between rough rubber surface and rigid smooth plane," *Tribology International*, vol. 92, pp. 335–343, 8 2015.

[103] F. Zernike, "Phase contrast, a new method for the microscopic observation of transparent objects," *Physica*, vol. 9, pp. 686–698, 7 1942.

[104] J. Dyson and W. Hirst, "The true contact area between solids," *Proceedings of the Physical Society. Section B*, vol. 67, pp. 309–312, 4 1954.

[105] N. J. Harrick, "Use of frustrated total internal reflection to measure film thickness and surface reliefs," *Journal of Applied Physics*, vol. 33, pp. 2774–2775, 1962.

[106] C. W. McCutchen, "Optical systems for observing surface topography by frustrated total internal reflection and by interference," *Review of Scientific Instruments*, vol. 35, pp. 1340–1345, 1964.

[107] E. V. Eason, E. W. Hawkes, M. Windheim, D. L. Christensen, T. Libby, and M. R. Cutkosky, "Stress distribution and contact area measurements of a gecko toe using a high-resolution tactile sensor," *Bioinspiration and Biomimetics*, vol. 10, 2 2015.

[108] B. A. Krick, J. R. Vail, B. N. Persson, and W. G. Sawyer, "Optical in situ micro tribometer for analysis of real contact area for contact mechanics, adhesion, and sliding experiments," *Tribology Letters*, vol. 45, pp. 185–194, 1 2012.

[109] W. Federle, "An integrative study of insect adhesion: Mechanics and wet adhesion of pretarsal pads in ants," *Integrative and Comparative Biology*, vol. 42, pp. 1100–1106, 12 2002.

[110] W. Federle and T. Endlein, "Locomotion and adhesion: dynamic control of adhesive surface contact in ants," *Arthropod Structure and Development*, vol. 33, pp. 67–75, 1 2004.

[111] W. Federle, W. Barnes, W. Baumgartner, P. Drechsler, and J. Smith, "Wet but not slippery: boundary friction in tree frog adhesive toe pads," *Journal of The Royal Society Interface*, vol. 3, pp. 689–697, 10 2006.

[112] P. L. Laturnus, "Use of a simple coaxial lighting system to enhance fingerprint and handwriting evidence," *J. Can. Soc. Forensic Sci.*, vol. 27, no. 2, pp. 69–80, 1994.

[113] U. Thombansen and M. Ungers, "Illumination for process observation in laser material processing," *Phys. Procedia*, vol. 56, no. C, pp. 1286–1296, 2014.

[114] A. Sakaguchi, Y. I. Matsumoto, K. Toriumi, and H. Kim, "Novel Observation Technique for Contact Condition of Fabric," *Text. Res. J.*, vol. 72, no. 3, pp. 221–226, 2002.

[115] "Coaxial illumination." `https://www.keyence.com/ss/products/microscope/microscope_glossary/lighting/coaxial_illumination.jsp`. Accessed: 2022-07-20.

[116] F. Rosenblatt, "The perceptron: A probabilistic model for information storage and organization in the brain.," *Psychological Review*, vol. 65, pp. 386–408, 1958.

[117] C. Robert, "Machine learning, a probabilistic perspective," *CHANCE*, vol. 27, 2014.

[118] J. Boyan, D. Freitag, and T. Joachims, "A machine learning architecture for optimizing web search engines," in *AAAI Workshop on Internet Based Information Systems*, pp. 1–8, 1996.

[119] E. G. Dada, J. S. Bassi, H. Chiroma, A. O. Adetunmbi, O. E. Ajibuwa, *et al.*, "Machine learning for email spam filtering: review, approaches and open research problems," *Heliyon*, vol. 5, no. 6, p. e01802, 2019.

[120] J.-A. Choi and K. Lim, "Identifying machine learning techniques for classification of target advertising," *ICT Express*, vol. 6, no. 3, pp. 175–180, 2020.

[121] A. Waibel, T. Hanazawa, G. Hinton, K. Shikano, and K. Lang, "Phoneme recognition using time-delay neural networks," *IEEE Transactions on Acoustics, Speech, and Signal Processing*, vol. 37, pp. 328–339, 3 1989.

[122] D. A. Pomerleau, "Alvinn: An autonomous land vehicle in a neural network," *Advances in neural information processing systems*, vol. 1, 1988.

[123] K. T. Butler, D. W. Davies, H. Cartwright, O. Isayev, and A. Walsh, "Machine learning for molecular and materials science," *Nature*, vol. 559, pp. 547–555, 7 2018.

[124] K. Guo, Z. Yang, C.-H. Yu, and M. J. Buehler, "Artificial intelligence and machine learning in design of mechanical materials," *Materials Horizons*, 2021.

[125] Y. Kim, C. Yang, Y. Kim, G. X. Gu, and S. Ryu, "Designing an adhesive pillar shape with deep learning-based optimization," *ACS Applied Materials and Interfaces*, vol. 12, pp. 24458–24465, 5 2020.

[126] J. Schmidt, M. R. Marques, S. Botti, and M. A. Marques, "Recent advances and applications of machine learning in solid-state materials science," *npj Computational Materials*, vol. 5, 12 2019.

[127] H. B. Barlow, "Unsupervised learning," *Neural computation*, vol. 1, no. 3, pp. 295–311, 1989.

[128] I. T. Jolliffe and J. Cadima, "Principal component analysis: a review and recent developments," *Philosophical Transactions of the Royal Society A: Mathematical, Physical and Engineering Sciences*, vol. 374, no. 2065, p. 20150202, 2016.

[129] L. Rokach and O. Maimon, "Clustering methods," in *Data mining and knowledge discovery handbook*, pp. 321–352, Springer, 2005.

[130] X. Zhu and A. B. Goldberg, "Introduction to semi-supervised learning," *Synthesis lectures on artificial intelligence and machine learning*, vol. 3, no. 1, pp. 1–130, 2009.

[131] R. S. Sutton and A. G. Barto, *Reinforcement learning: An introduction*. MIT press, 2018.

[132] D. Silver, A. Huang, C. J. Maddison, A. Guez, L. Sifre, G. Van Den Driessche, J. Schrittwieser, I. Antonoglou, V. Panneershelvam, M. Lanctot, *et al.*, "Mastering the game of go with deep neural networks and tree search," *nature*, vol. 529, no. 7587, pp. 484–489, 2016.

[133] R. M. Neal, "Pattern recognition and machine learning," *Technometrics*, vol. 49, 2007.

[134] "Cross-validation: evaluating estimator performance." `https://scikit-learn.org/stable/modules/cross_validation.html`. Accessed: 2022-04-15.

[135] B. K. Sarkar, "A case study on partitioning data for classification," *International Journal of Information and Decision Sciences*, vol. 8, no. 1, pp. 73–91, 2016.

[136] P. Refaeilzadeh, L. Tang, and H. Liu, "Cross-validation.," *Encyclopedia of database systems*, vol. 5, pp. 532–538, 2009.

[137] P. McCullagh and J. A. Nelder, *Generalized linear models*. Routledge, 2019.

[138] R. E. Wright, "Logistic regression.," 1995.

[139] D. G. Kleinbaum, K. Dietz, M. Gail, M. Klein, and M. Klein, *Logistic regression*. Springer, 2002.

[140] C. Cortes, V. Vapnik, and L. Saitta, "Support-vector networks editor," *Machine Leaming*, vol. 20, pp. 273–297, 1995.

[141] W. S. Noble, "What is a support vector machine?," *Nature biotechnology*, vol. 24, no. 12, pp. 1565–1567, 2006.

[142] A. J. Smola and B. Schölkopf, "A tutorial on support vector regression," *Statistics and computing*, vol. 14, no. 3, pp. 199–222, 2004.

[143] M. Awad and R. Khanna, "Support vector regression," in *Efficient learning machines*, pp. 67–80, Springer, 2015.

[144] J. R. Quinlan, "Induction of decision trees," *Machine Learning*, vol. 1, pp. 81–106, 3 1986.

[145] "Decision trees." `https://scikit-learn.org/stable/modules/tree.html`. Accessed: 2022-04-15.

[146] M. Somvanshi, P. Chavan, S. Tambade, and S. Shinde, "A review of machine learning techniques using decision tree and support vector machine," in *2016 international conference on computing communication control and automation (ICCUBEA)*, pp. 1–7, IEEE, 2016.

[147] L. Breiman, "Arcing the edge," tech. rep., Technical Report 486, Statistics Department, University of California at ..., 1997.

[148] J. H. Friedman, "Greedy function approximation: A gradient boosting machine.," *The Annals of Statistics*, vol. 29, pp. 1189–1232, 10 2001.

[149] J. H. Friedman, "Stochastic gradient boosting," *Computational statistics & data analysis*, vol. 38, no. 4, pp. 367–378, 2002.

[150] J. Goldberger, G. E. Hinton, S. Roweis, and R. R. Salakhutdinov, "Neighbourhood components analysis," *Advances in neural information processing systems*, vol. 17, 2004.

[151] "Nearest neighbors." `https://scikit-learn.org/stable/modules/neighbors.html#nearest-neighbors-classification`. Accessed: 2022-04-15.

[152] G. Fantoni, M. Santochi, G. Dini, K. Tracht, B. Scholz-Reiter, J. Fleischer, T. K. Lien, G. Seliger, G. Reinhart, J. Franke, H. N. Hansen, and A. Verl, "Grasping devices and methods in automated production processes," *CIRP Annals - Manufacturing Technology*, vol. 63, pp. 679–701, 2014.

[153] J. Frohm, V. Lindström, M. Winroth, and J. Stahre, "Levels of automation in manufacturing," *Ergonomia*, 2008.

[154] S. Gorb and R. Beutel, "Evolution of locomotory attachment pads of hexapods," *Naturwissenschaften*, vol. 88, pp. 530–534, 2001.

[155] D. Sameoto, H. Sharif, and C. Menon, "Investigation of low-pressure adhesion performance of mushroom shaped biomimetic dry adhesives," *Journal of Adhesion Science and Technology*, vol. 26, pp. 2641–2652, 2012.

[156] M. Kamperman, E. Kroner, A. del Campo, R. M. McMeeking, and E. Arzt, "Functional adhesive surfaces with "gecko" effect: The concept of contact splitting," *Advanced Engineering Materials*, vol. 12, pp. 335–348, 2010.

[157] J. Thiemecke and R. Hensel, "Contact Aging Enhances Adhesion of Micropatterned Silicone Adhesives to Glass Substrates," *Adv. Funct. Mater.*, vol. 30, no. 50, 2020.

[158] V. Lindström, M. Winroth, and J. Stahre, "Levels of automation in manufacturing," *Ergonomia*, vol. 30, 2008.

[159] R. L. Katz and P. Koutroumpis, "Measuring socio-economic digitization: A paradigm shift," *SSRN Electronic Journal*, 2012.

[160] A. Parness, D. Soto, N. Esparza, N. Gravish, M. Wilkinson, K. Autumn, and M. Cutkosky, "A microfabricated wedge-shaped adhesive array displaying gecko-like dynamic adhesion, directionality and long lifetime," *Journal of The Royal Society Interface*, vol. 6, pp. 1223–1232, 12 2009.

[161] J. Davies, S. Haq, T. Hawke, and J. Sargent, "A practical approach to the development of a synthetic gecko tape," *International Journal of Adhesion and Adhesives*, vol. 29, no. 4, pp. 380–390, 2009.

[162] M. P. Murphy, S. Kim, and M. Sitti, "Enhanced adhesion by gecko-inspired hierarchical fibrillar adhesives," *ACS Applied Materials and Interfaces*, vol. 1, pp. 849–855, 4 2009.

[163] D. R. King, M. D. Bartlett, C. A. Gilman, D. J. Irschick, and A. J. Crosby, "Creating gecko-like adhesives for "real world" surfaces," *Advanced Materials*, 2014.

[164] V. Tinnemann, E. Arzt, and R. Hensel, "Switchable double-sided micropatterned adhesives for selective fixation and detachment," *Journal of the Mechanics and Physics of Solids*, vol. 123, pp. 20–27, 2 2019.

[165] K. Autumn and N. Gravish, "Gecko adhesion: evolutionary nanotechnology," *Philosophical Transactions of the Royal Society A: Mathematical, Physical and Engineering Sciences*, vol. 366, pp. 1575–1590, 5 2008.

[166] C. Pang, K. Mak, Y. Zhang, Y. Yang, Y. A. Tse, and M. Y. Wang, "Viko: An adaptive gecko gripper with vision-based tactile sensor," in *2021 IEEE International Conference on Robotics and Automation (ICRA)*, pp. 736–742, IEEE, 2021.

[167] E. W. Hawkes, D. L. Christensen, A. K. Han, H. Jiang, and M. R. Cutkosky, "Grasping without squeezing: Shear adhesion gripper with fibrillar thin film," *Proceedings - IEEE International Conference on Robotics and Automation*, vol. 2015-June, pp. 2305–2312, 6 2015.

[168] E. W. Hawkes, H. Jiang, and M. R. Cutkosky, "Three-dimensional dynamic surface grasping with dry adhesion," *International Journal of Robotics Research*, vol. 35, pp. 943–958, 7 2016.

[169] M. Dadkhah, Z. Zhao, N. Wettels, and M. Spenko, "A self-aligning gripper using an electrostatic/gecko-like adhesive," in *2016 IEEE/RSJ International Conference on Intelligent Robots and Systems (IROS)*, pp. 1006–1011, IEEE, 2016.

[170] S. Song, C. Majidi, and M. Sitti, "Geckogripper: A soft, inflatable robotic gripper using gecko-inspired elastomer micro-fiber adhesives," in *2014 IEEE/RSJ International Conference on Intelligent Robots and Systems*, pp. 4624–4629, IEEE, 2014.

[171] M. Samri, J. Thiemecke, E. Prinz, T. Dahmen, R. Hensel, and E. Arzt, "Predicting the adhesion strength of micropatterned surfaces using supervised machine learning," *Materials Today*, 2022.

[172] S. Reddy, E. Arzt, and A. D. Campo, "Bioinspired surfaces with switchable adhesion," *Advanced Materials*, vol. 19, pp. 3833–3837, 11 2007.

[173] A. D. Roberts, "Looking at rubber adhesion," *Rubber Chemistry and Technology*, vol. 52, pp. 23–42, 3 1979.

[174] A. D. Roberts, "Squeeze films between rubber and glass," *Journal of Physics D: Applied Physics*, vol. 4, p. 311, 3 1971.

[175] M. Samri, A. Kossa, and R. Hensel, "Effect of Subsurface Microstructures on Adhesion of Highly Confined Elastic Films," *J. Appl. Mech. Trans. ASME*, vol. 88, no. 3, pp. 1–9, 2021.

[176] B. Guo, B. Zhang, S. Fang, L. Yang, and A. Zhang, "The study of the effective contact area of suction cup," tech. rep., SAE Technical Paper, 2021.

[177] Z. Wang, A. C. Bovik, H. R. Sheikh, and E. P. Simoncelli, "Image quality assessment: from error visibility to structural similarity," *IEEE transactions on image processing*, vol. 13, no. 4, pp. 600–612, 2004.

[178] Y. L. Chen, C. A. Helm, and J. N. Israelachvili, "Molecular mechanisms associated with adhesion and contact angle hysteresis of monolayer surfaces," *The Journal of Physical Chemistry*, vol. 95, pp. 10736–10747, dec 1991.

[179] Y. Liu and I. Szlufarska, "Chemical origins of frictional aging," *Physical Review Letters*, vol. 109, nov 2012.

[180] N. Maeda, N. Chen, M. Tirrell, and J. N. Israelachvili, "Adhesion and friction mechanisms of polymer-on-polymer surfaces," *Science*, vol. 297, pp. 379–382, jul 2002.

[181] M. Giri, D. B. Bousfield, and W. N. Unertl, "Dynamic contacts on viscoelastic films: work of adhesion," *Langmuir*, vol. 17, pp. 2973–2981, apr 2001.

[182] K. R. Shull, "Contact mechanics and the adhesion of soft solids," *Materials Science and Engineering: R: Reports*, vol. 36, pp. 1–45, jan 2002.

[183] B. Lorenz, B. A. Krick, N. Mulakaluri, M. Smolyakova, S. Dieluweit, W. G. Sawyer, and B. N. J. Persson, "Adhesion: role of bulk viscoelasticity and surface roughness," *Journal of Physics: Condensed Matter*, vol. 25, p. 225004, may 2013.

[184] A. Tiwari, L. Dorogin, A. I. Bennett, K. D. Schulze, W. G. Sawyer, M. Tahir, G. Heinrich, and B. N. Persson, "The effect of surface roughness and viscoelasticity on rubber adhesion," *Soft Matter*, vol. 13, no. 19, pp. 3602–3621, 2017.

[185] J. P. Pickering, D. W. V. D. Meer, and G. J. Vancso, "Effects of contact time, humidity, and surface roughness on the adhesion hysteresis of polydimethylsiloxane," *Journal of Adhesion Science and Technology*, vol. 15, pp. 1429–1441, jan 2001.

[186] A. A. Feiler, J. Stiernstedt, K. Theander, P. Jenkins, and M. W. Rutland, "Effect of capillary condensation on friction force and adhesion," *Langmuir*, vol. 23, pp. 517–522, dec 2006.

[187] J. Israelachvili, *Intermolecular and Surface Forces*. Elsevier Inc, 3rd editio ed., 2011.

[188] L. Prandtl, "Ein Gedankenmodell zur kinetischen Theorie der festen Körper," *Zeitschrift für Angew. Math. und Mech.*, vol. 8, no. 2, pp. 85–106, 1928.

[189] W. Zheng and Z. Ya-Pu, "Adhesion elastic contact and hysteresis effect," *Chinese Physics*, vol. 13, pp. 1320–1325, jul 2004.

[190] P. Guduru, "Detachment of a rigid solid from an elastic wavy surface: Theory," *Journal of the Mechanics and Physics of Solids*, vol. 55, pp. 445–472, mar 2007.

[191] H. Kesari, J. C. Doll, B. L. Pruitt, W. Cai, and A. J. Lew, "Role of surface roughness in hysteresis during adhesive elastic contact," *Philosophical Magazine Letters*, vol. 90, pp. 891–902, dec 2010.

[192] G. Carbone, E. Pierro, and G. Recchia, "Loading-unloading hysteresis loop of randomly rough adhesive contacts," *Physical Reviews E*, vol. 92, dec 2015.

[193] S. Dalvi, A. Gujrati, S. R. Khanal, L. Pastewka, A. Dhinojwala, and T. D. B. Jacobs, "Linking energy loss in soft adhesion to surface roughness," *Proceedings of the National Academy of Sciences*, vol. 116, pp. 25484–25490, nov 2019.

[194] A. Sanner, W. G. Nöhring, L. A. Thimons, T. D. Jacobs, and L. Pastewka, "Scale-dependent roughness parameters for topography analysis," *Appl. Surf. Sci. Adv.*, vol. 7, no. September 2021, 2022.

[195] M. H. Müser, W. B. Dapp, R. Bugnicourt, P. Sainsot, N. Lesaffre, T. A. Lubrecht, B. N. Persson, K. Harris, A. Bennett, K. Schulze, S. Rohde, P. Ifju, W. G. Sawyer, T. Angelini, H. Ashtari Esfahani, M. Kadkhodaei, S. Akbarzadeh, J. J. Wu, G. Vorlaufer, A. Vernes, S. Solhjoo, A. I. Vakis, R. L. Jackson, Y. Xu, J. Streator, A. Rostami, D. Dini, S. Medina, G. Carbone, F. Bottiglione, L. Afferrante, J. Monti, L. Pastewka, M. O. Robbins, and J. A. Greenwood, "Meeting the Contact-Mechanics Challenge," *Tribol. Lett.*, vol. 65, no. 4, 2017.

[196] A. I. Bennett, K. L. Harris, K. Schulze, J. M. Urueña, A. J. McGhee, A. A. Pitenis, M. H. Müser, T. E. Angelini, W. G. Sawyer, *et al.*, "Contact measurements of randomly rough surfaces," *Tribology Letters*, vol. 65, no. 4, pp. 1–8, 2017.

[197] B. Weber, T. Suhina, T. Junge, L. Pastewka, A. M. Brouwer, and D. Bonn, "Molecular probes reveal deviations from amontons' law in multi-asperity frictional contacts," *Nat. Commun.*, vol. 9, p. 888, Mar. 2018.

[198] M. H. Müser and B. N. Persson, "Crack and pull-off dynamics of adhesive, viscoelastic solids," *Europhys. Lett.*, 2022.

[199] M. Ciavarella, J. Greenwood, and J. Barber, "Effect of Tabor parameter on hysteresis losses during adhesive contact," *Journal of the Mechanics and Physics of Solids*, vol. 98, pp. 236–244, Jan. 2017.

[200] R. A. Schapery, "A theory of crack initiation and growth in viscoelastic media ii. approximate methods of analysis," *International Journal of Fracture*, vol. 11, pp. 369–388, June 1975.

[201] B. N. Persson and E. A. Brener, "Crack propagation in viscoelastic solids," *Phys. Rev. E*, vol. 71, no. 3, pp. 1–8, 2005.

[202] W. B. Dapp and M. H. Müser, "Contact mechanics of and Reynolds flow through saddle points: On the coalescence of contact patches and the leakage rate through near-critical constrictions," *Europhys. Lett.*, vol. 109, no. 4, p. 44001, 2015.

[203] A. Wang and M. H. Müser, "On the adhesion between thin sheets and randomly rough surfaces," *Friction*, 2022.

[204] R. Caracciolo and M. Giovagnoni, "Frequency dependence of Poisson's ratio using the method of reduced variables," *Mech. Mater.*, vol. 24, no. 1, pp. 75–85, 1996.

[205] N. W. Tschoegl, W. G. Knauss, and I. Emri, "Poisson's ratio in linear viscoelasticity - a critical review," *Mech. Time-Dependent Mater.*, vol. 6, no. 1, pp. 3–51, 2002.

[206] J. S. van Dokkum and L. Nicola, "Green's function molecular dynamics including viscoelasticity," *Modelling and Simulation in Materials Science and Engineering*, vol. 27, p. 075006, aug 2019.

[207] R. Bugnicourt, P. Sainsot, N. Lesaffre, and A. Lubrecht, "Transient frictionless contact of a rough rigid surface on a viscoelastic half-space," *Tribology International*, vol. 113, pp. 279–285, Sept. 2017.

[208] M. H. Müser, H. Li, and R. Bennewitz, "Modeling the contact mechanics of hydrogels," *Lubricants*, vol. 7, no. 4, pp. 1–21, 2019.

[209] L. A. Thimons, A. Gujrati, A. Sanner, L. Pastewka, and T. D. B. Jacobs, "Hard-material adhesion: Which scales of roughness matter?," *Exp. Mech.*, vol. 61, pp. 1109–1120, Sept. 2021.

[210] D. Tabor, "Surface forces and surface interactions," *J. Colloid Interface Sci.*, vol. 58, no. 1, pp. 2–13, 1977.

[211] B. N. Persson, "Nanoadhesion," *Wear*, vol. 254, no. 9, pp. 832–834, 2003.

[212] M. H. Müser, "Single-asperity contact mechanics with positive and negative work of adhesion: Influence of finite-range interactions and a continuum description for the squeeze-out of wetting fluids," *Beilstein J. Nanotechnol.*, vol. 5, no. 1, pp. 419–437, 2014.

[213] R. Hensel, R. M. McMeeking, and A. Kossa, "Adhesion of a rigid punch to a confined elastic layer revisited," *J. Adhes.*, vol. 95, no. 1, pp. 44–63, 2019.

[214] C. Müller and M. H. Müser, "Analytical and numerical results for the elasticity and adhesion of elastic films with arbitrary Poisson's ratio and confinement," *J. Adhes.*, 2022.

[215] A. J. McGhee, A. A. Pitenis, A. I. Bennett, K. L. Harris, K. D. Schulze, J. M. Urueña, P. G. Ifju, T. E. Angelini, M. H. Müser, and W. G. Sawyer, "Contact and deformation of randomly rough surfaces with varying root-mean-square gradient," *Tribology Letters*, vol. 65, nov 2017.

[216] K. J. Wahl and W. G. Sawyer, "Observing interfacial sliding processes in solid–solid contacts," *MRS bulletin*, vol. 33, no. 12, pp. 1159–1167, 2008.

[217] W. G. Sawyer and K. J. Wahl, "Accessing inaccessible interfaces: in situ approaches to materials tribology," *MRS bulletin*, vol. 33, no. 12, pp. 1145–1150, 2008.

[218] Y. Jiang, D. S. Grierson, and K. T. Turner, "Flat punch adhesion: Transition from fracture-based to strength-limited pull-off," *J. Phys. D. Appl. Phys.*, vol. 47, no. 32, 2014.